POLITECNICO DI TORINO

Department of Electronics and Telecommunications
Master's Degree in Biomedical Engineering

Master's Degree Thesis

Near-field Microwave Antenna for Brain Screening

Supervisors
prof. Francesca Vipiana
prof. David Rodriguez Duarte
Martina Gugliermino
Alex Ramiro Masaquiza Caiza

Candidate
Enrico Conti

Dicembre 2025

A Mariuccia, Cristina ed Elisa, tre generazioni di donne fiere e incredibili.

A Cesare, Davide, Emilio e Francesco, quattro uomini dall'animo forte e buono.

Al mio amore Ludovica, luce della mia vita.

A tutti i miei straordinari amici.

Summary

This thesis presents the selection and optimization of a compact on-body wideband microwave antenna for brain screening, adaptable to sensing and imaging tasks exploited for diagnosis and monitoring. Specifically, the proposal antenna is projected to be integrated with the stroke monitoring system developed by the Wavison Research Group at Politecnico di Torino, extending its physical and electromagnetic performance requirements. Building on the requirement definitions, the first part of the work conducts a scoping review of state-of-the-art microwave bio-imaging antennas, resulting in the selection of five candidates — circular patch antenna with parasitic element, double substrate bowtie antenna, double ridge filled horn waveguide antenna, edge feed planar log periodic antenna and central feed planar log periodic antenna—which are studied in depth via full-wave simulations. Their performance was evaluated on both simplified and anatomically realistic head phantoms, focusing on reflection and transmission coefficients, near-field radiation patterns, and wave penetration. Among the selected designs, the filled-horn double-ridged waveguide antenna demonstrates superior performance, minimizing surface waves, reducing back radiation, and achieving deeper penetration —critical parameters. The second part covers the optimization of the latter by adjusting its geometry and including dielectric filling. The final optimized antenna operates in the -10 dB band from 0.84 to 1.34 GHz while maintaining a compact footprint of 31 $\times$ 23 mm2, suitable for a helmet-antenna-array with up to twenty-four elements. The filling material has a relative permittivity of 30. The optimized horn antenna represents a significant advancement, overcoming critical problem-specific system design requirements.

Acknowledgements

Ringrazio la professoressa Vipiana per avermi dato la possibilità di svolgere una tesi stimolante che mi ha permesso di imparare molto. Ringrazio il professor Rodriguez-Duarte, Martina Gugliermino e Alex Ramiro Masaquiza Caiza per il loro supporto durante il percorso. Ringrazio in particolar modo i miei genitori e i miei nonni che mi hanno fornito tutti gli strumenti e il supporto morale necessari per proseguire per l'intera durata del mio percorso, senza i quali non avrei mai potuto arrivare fino in fondo. Ringrazio Ludovica che mi ha dato tutto l'amore e la forza inestimabili per superare i momenti più bui e gli ostacoli più alti, soprattutto quelli interiori che solo lei avrebbe potuto aiutarmi a vedere. Grazie per aver sempre creduto in me. Ringrazio tutti i miei preziosissimi amici, che in questo viaggio mi hanno donato serenità e risate, e mi hanno sempre ricordato cosa voglio davvero nella mia vita. Se sono qui lo devo anche a voi.

Contents

Chapter 1

Introduction

1.1 Brain Stroke

Stroke is a great challenge all around the world. Its health threatening nature calls for continuous focus on prevention, treatment, and long-term care [1]. A true understanding of the disease requires examination of its global epidemiological impact, its underlying pathophysiology, the diverse clinical manifestations, and the therapeutic strategies employed.

Epidemiology and Burden

Stroke cases show regional variations in incidence, prevalence, and mortality [1, 2]. Incidence and mortality rates are positively correlated with the proportion of the population aged 65 years [1]. In Europe historical data highlight a strong gap between the two sides of the continent. Incidence rates are generally higher in Eastern European (EE) countries (3.0-5.0 per 1000 inhabitants) [2] compared to Western European (WE) countries (2.0-2.5 per 1000 inhabitants). Stroke is a leading cause of death globally: it is reported to be the third most frequent cause in most WE countries, and often higher in certain EE regions [2]. The percentage of fatality rates display substantial variation globally, with 28-to-30-day rates reported as high as 37-42% in some regions like India, and as low as 10% in others like Dijon, France [1].

Risk Factors and Demographics

A significant portion of the observed epidemiological disparities, particularly the higher incidence and case-fatality in EE, is attributed to a case mix involving more severe strokes and a higher prevalence of common risk factors such as hypertension and smoking [2]. Chronic conditions like arterial hypertension, diabetes, and hyperlipemia are known risk factors for stroke [3]. Data show higher incidence in males, but exceptions do exist, such as in Martinique [1].

Stroke Types and Pathophysiology

Stroke is broadly categorized into ischemic stroke (Acute Ischemic Stroke, AIS) and haemorrhagic stroke (Intracerebral Haemorrhage, ICH). In most Western European countries haemorrhagic strokes are estimated at 15% or less of all strokes. Rates can be considerably higher in certain Eastern European countries, reaching 30-35% [2].

A pivotal concept in AIS pathophysiology is the ischemic penumbra. This words designate tissue that is critically ischemic and functionally impaired, yet maintains preserved structural integrity. This region is at immediate risk of infarction. Penumbral tissue is identified by severely reduced cerebral blood flow (CBF) and a high oxygen extraction fraction (OEF): such characteristics indicate a mismatch between oxygen demand and supply. The fate of the penumbra (survival or infarction) is unpredictable and depends heavily on the degree and duration of ischemia [3].

Clinical Features and Outcomes

Spontaneous neurological recovery after a stroke is variable and can be substantial. One of the primary mechanisms that influence early recovery is the survival of the penumbral tissue. The volume of non-infarcted penumbra is highly correlated with neurological recovery measured at two months from the stroke. The degree of the initial neurological deficit shows a strong correlation with the volume of acutely neurally damaged tissue, defines as both the infarcted tissue and the non-infarcted tissue of the ischemic penumbra [3].

Apart from the sheer survival of the tissue, brain plasticity plays a significant role in functional recovery. Positron Emission Tomography (PET) studies on motor recovery after hemiplegic stroke tell us that movement of the recovered hand leads to a bilateral activation of the sensorimotor cortex and of the cerebellar hemispheres: this suggests that ipsilateral motor pathways contribute substantially to the recovery process [4].

Treatments and Complications

Effective stroke care requires a rapid and organized approach [2]. Acute management involves reperfusion therapies for AIS. Intravenous (IV) thrombolysis using alteplase is recommended for patients within 4.5 hours of symptom onset. Patients with acute large vessel occlusion (LVO) are usually treated with mechanical thrombectomy (MT): this procedure should be performed within 6 hours to 24 hours in case imaging demonstrates a favourable difference between the ischemic core area and the area with good perfusion status.

Imaging-based stroke diagnosis

In stroke care, neuroimaging is essential for diagnosis, categorisation and follow-up. Each of the various potential imaging techniques has its own advantages and disadvantages. Due to its availability and speed, computed tomography (CT) is the preferred method in

emergency situations. Non-contrast CT is also useful for confirming the presence or absence of bleeding. However, it has low sensitivity to ischaemia, with detection rates as low as 7% in the first three hours following onset[5].. For this reason, CT is less accurate at detecting ischaemic stroke in its early stages. Another common piece of hospital equipment is the magnetic resonance imaging (MRI) scanner, which provides excellent sensitivity and specificity. The gold standard for identifying acute infarcts is diffusion-weighted imaging. However, due to lengthy acquisition times, increased costs and restricted accessibility in many hospitals, this machine is not very practical in emergency situations. Perfusion-weighted imaging provides important new information about the penumbra, but requires resources that aren't always available in acute care settings. Finally, positron emission tomography (PET) is considered the most precise method for identifying the penumbra and infarct core. However, its lack of anatomical detail, high cost and lengthy acquisition times limit its clinical use. These limitations highlight the challenge of balancing practicality with diagnostic accuracy in day-to-day practice. Multimodal imaging is still essential in order to distinguish between different types of stroke, plan interventions, and track treatment results.[5].

Management of Intracerebral Haemorrhage (ICH) focuses on critical control measures. In case of patients with spontaneous ICH and hypertension, acute systolic blood pressure (SBP) should be lowered within 6 hours. The target is 140 mm Hg to mitigate hematoma expansion risk. However, it is imperative to avoid SBP < 110 mm. Moreover, rapid discontinuation and reversal of anticoagulation are required for associated ICH.

Guidelines indicate that stroke patients receive care in a specialized, geographically defined stroke unit, staffed by an interdisciplinary rehabilitation team [6]. The traditional concept of a rigid therapeutic time window for anti-ischemic agents should be replaced by individual assessment of the brain's physiological status. A particular important indicator is therefore the extent of the still-present penumbra [3].

1.2 Microwave Imaging

Microwave (MW) imaging and sensing systems can transmit electromagnetic waves inside dielectric materials safely and non-destructively, which makes them ideal for medical applications such as detection, diagnosis, classification, and monitoring tasks. MW systems characteristics which depend on tissue types and pathological conditions include the fact that their radiations are non-ionizing and show sensitivity to dielectric contrasts of the human body. This is typically achieved within the frequency range of 1 GHz to 15 GHz, depending on the specific medical task. The substantial difference in electrical characteristics between malignant tumor tissue and the surrounding normal tissue makes microwave imaging, especially with Ultrawide Band (UWB) technology, a promising method for medical applications, such as early breast cancer detection. Compared to other detection methods, UWB microwave imaging has several advantages, including high contrast capabilities, low cost, and anticipated safety. [7] The procedure is anticipated to be quick, precise and sensitive, making the examination safer and more comfortable for patients. There are however challenges regard the focusing of the electromagnetic waves inside of the body tissues. On the software side, delay-and-sum algorithm, a popular reconstruction

method, is valued for its intrinsic simplicity, resilience and efficiency in terms of computation time. However, several intricate obstacles must be overcome for this imaging system to be deployed successfully. Finding an incredibly accurate time-delay calculation for signals passing through a focal point between the transmitter and receiver is crucial to the algorithm's accuracy. Another important aspect to consider is the need to equalize tissue losses and the radial spread of the spherical wavefront to ensure that all received pulses are precisely time-aligned, and that their amplitude and shape are standardised, in order to improve image quality and eliminate errors.[7]

Furthermore, rather than simply encircling the target in one dimension, antennas must be tightly deployed in various planes of interest to produce high-quality, well-defined 3D tumour images.

The system is typically consisting of an array of sending and receiving probes that are uniformly distributed around Domain of Imaging (DoI), which are tasked with the emission of an incident electric field and reception a resultant modified field. Thereafter, a computational algorithm is applied to the acquired measurements in order to reconstruct a dielectric distribution of the scattering object. [8]

Stroke from an electromagnetic point of view

When an electric field E is introduced into a dielectric material, it generates a total displacement flux D determined by the complex permittivity (ε) of that material. It is described as $D = \varepsilon E$. The complex permittivity is a parameter where its real part defines the material's capability to store energy, while its imaginary part accounts for losses. Part of these losses are conductivity losses. For biological tissues, the primary determinant of dielectric characteristics, particularly their dependence on frequency, is their water content. Tissues rich in water, such as blood and healthy brain matter (both gray and white matter), show high variation in permittivity across frequencies. This is not the case for drier tissues like the bone [8].

The pathological event of a stroke introduces a local deviation in these established dielectric characteristics relative to the surrounding healthy brain matter. This deviation can be expressed as the dielectric contrast (χ), defined as the ratio of the difference between the relative complex permittivity of the tissue under examination (ε_r) and the background permittivity (ε_b) to the background permittivity itself: $\chi = (\varepsilon_r - \varepsilon_b)/\varepsilon_b$. [9] In this sense, the two primary stroke types can give us opposite values of this electromagnetic contrast. The majority of cases involve AIS, caused by a blockage impairing blood flow. Ischemic tissue is characterized by dielectric property values that are lower than the average background of the healthy brain. Consequently, the dielectric contrast in case of AIS has a real part lower than zero ($\mathrm{Re}(\Delta\chi) < 0$). [10] On the other side ICH is caused by leaking blood vessels and therefore involves the accumulation of blood. Haemorrhagic tissue, consisting largely of blood, exhibits higher permittivity and conductivity compared to the surrounding healthy brain tissue [9]. This means that an ICH case is associated with a positive sign in the real part of the dielectric contrast ($\mathrm{Re}(\Delta\chi) < 0$) [10]. These differing dielectric properties are crucial because they allow for the potential differentiation of the two pathological conditions based on the sign of the dielectric contrast [9].

From a purely theoretical perspective, these differences in complex permittivity mean

that the pathological area acts as a localized scattering object within the overall dielectric system of the head [8]. If we emitted microwaves in the brain system, the localized change in dielectric properties caused by the stroke would induce a perturbation of the excited electromagnetic field [10]. This measurable perturbation is directly related to the specific characteristics of the dielectric contrast ($\Delta\chi$). If this emission of microwaves was generated and received by a multitude of antennas, arranged around the brain in a matrix, we would be able to obtain the values of the scattering parameters.

Components of a Microwave Imaging System

Antennas serve as the probes surrounding the body that transmit and receive the electromagnetic energy. Their design greatly influences the capabilities of the system, as factors such as their shape, size, feeding method and the choice of matching medium material dictate how effectively they can convey EM radiation inside the body. Their operating frequency is key, as its choice always constitutes an inevitable trade-off: higher frequencies bring us a higher level of detail but limit our penetration capabilities. The contrary is of course also true. It is imperative to keep in mind the scale of the sensed body parts and their depth inside the DoI.

The transceiver component of the apparatus usually employs a **Vector Network Analyzer (VNA)**, which finds his purpose in the generation and collection of the MW signals. The VNA connects to the multi-probe array. It constitutes one of the the primary expenses in many experimental devices [8].

In the case that an array of radiators is connected to a VNA having a small number of ports, it is necessary for a switch matrix to be present. When an array apparatus uses electronic scanning, the scanning function is performed by electro-mechanical or solid-state RF switches.

The **switching matrix** can include signal interconnections provided by semi-rigid coaxial cables. The couplings are precisely manufactured so that each path from the VNA port to the radiators is of same electrical length. An alternative switch controller, backed with a source power, connects the script of settings for acquiring data to the switching matrix. Constraints related to switches are: insertion loss, power isolation and repeatability [8].

The imaging system utilizes a computational technique or inversion algorithm to process the data and reconstruct the dielectric distribution. Multi probe systems have a control unit for collecting the data of scattering parameters (S) of each radiator pair (i,j) so that an image can be obtained.

The image-reconstruction computations involve the measured data (either in frequency domain or time domain) and are based on pre-computed EM models of the sensing geometry. Imaging approaches can be roughly categorized into three categories: direct inversion approach, radar-based approach and quantitative tomography [8].

For a quantitative reconstruction of the DPs (relative permittivity and conductivity) from measured field values, iterative non-linear calculation methods can be used i.e., for example Contrast Source Inversion (CSI). This estimate is computed using typically a particular computation code, such as Finite Element Method (FEM) code for solving the inverse scattering question [9].

The S-parameters tell us how our signals work in an antenna system. They describe how much of an incident electromagnetic wave is reflected, transmitted, or absorbed by each port in a network. The S_{11} and S_{21} are the reflection coefficient of an antenna and the transmission coefficient between two antennas, respectively. These depend not only on the features of antennas themselves, such as their geometry or materials, but also on the medium between them. Boundaries between different DP materials change the propagation path of a wave, which changes the obtained S-parameters. This implies that changes in the brain, such as the scattering objects generated by stroke events, results in deviations from the expected transmitting and reflecting behaviours.

1.3 Thesis purpose, contributions and methodologies

The central research scope of this thesis is an antenna design and optimization strategy that can best minimize mutual coupling and back radiation while ensuring deep penetration and accurate imaging in a brain stroke monitoring device.

To this end, several contributions have been apported to the inquiry, starting with a comprehensive literature review on state-of-the-art antennas for microwave bio-imaging.

Five candidate antennas of different geometries have been modelled, systematically simulated and analysed using simplified a head phantom. The performance of these designs is assessed and documented in terms of reflection and transmission coefficients, radiation patterns and wave penetration.

A key contribution was the optimization of the horn double-ridged waveguide antenna, including geometrical parameters calibration and manufacturable filling material choice, resulting in a compact and high-performing design. Finally, the practical testing of the final design in a laboratory environment mark the true significance of the investigation and its value for real applications.

The methods used here combined computational, theoretical and experimental approaches. The first step is a literature-driven selection of candidate antennas. Then, electromagnetic simulations are carried out in CST Studio under simplified but plausible conditions; parametric sweeps are undertaken to refine its design. External prototyping, internal material manufacturing and virtual network analysis were then used for the experimental phase of the research. Such an integrated approach both ensures that the proposed antenna design is based on an appropriate theoretical foundation while also providing practical guidance for its execution in applications involving medical imaging.

Chapter 2

Antenna Review

2.1 Requirements Definition

Given the small space gap between each of the 22 antennas on the patient's head, it is beneficial that the sensors emit the least amount of radiation possible in the lateral direction to avoid coupling between nearby antennas. Such coupling is undesirable because it means that part of the transmitted energy is directly received by neighbouring antennas without passing through the tissue. These redundant signals can introduce artifacts and compromise the quality of the reconstructed images. An additional requirement of the same importance is that the antennas avoid irradiating as much as possible in the backward direction. Waves propagating in the space around and away from the head are susceptible to external interference, which the reconstruction algorithm cannot take into account, potentially introducing errors in the reconstructed image. For these reasons a literature review has been conducted with the aim of finding existing antennas designed for microwave brain imaging, that offer features suitable for the tightly packed sensor environment of the helmet device. Several factors have been taken into account, such as near-field radiation pattern, return loss at relevant frequencies, manufacturing costs and simplicity. A summary of the qualities needed can be defined as:

- Operation at lower frequencies: Improves penetration of electromagnetic waves (EM) into biological tissues, which are highly dissipative at high frequencies. The perfect range stands between 0.8 and 1 GHz.
- Wideband: Essential to achieve high image resolution and fast data transmission.
- Directivity and unidirectional radiation: Important to focus energy on the target tissue, improve the signal-to-noise ratio (SNR), and reduce unwanted reflections from the surroundings.
- Compact size: Allow integration into arrays with enough elements for proper spatial sampling, while also ensuring system portability.
- On-body adaptation (in contact with the body): Reduces signal loss at the air-skin interface and improves energy coupling into biological tissues.

2.2 The Selected Papers

A starting pool of 28 antennas was selected. They were divided into planar antennas (patch and slotted), bowtie antennas, horn waveguide antennas, and dipole antennas. The minimum working frequency of this pool of antennas was found to be 0.4GHz, while the maximum working frequency and the average working frequency are 20 GHz and 3.4 GHz, respectively. A significant portion of them are planar antennas. These antennas are popular in brain imaging research due to their ease of fabrication and low profile. In the following, each study is briefly described, and all literature references are summarized in Table 1.

Table 1: Summary of antennas used in tissue imaging.

Ref	Type of Antenna	Overall Dimension (mm)	Application	Operating Frequency Band	Substrate Material	Matching Medium	Metamaterials / Metasurfaces
[11]	Planar (Patch) Antenna	60×60	Breast cancer detection	~ 2.45 GHz	FR-4	Quasi crystal, $\varepsilon = 2.2$	AMC
[12]	Planar (Patch) Antenna	$29.4 \times 29.4 \times 25$	Breast cancer detection	3–12 GHz	FR-4	None	None
[13]	Planar (Patch) Antenna	50×50	Breast, lung, brain cancer detection	2–5 GHz (AMC at 4.75 GHz)	FR-4	None	AMC, Metamaterial-based Lens
[14]	Planar (Patch) Antenna	Diameter 75, thickness 8	Deep torso imaging	0.64–2.22 GHz	Wangling TP-1	None	None
[15]	Multiple Dipole	42×36 at $\lambda_0 = 0.55$ GHz	Brain imaging	0.6–3.0 GHz	PCB, $\varepsilon_r = 10.2$	Gel	None
[16]	Multiple Dipole	34×24	Brain imaging	0.5–1.5 GHz	Rogers 3010	Gel	None
[17]	Dielectric Filled Horn Antenna	54×34	General tissue imaging	1.85–3.1 GHz	Rogers RO3210, Taconic RF-60A	GRIN lens filling	GRIN Metasurface lens
[18]	Planar (Log Periodic) Antenna	91×64	Brain imaging	0.5–3 GHz	FR-4	None	None
[19]	Dipole Antenna	60×60	Brain imaging	0.4–2.5 GHz	Substrates, $\varepsilon_r = 3.55$	Liquid	None
[20]	Planar (Patch) Antenna	79×69	Breast cancer detection	2.89–7.0 GHz	Felt	None	None
[21]	Planar (Patch) Antenna	36×36	Knee imaging	0.7–3.3 GHz	Felt	Wool-felt	–
[22]	Dipole Antenna	50×40 at $\lambda_0 = 1$ GHz	Brain imaging	1–4.3 GHz	PDMS	None	None
[23]	Planar (Patch) Antenna	30×30 at $\lambda_0 = 0.55$ GHz	Brain imaging	0.55–0.7 GHz	RTV silicone	None	None
[24]	Planar (Patch) Antenna	28×26	Brain imaging	0.6–2.5 GHz	RTV silicone	Flexible solid	None

[25]	Planar (Patch) Antenna	68×68	Brain imaging	1.0–1.7 GHz	FR-4	None	None
[26]	Dielectric Filled Horn Antenna	$43 \times 30 \times 41$	General tissue imaging	0.5–3.0 GHz	3D-printed horn, fillers (cornflour, gelatin, water)	Filling material	None
[27]	Planar (Patch) Antenna	60×85 at $\lambda_0 = 1.45$ GHz	Brain imaging	1.16–1.94 GHz	PDMS	Flexible solid	Metamaterial unit cells array
[28]	Planar (Patch) Antenna	76×44	Breast cancer detection	2.9–7.8 GHz	FR-4	None	AMC
[29]	Planar (Patch) Antenna	55×40	Breast cancer detection	3–10 GHz	FR-4	None	None
[30]	Planar (Bowtie) Antenna	30×30	Breast cancer detection	0.5–2.0 GHz	Rogers RT6010	None	None
[31]	Dielectric Filled Horn Antenna	16×11	General tissue imaging	1.5–5.0 GHz	Ceramic horn	Filling material	None
[32]	Dielectric Filled Horn Antenna	74×30	Breast cancer detection	3.1–10.6 GHz	Eccostock HiK horn	Filling material	None
[33]	Planar (Patch) Antenna	30×24	Breast cancer detection	3–20 GHz	FR-4	None	None
[34]	Planar (Bowtie) Antenna	60×44	General tissue imaging	3–11.7 GHz	FR-4	None	None
[35]	Dipole Antenna	120×120	Wireless communications	1.85–2.89 GHz	Metal structure	None	None
[36]	Planar (Bowtie) Antenna	60×60	Brain imaging	1–6 GHz	Rogers RO4003C	None	None
[37]	Planar (Slot) Array	Not specified	Breast cancer detection	3–8 GHz	Multilayer PCB	None	None
[38]	Dipole Antenna	70×30	Brain imaging	1.12–2.50 GHz	Rogers RT5880	None	Metamaterial unit cells array

[11] Quasi Crystal based Circular Patch Antenna with Artificial Magnetic Conductor for Breast Cancer Detection

This study shows the design and computational testing of a circular microstrip patch antenna equipped with an Artificial Magnetic Conductor (AMC) and a Penrose quasi-crystal pattern. The main goal of this study is to develop a new method for detecting malignant tissue in the breast, extrapolating its pocision in a precise way, while keeping the SAR low to protect the patient. For this reason the antenna is designed to work at 2.45 GHz. The antenna uses an FR-4 substrate. The top patch and the bottom ground plane are made of copper, a cheap and very conductive material. The AMC is a metamaterial, a planar periodic structure that is placed behind the antenna and behaves like a perfect magnetic conductor (PMC). At its resonant frequency, it gives a reflection phase of zero degrees. The importance of the AMC is mainly its ability to stop surface waves. Where these waves contribute to a wider radiation pattern, the presence of the AMC reduces side lobes and makes the beam more focused. The Penrose quasi-crystal helps to focus the electromagnetic waves in a narrow direction: scattering parameters S11 and S22 are better when the quasi-crystal is used. The main limitations of this study stem from the fact that AMC and quasi-crystals improve performance, but the design and fabrication are not simple. Including these structures in a complete device could be a challenge. Furthermore, the computational nature of the study limits the results to the simulation domain, without any testing of a physical prototype.

[12] UWB Antenna with Enhanced Directivity for Applications in Microwave Medical Imaging.

This study focuses on improving the directivity of a compact UWB antennas for Microwave Medical Imaging (MMI).The work proposes a slot patch antenna. It is modified with a metal reflector inspired by the Yagi-Uda design. This turns it into a Reflector Loaded Antenna (RLA). The aim is to develop a simple and general technique to convert many non-directional UWB antennas into directional ones, without reducing other key features such as bandwidth, efficiency, and time-domain response. This is important for tumor detection and localization in different body regions as the breast, which is the region of choice for the simulations performed in this study.The authors tested three antenna setups. First, they used a basic antenna without a reflector. Then, they added a reflector to see if it improved the signal. Finally, they tried the same idea on a different antenna type. This helped show that the reflector works well and can be used with different designs. The proposed RLA shows clear improvements in gain and directivity compared to the non-directional reference antenna. The transmitted field inside a human breast model increases by 14.26 dB. The antenna keeps the input signals almost unchanged in the time domain, with a high correlation factor of 94.86%. Furthermore, it keeps the same bandwidth as the reference antenna.

[13] Design and experimental validation of a metamaterial-based sensor for microwave imaging in breast, lung, and brain cancer detection

This study details the development of a microstrip sensor for the advanced detection of breast, lung, and brain cancers. The sensor's architecture combines a microstrip patch antenna fed by a coplanar waveguide (CPW), a metamaterial (MTM) lens positioned on the backside, and an artificial magnetic conductor (AMC) added as additional substrate at 15 mm from the main one. The antenna is fabricated on a 1.52 mm thick FR4 laminate with a dielectric constant of 4.3. The MTM lens is used to focus the waves toward the top surface of the AMC, and the AMC performs as a perfect wave reflector. Both metamaterial components are formed from arrays of unit cells with specific geometric shapes. At the resonance frequency of 4.56 GHz, the realized gain reaches 8.5 dBi, which includes a 3.8 dBi enhancement attributable to the AMC. The usable bandwidth spans 2.5 to 4.75 GHz. Experimental tests with breast, lung, and brain phantoms showed the design's ability to clearly detect tumor sizes. The AMC's negative-epsilon characteristic also contributes to improved impedance matching. Finally, the AMC's radiation pattern reduces rearward radiation, which in turn minimizes the noise level during the imaging process. The design was validated on brain, lung and breast cancer, showing its ability to detect tumors from 2 to 4 mm in size. The versatility of this antenna makes it a valuable sensor for medical purposes, but its high frequency range poses doubts about its applicability in stroke monitoring contexts, and the manufacturing of the metamaterials included in its structure would require a complex optimization process.

[14] Dual-Sense Circularly Polarized Substrate Integrated Waveguide Antenna for Deep Torso Imaging

The authors designed an antenna for thoracic imaging which is compact and incorporates dual sense circular polarization (CP). The design starts with a single-polarization antenna of circular shape which features a square patch and uses the SIW technique for better penetration of EM wave into the torso. To maintain compactness, sleeved feeding and slow wave feeding techniques are used to increase the bandwidth of CP. The final dual-sense CP antennas use dual feeds with both RHCP and LHCP polarization. They are fed using dual-port circular feeds, using Wangling TP-1 substrate with ε r = 25, thickness of 8 mm, and a tan δ = 0.0025. The SIW wall is formed by 36 metallized vias around the edge of the substrate. Operating frequency range is 0.64-2.22 GHz with fractional bandwidth (FBW) of 107%. 75 mm diameter and 8 mm in height, structural thickness is $0.15\lambda^3$.The focus is to address the issues created by the torso's heterogeneous anatomy and its sizeable dimensions, along with the need to image the deeply situated organs like the lungs and the liver, which demand a compact, low-profile antenna with wide bandwidth and the capability to efficiently focus low-power EM wave penetration. It is practical for clinical use, too, with a 75 mm diameter and 8 mm thickness. The bandwidth of 0.64-2.22 GHz provides a good balance between penetration at lower frequencies and resolution at higher frequencies. This work demonstrates an effective design and feeding technique solutions to the structural difficulties of torso imaging.

[15] Detection Capability Enhanced Biosensor Antenna for Portable Electromagnetic Stroke Diagnostic Systems

The authors present a planar compact antenna for biosensing, designed for portable EM stroke diagnostic systems. The antenna is based on multiple dipoles, showing multi-mode resonance and complementary interactions. The geometry of the antenna was achieved using three identical PCB circuits with a relative permittivity of 10.2. At the centre of the antenna two shorted patches were placed, similar to a bowtie shape, manufactured with triangular patches and metallic vias. Two half-wavelength electric dipoles are connected to the sides. Innovative T-connectors connect the dipoles, ensuring in-phase excitation for directional radiation. The power supply is differential, consisting of two 50 Ohm microstrip lines. The antenna covers a wide frequency band from 0.5 GHz to 3.0 GHz. It features unidirectional radiation patterns with high front-to-back ratios (FBRs) exceeding 13.5 dB in the near-field region. The overall dimensions are compact, equal to $0.07\lambda 0 \times 0.06\lambda 0 \times 0.0125\lambda 0$, where $\lambda 0$ is the free-space wavelength at the lowest operating frequency. The authors aim to enhance both the bandwidth and the depth of penetration of the EM radiation of current devices. A 12-element array was tested numerically and on experimental head phantoms (liquid and semi-solid) with stroke-emulating inserts, demonstrating the detection of stroke-affected areas as small as 3 mm in radius and the ability to detect multiple bleeding areas experimentally. Unidirectional radiation patterns with high FBRs (greater than 13.5 dB) maximize energy directed at the target and reduce interference. The antenna's sensitivity to air gaps between the antenna and the head phantom can degrade impedance matching, making good contact or the use of matching material crucial. The complex geometry with multiple dielectric layers and metal vias, while functional, could increase the difficulty of precision manufacturing.

[16] An Antenna Array Based on Radar Operation with High Detection Capability and Implementability for Three-Dimensional Head Imaging

The following paper presents a printed magnetoelectric (ME) dipole antenna. The structure combines a shorting bow-tie patch acting as a magnetic dipole with two electric dipoles fabricated on a Rogers 3010 substrate ($\epsilon r = 10.2$). The power supply is differential, and the reported dimensions are 34 mm × 10.2 mm considering the upper patch, with a 2.5 mm metal cavity height. This design is conceived to operate in the 0.5–1.5 GHz band. The author's aim is to develop a radar-based 3D head imaging platform with high capability for detecting small internal variations: to this end the configuration uses multistatic acquisitions with a VNA and reconstruction via DAS beamforming. This is based on differential matrices obtained from subsequent measurements. A 24-element array architecture on a plastic support is implemented by Chen et all., with an inter-element coupling of approximately -20 dB across the array. The system demonstrates high sensitivity: simulated volumes as little as 2.14 cm^3 are sensed with localization errors inferior to 5.67 mm. The reconstruction maintains a maximum intensity ratio (MIR) than 1, in the presence of noise with a SNR up to 20 dB, indicating robustness. The resolution

remains inferior to medical tomographic techniques such as CT/MRI. The accuracy depends on antenna-to-skin contact, a problem that the authors approached with the use of a dielectric gel. In conclusion this design seems to deliver a solid performance, at the price of a complex geometry that is potentially challenging to manufacture.

[17] Design of Highly Directive GRIN MS Lens Integrated DFHA for Deep Tissue Biomedical Imaging

Paul et all. In this study aim at the development of a dielectric filled horn antenna for deep tissue imaging. Their main objective is to achieve deeper electrical field penetration and to enhance the spatial resolution for tumor detection. Their design strategy revolves around the use of a gradient refractive index (GRIN) metasurface lens. This is essentially a structure featuring periodic elements that vary in their geometric properties, allowing a spatial distribution of the refractive index across the aperture to achieve a high impedance matching and directivity. The GRIN lens is composed of different modules, each one with its own pattern of unit cells. Two different configurations have been tested on a torso digital phantom. In the first one a Core Layer (CL) stands between two Impedance Matching Layers (IMLs). In the second one a CL stands before an IML, followed by an Impedance Body Matching Layer (IBML), eliminating the need for an extra dielectric between lens and tissue. Configuration 1 was also experimentally tested. In both computational and physical testing two antennas were placed at the ends of the phantom, inside of which an artificial tumor resided. Reconstructed images show that the integrated system accurately localizes the tumor. Compared to the conventional DFHA, the GRIN lens assisted antenna achieved 12 dB higher penetration at 100 mm. Reconstructed images show clearer tumor borders. The length of the antenna is however considerable, as the GRIN lens add an additional 19 mm to the 70 mm antenna. Such a size could prove challenging for the array of the final device, and the metamaterials of the lens are hard to optimize for a different working band.

[18] Design of Low-Profile Ultrawideband Conformal Array Antennas for Microwave Brain Imagers

A low profile, double layer folded log periodic radiating element for conformal ultrawideband brain imaging is presented in this paper. A thin plastic supporter with relative permittivity of 3.5 and supporter with a thickness of 3 mm supports the radiator's compact and mechanically straightforward main radiating element, which measures 91 $\times$ 64 $\times$ 1 mm^3. According to the authors simulations, the antenna offers an ultrawideband response with a simulated reflection coefficient that spans roughly 0.5 GHz to 3.0 GHz. The design is appropriate for close fitting, conformal arrays around irregular surfaces like a head because of its small thickness (1 mm radiator on a 3 mm supporter) and folded log periodic geometry, which maintain ultrawideband behavior while keeping the profile low. A brain-matched glycerol–water mixture with relative permittivity of around 40 for tissue loading was used in the experiments. The reflection coefficient and port isolation were

measured using a Keysight vector network analyzer. A polygonal plastic container containing a glycerol–water mixture was used as the experimental phantom to mimic brain dielectric loading. S11 resonances shifted, the measured -10 dB bandwidth and front to back ratio decreased, backlobes and cross polarization increased at higher frequencies, and mutual coupling increased at the low end when elements were near the phantom, according to measured results that differed slightly from simulations.

[19] An On-Body Matched Differentially Fed Magnetoelectric Dipole Antenna for Head Imaging Systems

Chen et all. suggest an on-body matched, differentially fed magnetoelectric (ME) dipole antenna for use in microwave head imaging systems meant to identify intracranial hemorrhage (ICH). The authors tried to overcome the shortcomings of existing microwave imaging antennas by developing a compact, wideband solution that could reliably couple energy into head tissues. The antenna's 137% wide impedance bandwidth (0.45–2.4 GHz) allows for fine imaging resolution at higher frequencies and deep penetration at lower frequencies, according to the authors. There is less interference from the environment because the front-to-back ratio (FBR) is higher than 18 dB throughout the band.The specific absorption rate (SAR) stayed well within IEEE limits at less than 0.82 W/kg. An antenna array of eight elements was built into a head imaging system and used for validation. Physical experiments verified detection down to 5 mm radius, while simulations showed detection of bleeding areas as small as 3 mm radius. A strong contrast between hemorrhage and background tissues and high localization accuracy were demonstrated with quantitative imaging. Localization errors were inferior to 3.6 mm. Experimental results closely matched simulations. The authors admit some drawbacks despite these encouraging findings. Reliance on matching liquid may restrict portability and make system integration more difficult. Moreover, similarly to other antennas of the same kind, optimization and manufacturing could prove quite challenging for the purposes of the Wavision Research Group.

[20] Directional Wideband Wearable Antenna with Circular Parasitic Element for Microwave Imaging Application

In order to detect breast cancer using microwave imaging, the authors propose the use of a directional, wideband, wearable antenna with a dual-layer, coplanar waveguide (CPW) design and a circular parasitic element. This aims to address the limitations of traditional screening techniques such as mammography and MRI. These techniques can be expensive, invasive or inaccurate, with false-positive rates of up to 60–70The design process comprised three stages (Design A, B and C). Design C, the final stage, achieved resonance across 2.89–7.00 GHz and a bandwidth of 4.11 GHz centred at 5.15 GHz. Important performance metrics that demonstrate a notable improvement over earlier iterations include a gain of 5.51 dBi and an FBR of 11.36 dB. The antenna was constructed using felt (with a relative permittivity of 1.45) as the substrate and ShieldIt Super™ as the conductor, in order to ensure flexibility and cost-effectiveness. The simulated wideband operation

was confirmed through physical testing. Measurements revealed an impedance bandwidth ranging from 3.06 to 7.00 GHz. However, due to connector losses, substrate inhomogeneity and fabrication errors, these values were somewhat lower than those predicted by the simulations. The radiation patterns consistently exhibited stable unidirectional lobes with reduced back radiation in both the simulation and the measurement. The authors point out that the larger size of the antenna is a result of the low dielectric constant of textile substrates and the unpredictability that comes with manual fabrication. Furthermore, real-world challenges still include connector integration and substrate homogeneity.

[21] Wearable Dual Polarized Electromagnetic Knee Imaging System

Driven by the need for portable, on-site diagnostic tools to supplement or replace the expensive and impractical MRI scanner, which is not suitable for routine monitoring, Sultan and Abbosh's paper presents a wearable, dual-polarised electromagnetic imaging (EMI) system for detecting knee injuries. The authors aimed to create a small, textile-integrated antenna array that could identify ligament tears by taking advantage of the dielectric contrasts brought on by the buildup of synovial fluid. The suggested system comprises an eight-element dual-polarised aperture antenna array, with each element measuring 36 $\times$ 36 $\times$ 3.1 mm^3 and supported by a ground plane for unidirectional radiation. With a front-to-back ratio of over 10 dB and more than 20 dB of isolation between the vertical and horizontal ports, the array operates over a bandwidth of 0.7–3.3 GHz (130%). With a maximum specific absorption rate (SAR) of 0.183 W/kg at 10 dBm input power, the system notably conforms with safety regulations, being significantly below the IEEE limit of 2 W/kg. A penetration efficiency of >80% guarantees adequate field interaction with knee tissues. Both numerical validation (using realistic voxel knee models and CST simulations) and experimental validation (using liquid and durable phantoms) were performed. Despite minor frequency shifts caused by variations in the dielectric properties of the fabricated and analytical phantoms, the measured S-parameters showed good agreement with the simulations. According to reconstructed images, the dual polarised system performed better than single polarised designs, especially for slant or irregularly shaped injuries. It produced better signal-to-clutter ratios (SCR >0 dB), lower localisation error and higher contrast ratios (CR > 1). However, the authors acknowledge their limitations. Depolarisation effects in heterogeneous tissues reduce isolation in realistic phantoms (down to 17 dB compared to 23 dB in homogeneous models) and the brace needs careful calibration to account for this.

[22] Compact Unidirectional Conformal Antenna Based on Flexible High-Permittivity Custom-Made Substrate for Wearable Wideband Electromagnetic Head Imaging System

Alqadami et al. present the design and validation of a compact conformal wideband unidirectional antenna for wearable electromagnetic (EM) head imaging systems in their paper. The authors aimed to developing a flexible, high-permittivity substrate that would

allow miniaturisation while preserving robustness and tissue compatibility. The custom substrate was created by combining poly-dimethylsiloxane (PDMS) with AlO3 powders and graphite in different ratios. Dielectric characterisation revealed adjustable properties. For example, a ratio of 7.5:2.4:0.1 produced a loss tangent of 0.028 and an average relative permittivity of 14.7 across 1–4 GHz. This enabled the antenna to be small, but remain flexible enough to fit the shape of a human head. The antenna operated electromagnetically as both electric and magnetic dipoles in various bands using a combination of multi-slot planar radiators and four shorting pins. Simulations predicted a broad operating bandwidth of 0.93–4.65 GHz with VSWR < 2.6. Physical testing on a SAM head phantom verified a measured reflection coefficient (S11) bandwidth of 1–4.3 GHz, or a 124% fractional bandwidth. The slight difference between the measured and simulated cutoffs (0.65 vs. 4.3 GHz and 0.93 vs. 1 GHz) was attributed to fabrication tolerances and changes in tissue properties. Promising performance metrics included penetration depths of up to 70 mm at 1.2–1.5 GHz, sufficient to reach deep brain regions. The clinical potential was demonstrated through the successful reconstruction of images of targets inside a realistic head phantom using an array of 13 antennas. However, there are still drawbacks. Higher AlO3 loading reduces the flexibility of the substrate, while higher graphite content increases losses. Although the antenna reduces skin-air reflections, calibration in clinical settings may still be difficult due to the unpredictability inherent in manual fabrication.

[23] Compact Flexible Wideband Antenna for On-Body Electromagnetic Medical Diagnostic Systems

The paper by Alqadami and associates presents a compact, flexible, wideband antenna designed specifically for biomedical diagnostic applications. Like other flexible antennas discussed in this review, its purpose is to achieve high imaging accuracy while ensuring close adherence to the human body. This is because traditional rigid antennas often lack adaptability to curved surfaces and have a limited bandwidth, which clearly restricts their use in imaging scenarios such as ours. The authors propose a design featuring an annular ring structure with a capacitive gap and a shorted parasitic element. The silicone-based substrate used to manufacture this antenna ensures both mechanical flexibility and biocompatibility. With dimensions of only $0.055\lambda 0 \times 0.055\lambda 0 \times 0.009\lambda 0$ at 0.55 GHz, the antenna is 80% smaller than conventional designs. With a fractional bandwidth of 138% measured across the 0.55–3 GHz range, the antenna can operate in multiple bands, making it suitable for various diagnostic applications. Its radiation properties are also noteworthy due to its unidirectional near-field pattern and front-to-back ratio of over 10 dB, ensuring efficient penetration of biological tissues. In terms of safety, the specific absorption rate values remain below 0.8 W/kg at an input power of 10 dBm. This exceeds the IEEE guidelines. The simulated performance was furthermore investigated through physical testing on human volunteers. In line with the CST simulations, measurements taken from the head and arm revealed operational bands of 0.54–3.1 GHz and 0.57–2.9 GHz. The antenna's suitability for biomedical imaging was confirmed by the close correlation between the near-field radiation patterns. The performance is sensitive to tissue variability and bending, with slight frequency shifts observed across various body models. Silicone substrates offer flexibility but their durability and suitability for large-scale production

are problematic.

[24] Flexible Electromagnetic Cap for Head Imaging

This paper presents a wideband, wearable electromagnetic system for the rapid detection of strokes. The authors aim to address three main drawbacks of traditional imaging modalities such as MRI and CT: cost, accessibility and time consumption. To reduce mismatch between the impedance of the antenna and that of the skin, they have incorporated a 16-element flexible multi-slot planar antenna array into a lightweight silicone cap. The system includes a high-permittivity matching layer. The proposed antenna appears to demonstrate several key performance indicators. The authors report that the sensor provides both penetration depth and image resolution when operating within the wideband frequency range of 0.6–2.5 GHz. Near-field radiation achieves a front-to-back ratio of at least 11 dB, confirming unidirectional energy delivery to head tissues. Meanwhile, reflection coefficient values remain below -7 dB. Interestingly, with an input power of under 10 dBm, the antenna maintains a fidelity factor of at least 90%. This is the generally accepted threshold for minimal signal distortion. It also meets safety standards, with SAR values of less than 1 W/kg. With a dielectric permittivity of around 50 at 0.5 GHz, the flexible matching layer improves conformity further and mitigates the impact of air gaps resulting from hair or anatomical variation. Homogeneous tissue models and realistic head phantoms were employed for experimental validation. In both cases, the system identified the objects that emulated stroke, and the reconstructed images closely matched the ground truths. Physical measurements of reflection coefficients (S11) taken from human volunteers and phantoms appear to be in line with the same values that the authors derived with their CST simulations. This confirms the robustness and repeatability of the method in a curved state.

[25] Compact 3-D Antenna for Medical Diagnosis

The authors present a folded structure cavity-backed antenna designed specifically for microwave head diagnostics. They aimed to overcome the limitations of reflection-based microwave imaging, which has poor signal penetration and low signal-to-noise ratios due to the dielectric properties of human tissue. To outperform previous designs in terms of penetration, directionality and specific absorption rate (SAR), they proposed a folded, inverted-F-like structure with a slot-loaded ground plane. Remarkably small, the antenna measures $0.23\ \lambda \times 0.23\lambda \times 0.04\lambda$ in relation to the lowest operating frequency. Operating in the 1–1.7 GHz band, it strikes a balance between penetration depth and controllable tissue losses. Crucially, the antenna achieves a front-to-back ratio (FBR) of over 17 dB, ensuring that radiation is concentrated on the head rather than being wasted in the surrounding area. The maximum measured specific absorption rate (SAR) value was 0.0147 W/kg (10 g) at 1.45 GHz, which is significantly lower than that reported for comparable antennas in the literature and two orders of magnitude below the IEEE safety limit of 1.6 W/kg. Physical testing was conducted using a manufactured three-layer phantom (skin, bone and brain), and the results were compared to simulations using a head model. The simulated bandwidth was 1.03–1.7 GHz, while the measured bandwidth

was slightly wider at 0.9–1.8 GHz, indicating good agreement. There were symmetrical E- and H-plane responses, stable main beams and consistent radiation patterns. Overall, the antenna showed good penetration and low SAR in both situations, with only slight variations ascribed to material uncertainties and phantom simplifications.

[26] 3-D Printed UWB Microwave Bodyscope for Biomedical Measurements

This paper presents a 3d printed double ridge horn designed for generale body microwave imaging. Like many horn antennas it is filled with a dielectric material, in this case a mixture of water, flour and gelatine that is specifically mixed to present the average relative permittivity and conductivity of the white and grey matter in the brain. Such relative permittivity is 50. It maintains compact dimensions at $43 \times 30 \times 41\,\text{mm}^3$. Its -7 dB bandwidth was measured by the authors to extend between 0.5 and 3 GHz, which should guarantee a usable performance fit for a general purpose, which is the purpose of Rashid et all.. It was validated through computer simulations on a box phantom mimicking the human head, and then experimentally validated on a physical twin of the same phantom. The phantom included a metallic cylinder at 10cm, that was successfully located by the sensor. The electric file plots show a promising directivity at higher frequencies, but its general purpose nature may hinder its good matching with head tissues, and the gelatine material is not prone to be conserved for long periods of time.

[27] Wearable Electromagnetic Head Imaging System Using Flexible Wideband Antenna Array Based on Polymer Technology for Brain Stroke Diagnosis

The authors of the paper propose a flexible wideband antenna array with the purpose of a rapid, portable and non-ionizing stroke diagnosis. The array consists of a radiating element of 4×4 radiating patches equipped with open-ended U-slots. Around them on the same plane we find a series of electromagnetic bandgap cells, while on the back side of the array a 4×4 metamaterial cell array contributes to a unidirectional radiation. The substrate used is PDMS polymer, fundamental for a flexible structure capable of adapting to the head's surface. The overall size of the array is $60 \times 85 \times 4$ mm3. The bandwidth is between 1.16 and 1.95 GHz, which is to the ideal 0.8-1 GHz range for the Wavision group. The system was tested on both realistic digital and physical target, and both simulated and measured radiation patterns show good directivity. It is however important to notice that the array manufacturing poses many challenges due to its complexity of assembly, multi layered structure and use of metamaterials. Moreover, the normalized E-field distribution on the realistic head model highlights modest but still present superficial waves.

[28] Microwave Imaging for Breast Tumor Detection using Uniplanar AMC Based CPW-Fed Microstrip Antenna

This work revolves around a microwave imaging system designed for the detection of breast tumor. The antenna of choice is a coplanar waveguide fed patch antenna, featuring an oval shaped microstrip. The structure of the antenna is built on a an inner layer of Rogers RO4003C and an inner FR4 substrate with a thickness of 1.6 mm, incorporated with a double layer of Artificial Magnetic Conductor (AMC). This AMC is achieved through a 5x5 array of unit cells and is intended to enhance directivity. The operative band was shown to be between 2.9 and 7.8 GHz, a frequency range in line with breast imaging devices, but sensibly higher than the usual intervals for brain imaging. Its directivity was tested in both simulations and anechoic chamber, yielding a quite narrow beam when using the AMC, but much more isotropic without it. Imaging of tumor-like objects was performed on real breast phantoms with a variety of techniques. The antenna features a good performance but it seems to be based mostly on the properties of the AMC, which would require significant redesign to adapt to a much lower frequency.

[29] Development of an ultra-wideband, stable and high-directive monopole disc antenna for radar-based microwave imaging of breast cancer

Celik et all. present a monopole patch disc antenna intended for breas cancer imaging. The paper reports the design process consists of four different versions of the sensor. In the last iteration an L-shaped slotted ground and a parasitic element are present. The triangular slot is designed to improve impedance matching and extend the bandwidth, while the parasitic element acts as a resonator to increase directivity in the intended direction. The antenna was tested only in free air to verify the directivity, which appears to be very high. The beam direction is stable over a large range of frequencies, from 3 to 10 GHz. The substrate size is 55×40 mm^2 and is made of FR4. The antenna presents itself as an easy manufacturable sensor, but it was unfortunately not tested on phantoms, and the simulated and measured results seem to diverge significantly.

[30] A compact double-layer on-body matched bowtie antenna for medical diagnosis

The authors of the paper designed a compact double-layer bowtie antenna intended to be used for various medical imaging purposes, especially breast cancer and stroke diagnosis. The purpose of this project is to enhance the reflections from abnormal volumes inside the body. The structure of the antenna is based on a double substrate of RT6010 with a relative permittivity of 10.2 and a thickness of 1.27mm. The top of the device features a folded bowtie geometry, which reaches the backside hosting a meandered microstrip line. This microstrip aims to extend the electrical length at low frequencies. The footprint is a compact 30x30 mm, which is a very suitable size for a device that contains a large number of tightly packed antennas. Li et all designed the sensor to have a wide bandwidth going from 0.5 to 2 GHz. This is to grant a finer imaging resolution. The front to back ratio is

greater than 9:1. The antenna was tested on both physical and digital phantoms, showing promising pairing with the body-simulating materials. The operative frequencies cover the interval important for the wavision device, but optimization could prove challenging.

[31] Ultra-wideband Miniaturised High Permittivity-Matched Antennas for Biomedical Diagnostic

Clemente et all. present a miniaturised ceramic double-ridged horn antenna purposed for breast cancer detection and possibly different forms of medical diagnosis. The main aim of the sensor designed by the authors is the achievement of an extremely compact antenna, which in fact has an aperture of 16x11 mm. The structure is a metallised ceramic body equipped with ridges of exponential profile. The advantage of choosing the ceramic base is the manufacturing though pressing and sintering. The directivity is very high, as often seen in horn antennas: the gain is about 8dBi, and the beawidth is around 60° in both planes. The physical testing was performed inside a basin of de-ionised water, which acts as an anechoic environment. The frequency range is between 1.5 and 5 GHz. A possible drawback of the miniaturization is that dielectric scaling reduced the input impedance to 15 Ohm, causing mismatch with standard 50 Ohm equipment.

[32] Near-field microwave imaging based on aperture raster scanning with TEM horn antennas

The authors of the paper present an ultrawideband TEM horn antenna designed for planar scanning and breast tumour detection. The antenna is made of two copper plates forming a horn open on its sides. The aperture is 19x30 mm, and is filled with three pieces of ECCOSTOCK HiK dielectric glued together. This dielectric material has a relative permittivity around 10, designed to match the dense breast tissue permittivity. On top of the upper copper plate, a microwave absorbing layer ECCOSORB FGM-40 is glued to isolate it from external electro-magnetic fields. This configuration offers a wide band under the -10dB line, going from 3.1 to 10.6 GHz. Digital computation of the directivity showed that 93 percent of the radiated power is directed through the front aperture into the tissue. Imaging trial were carried out both digitally an physically. A compressed breast was simulated with tumors inside of various shape, an those shape were reconstructed with reliable accuracy at 5-7GHz. The same test was conducted on glycerin based homogeneous phantoms. The sensor is clinically promising, but would require many optimizations to adapt it to brain stroke monitoring.

[33] Novel Ultra-Wideband Directional Antennas for Microwave Breast Cancer Detection

This work from Esuola et all. discusses two elliptical patch antennas. The context of development is breast cancer detection, and the main goal of the authors is the creation of a very compact antenna capable of operating over an ultrawide bandwidth. Both antennas have an elliptical patch on the front connected to a microstrip feed. This patch

is laid upon an FR4 substrate with a relative permittivity of 3.9, which features on its back a ground plane with two slots. Thisis where the two designs differ: the first one has two slots place of 9.9 mm at 45°, while the second one has two parallel vertical slots of 14 mm. Both designs have a size of 30 × 28 × 1.6 mm, so they are compact while maintaining a very wide frequency range between 3 and 20 GHz under the -10dB band. Both designs have a max directivity gain of almost 9 dBi, but a t higher frequencies side lobes increase. The antennas were purely simulated, and possible discrepancies with the real world are yet to verify.

[34] A high-directive bowtie radar antenna with a pyramidal reflector for ultra wideband radar imaging applications

The authors propose a bowtie antenna equipped with a pyramidal reflector mounted behind the radiating bowtie element. The main purpose of this element, which has a depth of 20 mm, is to increase the front to back radiation ratio, enabling ultrawideband general radar imaging, as the radar approach greatly benefits from unidirectional radiation. The bowtie element is not triangular but horn shaped, and it's built on an FR4 substrate with a footprint of 48x32 mm2 and a thickness of 1.6 mm. The antenna was tested in an anechoic chamber, which established that the back reflector allows for a gain directivity of 8.5 dBi. Unfortunately, the antenna was not tested on phantoms emulating the human body, as it seems not intended for medical applications. The frequency range in free space is from 3 to 10.8 GHz. Directivity plots offer the view of a very directional radiation, but the higher frequencies of the band suggest a splinting of the beam. The antenna structure is compact and easy to manufacture, but in its current state it is not optimized for body tissues and differences between simulations and measurements seems not to be negligible.

[35] A New Wideband Unidirectional Antenna Element

In this paper the authors are presenting a wideband unidirectional antenna aimed at modern wireless communication systems. It comprises a planar electric dipole with a vertically oriented shorted patch, operating above a square ground plane of 120x120 mm2, which is the center frequency wavelength of the antenna. The dipole length is 60 mm and is fed by a Γ-shaped strip. This system, like the previous, is designed to operate in free space as its application suggests. The frequency range of operation is 1.85 to 2.89 GHz. It offers a stable gain at 8 dBi, and the radiation patterns are symmetric in the E and H planes. Testing involved full-wave simulations using IE3D and experimental validation with an HP8510C network analyzer and compact range chamber measurements. Its interesting to note that this design reduced back radiation by 10dB compared to dipoles. While the design achieves its objective of unidirectional radiation and low cross-polarization, it is not been validated for focusing power inside tissues, and its size appears to be inconvenient for a system equipped with multiple antennas meant to rest around the human head.

[36] UWB Bowtie Antenna for Medical Microwave Imaging Applications

Fiser et all. designed a bowtie antenna for microwave imaging powered by a balun circuit. The main imaging fields intended for the device are brain stroke detection and brain stroke monitoring. The antenna is constructedon a ROGERS RO4003C substrate and the radiating element is a planar bowtie dipole with rounded edges, which have the purpose of reducing the antenna dimensions. Such dimensions are 60x60 mm2 while the substrate thickness is 1.54. The depth reaches however 50mm due to the perpendicularly mounted balun circuit to ensure symmetrical excitation. Performance metrics show operation across 1–6 GHz with a fractional bandwidth of 143%, while the reflection coefficient |S11| remains below -12 dB for brain and muscle phantoms. The balun features an exponentially tapered profile, which was deemed the most performing by experimentation. The antenna was in fact validated on in both numerical simulations (using a cube of material) and lab testing, where an octagonal phantom with a plastic shell was filled with a liquid material simulating the average electromagnetic properties of the brain and was surrounded by 8 antennas. The sensor array was then used to successfully locate specifically inserted inhomogeneities. The SAR distribution in the simulations point to an unidirectional radiation pattern. The wideband and ease of manufacturing seems very promising for the Wavision's task, but the perpendicularly mounted balun and the wide substrate are not in favour of a tightly packed array of antennas.

[37] Electronically Scanned Active Sensor Array for the Imaging of Compressed Breast

In this paper an active sensing array is presented constituted by 6x6 printed slotted antennas. This system has the aim of conducting breast microwave imaging to detect cancer. The antenna structure is realized on a multilayer printed circuit board, with slot antennas etched in Metal Layer 4 at 12 mm spacing, electromagnetically coupled to forks in Metal Layer 3, and transitioned via coplanar waveguides to triple-wire vertical vias. A grounded metal plane serves the purpose of isolating the radiating elements to improve the front to back ratio and achieving a unidirectional pattern. The numerical testing involved a cylindrical phantom with a range of height, with two arrays laid on the two flat sides of the model. This exact same setting was replicated in physical testing, were a carbon-rubber material was used to simulate the EM properties of compressed breast and Keysight VNA was used for measurements. The frequency range was found to be 3 to 8GHz, a very suitable range for breast imaging. Mutual coupling was also very low, below -20dB. The array is however too large to be used on the patient's head and is also not flexible. Scaling it down could prove to be very challenging due to the multilayered nature of its structure.

[38] A Portable Electromagnetic Head Imaging System Using Metamaterial Loaded Compact Directional 3D Antenna

Islam et all. present a portable electromagnetic head imaging system designed for non-invasive detection and monitoring of intracranial haemorrhages. The system is based on an antenna constituted by two slotted dipole elements. The dipoles include two folded parasitic components that are meant to enhance the directivity of the beam, and two separate arrays of metamaterial cells improve the bandwidth of the sensor. These cells are formed by three hexagonal slotted rings connected between them by a metallic segment. A microstrip line is used to feed the antenna and the overall structure is designed to exhibit a symmetry on the y axis. A Rogers RT5880 substrate is used for the antenna, which measure 30x70 mm2 in its footprint. A complex head phantom was used in both numerical and real-world testing, with multiple tissues represented by different materials. The frequency operating ranges of the two settings show negligible difference: the reflection coefficient stays under the -10dB band between 1.12 and 2.5 GHZ. Both simulations and experiments analysed the antenna operating at a distance from the head, and this was shown to be a difficult obstacle for the antenna in field penetration. The system was nonetheless able to detect and locate objects inserted inside of the phantom. The system's major weakness is its size, which is hard to implement in a device designed to be please in direct contact with the head of the patient.

2.3 Comparison of the modelled antennas

The antennas chosen to be modelled and simulated were the circular patch antenna with a parasitic element [23], the double substrate bowtie antenna [30], the double ridge filled horn waveguide antenna [26] and the edge feed planar log periodic antenna [18], shown in Figure 1. They were selected due to their good operating range, compact size and their design conceived for directivity. Since the presence of the feeding system on the edge of the log periodic antenna would be less practical for the Wavison brain stroke monitoring helmet, that requires 22 antennas to be stacked closely on the surface of the device, a fifth antenna was added to the simulation group. This device was obtained by removing the original feeding microstrip from the back of the substrate and placing instead a coaxial waveguide port on the same side that connects to the two structures on the front through two separate vias, as illustrated in Figure 2.

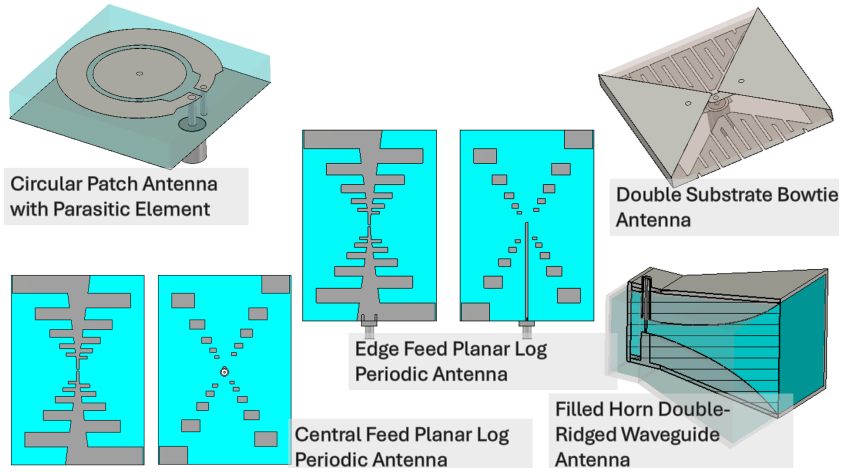

Figure 1: The modelled antennas

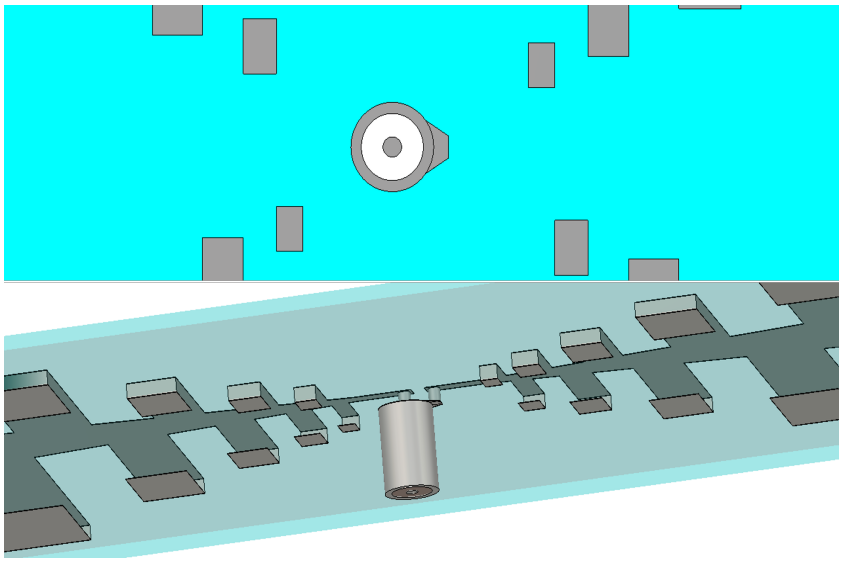

Figure 2: Details of the central Feed Log Periodic Antenna

The geometry of the horn antenna required the choice of an equation to describe the profile of the ridges.

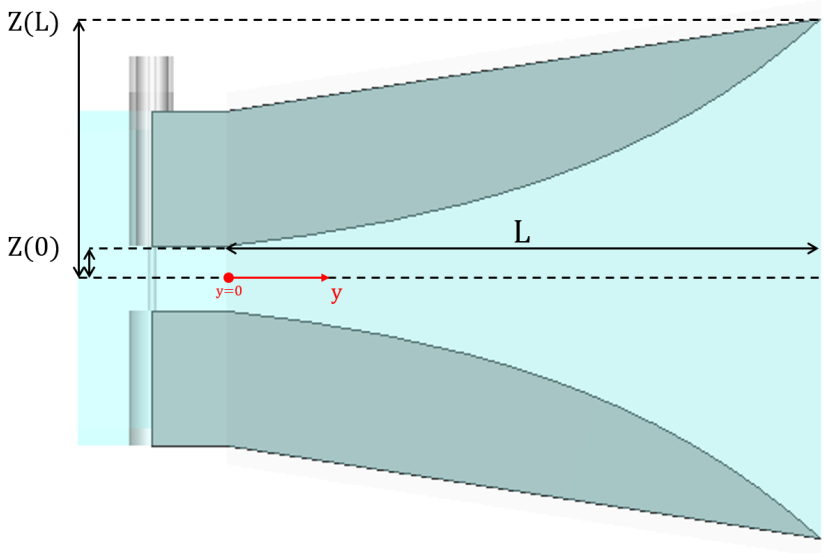

Figure 3: The used ridge profile reference system

Such equation was chosen to be $Z(y) = Z(0)\, e^{ky}$, where $k = \frac{1}{L} \ln\left(\frac{Z(L)}{Z(0)}\right)$. In this way the values of the parameters were strictly dictated by the intended geometry of the antenna, such as its height, length and space between the ridges at the core of the waveguide. A similar approach for antenna ridges was adopted in [39], where a linear part was also added to the exponential one.

Simulation Conditions

The radiation of the antennas had to be numerically simulated to calculate the frequency curve of their S11 parameter (reflection coefficient) and S12 parameter(transmission coefficient) over the relevant range of frequencies. Such interval stands between 0.5 and 2 GHz, but the most effective interval is between 0.8 and 1 GHz, which is the interval where not only the best best compromise between depth and resolution is achieved, but where the impact of inevitable manufacturing errors of the antennas can be minimized [10]. Furthermore the values of both EM field and power density field had to be calculated and displayed to observe the penetration of the EM waves inside the volume of the subject. The solver, CST Studio, was set to work in the frequency domain. The chosen matter to be irradiated therefore had to be comparable to the investigated subject, the brain. For this reason a material was employed that has the weighted average electromagnetic values of grey and white brain matter.The values of permittivity and conductivity used in this study, shown in Figure 4, are derived from experimental measurements of tissue-mimicking liquids used for lab testing, which themselves are formulated based on human tissues dielectric properties obtained from open-source databases from IT'IS Foundation [40].

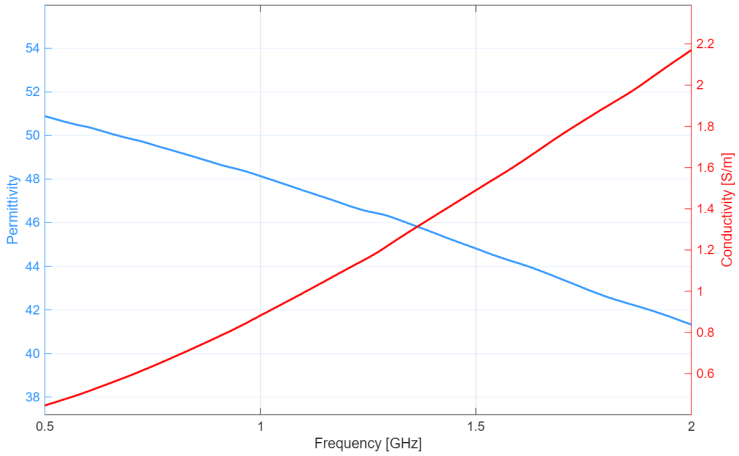

Figure 4: Average brain material permittivity and conductivity

A filling material had to selected to be able to simulate the horn antenna and compare it to the other sensors. A crucial parameter in this matter is the permittivity of the material which can ensure or prevent a matching between the impedance of the antenna and the impedance of the brain. For this reason a set of computational simulations was conducted in which the horn antenna, filled with materials of different permittivity (i.e. eps = 10, 20, 30, 35, 40, 50, 60), was placed directly in contact with a cube of average brain material. Such values were chosen to explore a range containing both the value of the filling used in the original paper and a few of the values commonly used in the laboratories of the Wavision group. The cube had dimensions of $200 \times 200 \times 150$ mm, and the filling material was set to be simulated without any loss. In this way the S11 is not influenced by the intrinsic power absorption of the material, only by the quality of the impedance matching. Furthermore, the permittivity was set to be stable across all frequencies. The results of such tests are reported in Figure 5.

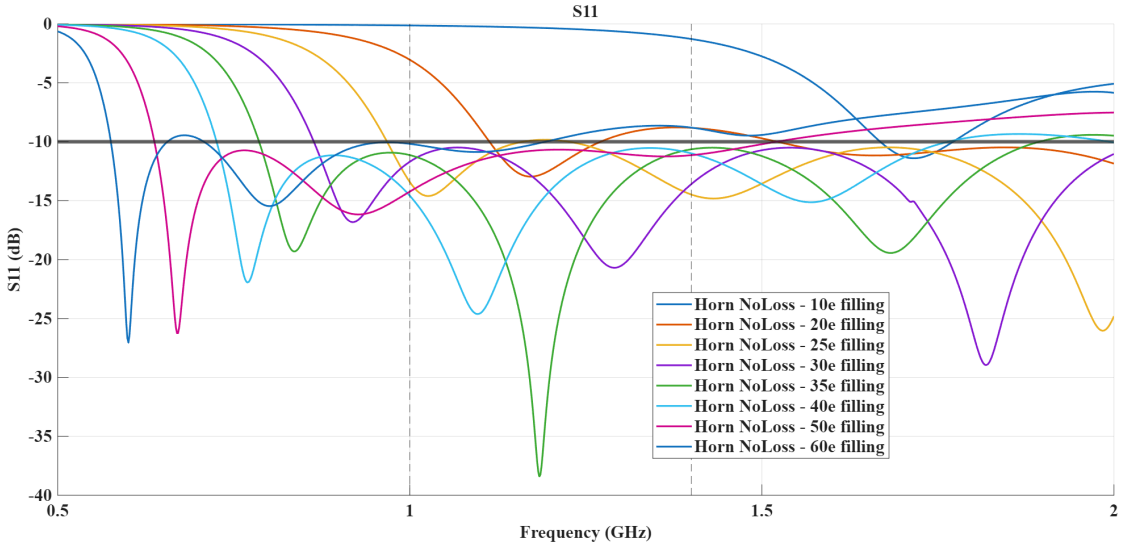

Figure 5: S11 of the horn antenna with different filling permittivities and no losses

These tests highlighted the promising behaviour of scattering parameters found with the fillings with permittivity of 30, 35 a 40. To make a more precise final choice between the three, a further simulation was run for each one of them including losses. The entity of the losses was decided based on the ones found in the filling mixture used in [26]. This was done by imposing the dielectric loss calculated using the conductivity and permittivity at 1 GHz of the author's mixture, its value being simply $\tan\delta = \frac{\sigma}{2\pi f \varepsilon_0 \varepsilon_r} = \frac{0.5}{2\pi \cdot 10^9 \cdot 4.8697 \cdot 10^{-10}} \approx 0.1634$.

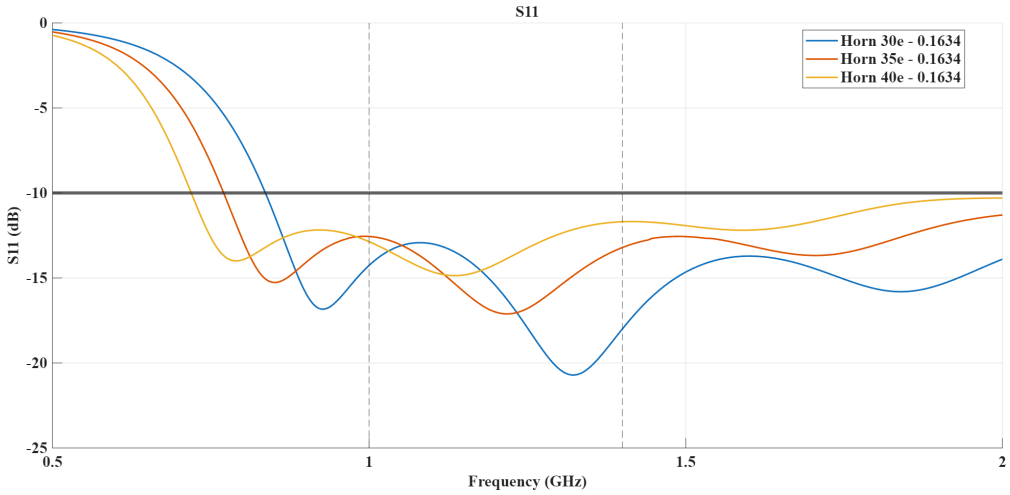

Figure 6: S11 of the horn antenna with different filling permittivities, losses included

Figure 6 reports the S11 curves obtained with the three new fillings.The value of $\epsilon = 30$ was found in this way to be the one with the least reflection in the relevant band of

0.8 to 1 GHz, thus making it the best candidate. This is caused by the shift in resonance frequency observed lowering the relative permittivity of the filling.

With all of the five antennas ready to be simulated the last choices regarded the target choice and frequency range. It was chosen to run simulations first with a single antenna placed directly on the previously cited block of average brain material without any gap, to test for S11 on the most simple situation possible, and then repeat the simulations with two opposing antennas at the ends of a plastic shell filled with the same average material to compute the transmission coefficient between them. The latter is the digital twin of a physical phantom realized inside the laboratory of the Wavison Research Group. This will allow for direct comparison between simulated and measured scattering parameters. The plastic material has a relative permittivity of 2.1.

Simulation Results

The first phase of single-antenna simulation on the average brain block led to a set of S11 curves for the most part well below the threshold of -10dB, as shown in Figure 7, which is generally chosen as the threshold for acceptable antenna performance. This indicates that in an idealized scenario of perfect adherence to the brain tissues all of the five antennas show negligible reflection at the antenna-subject interface. All of the antennas seem to have a bandwidth that goes from 0.5 to 2 GHz and beyond, except the circular antenna and the horn antenna, whose minimum usable band frequencies are 0.57 and 0.83 GHz respectively. This scenario is reported in Figure 7.

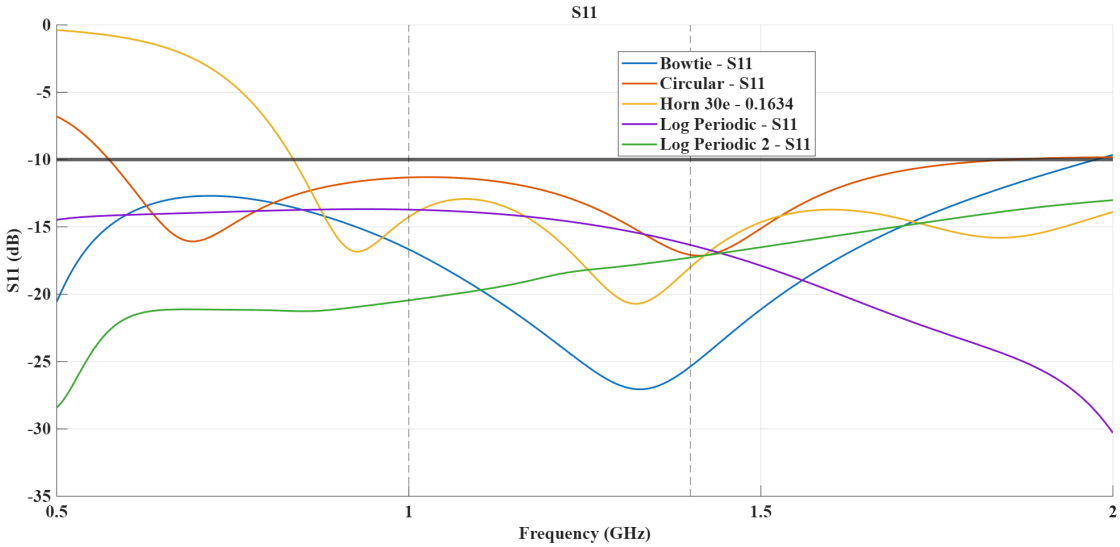

Figure 7: S11 of the single antennas placed directly on the average brain cube

After the computation of the S11 curves, it was necessary to investigate the electric and power density fields. Since the three non-log periodic antennas showed to have a resonant frequency around 1.4 GHz, both 1 Ghz and 1.4 GHz were selected as the frequencies at which the electric field was calculated and displayed.

After such computations, a convention had to be established to properly compare the fields of the five antennas. They were visualized on the two main cross-sectional planes intersecting both the antenna and the object. Since the wave-front plays a crucial role in the understanding of the propagation of the EM waves inside the subject, on the surface and in the back direction, instantaneous E field is employed instead of average E field, which would cancel out the exact shape of the waves. To combine this approach with a more rigorous representation, power density distributions are then showed for each antenna and both planes of view. Given the periodic dependence of the E field on the phase of excitation, a specific phase has to be selected for the diagrams. To give these a more representative quality in the context of a study on wave dispersion, an approach was employed for each antenna where the phases of most back radiation and least back radiation were taken as values for an average phase. This average phase gives us a field qualitatively comparable to the average E field, where the wavefronts are preserved and the back radiation displayed is the one that best characterizes the general performance of the antenna.

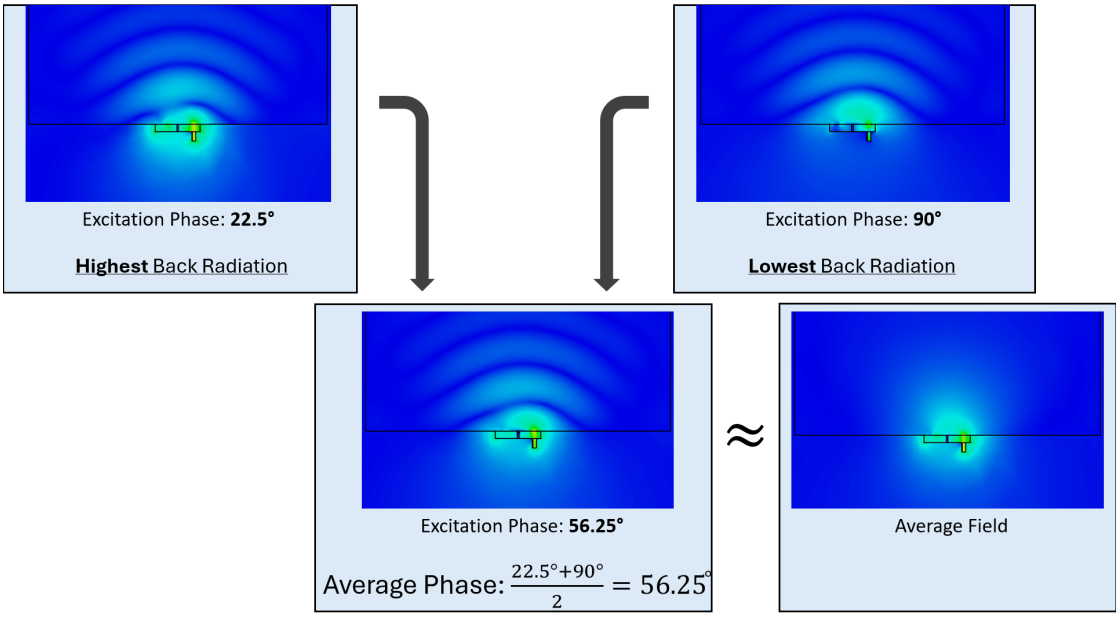

Figure 8: The average phase approach

Figure 9 to 12 report the electric fields of the five antennas at 1 and 1.4 GHz, in the frontal and lateral plane, while radiating on the average brain material cube. Figures 13 to 16 report the corresponding power density distributions.report the electric and power density fields of the five antennas at 1 and 1.4 GHz while radiating on the average brain material cube.

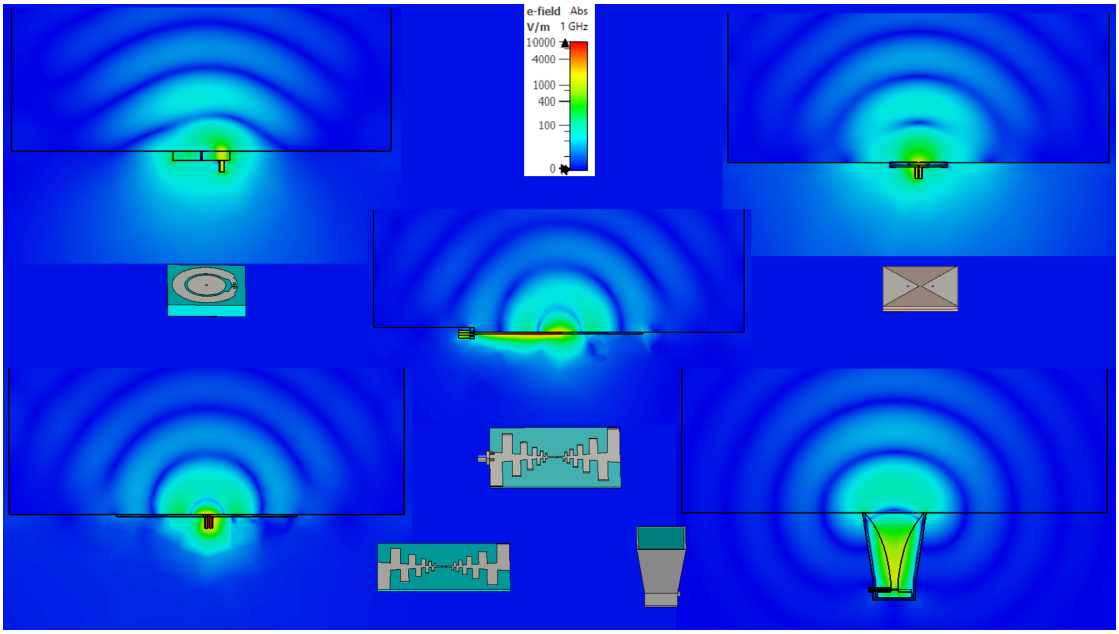

Figure 9: E field of the antennas on the frontal plane at 1 GHz

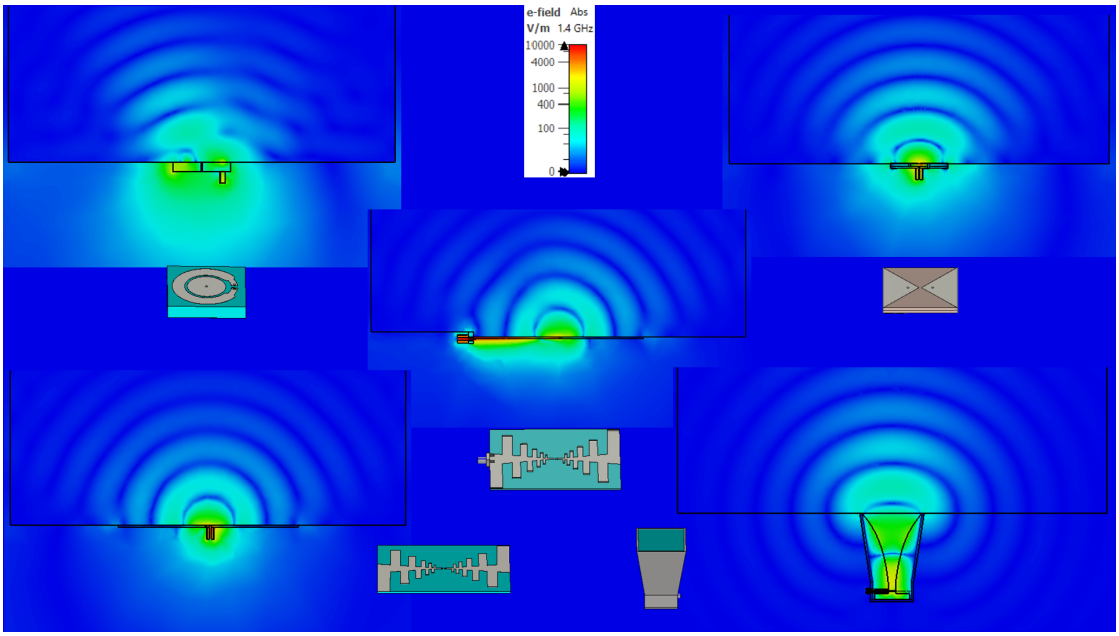

Figure 10: E field of the antennas on the frontal plane at 1.4 GHz

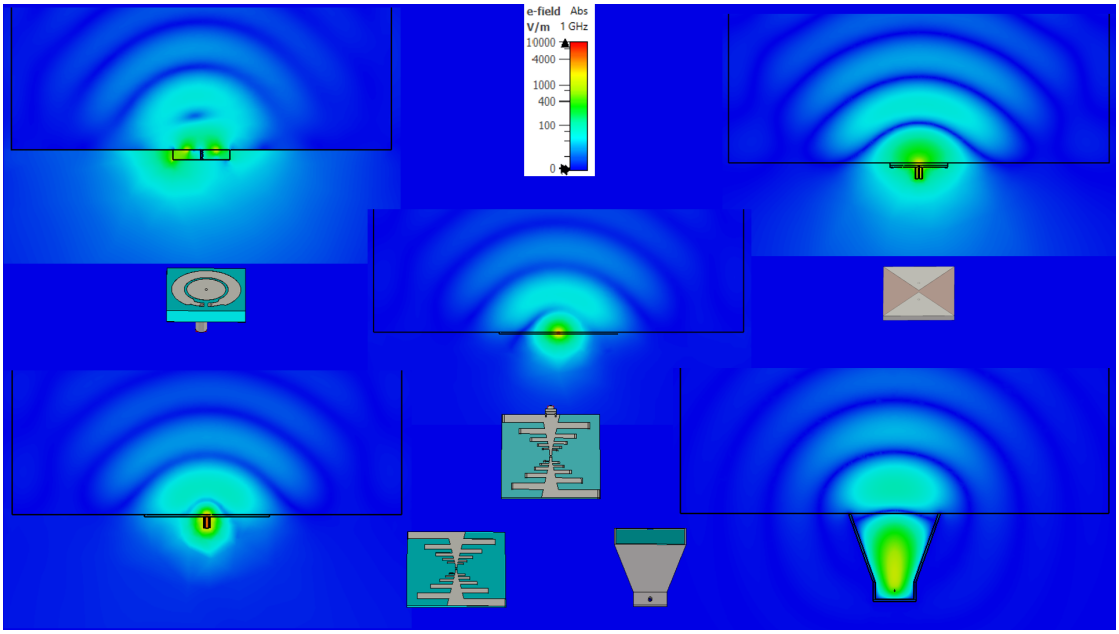

Figure 11: E field of the antennas on the lateral plane at 1 GHz

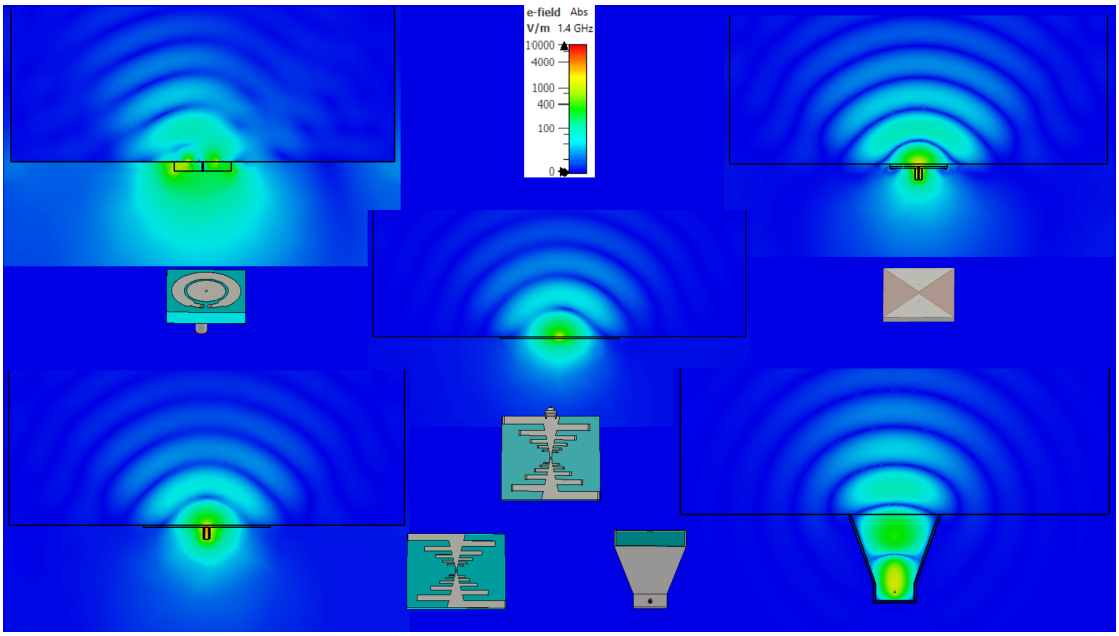

Figure 12: E field of the antennas on the lateral plane at 1.4 GHz

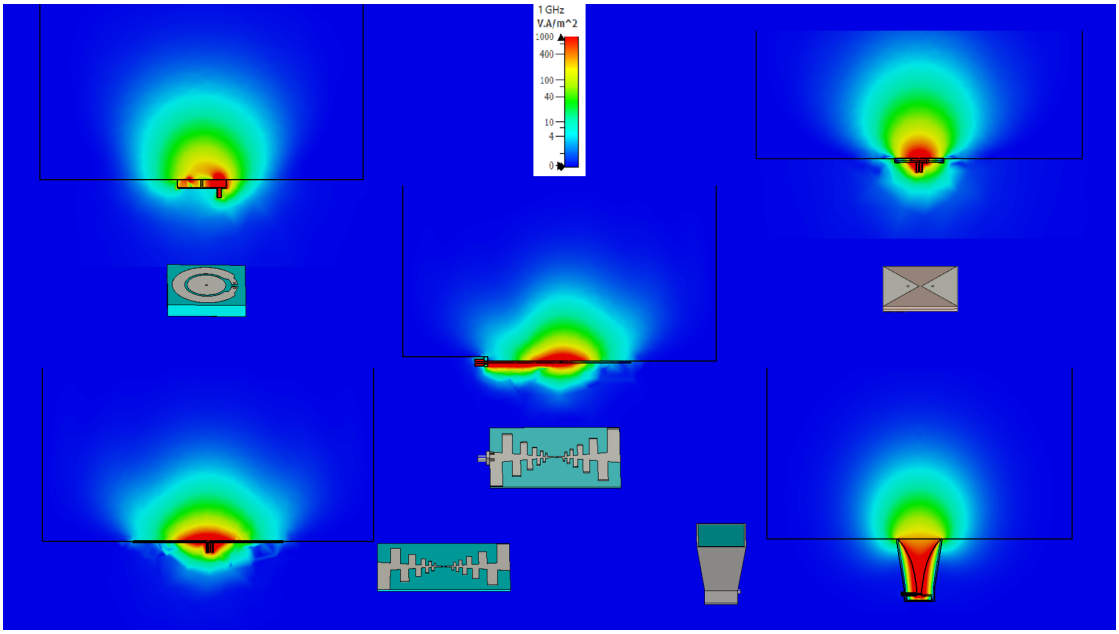

Figure 13: Power density field of the antennas on the frontal plane at 1 GHz

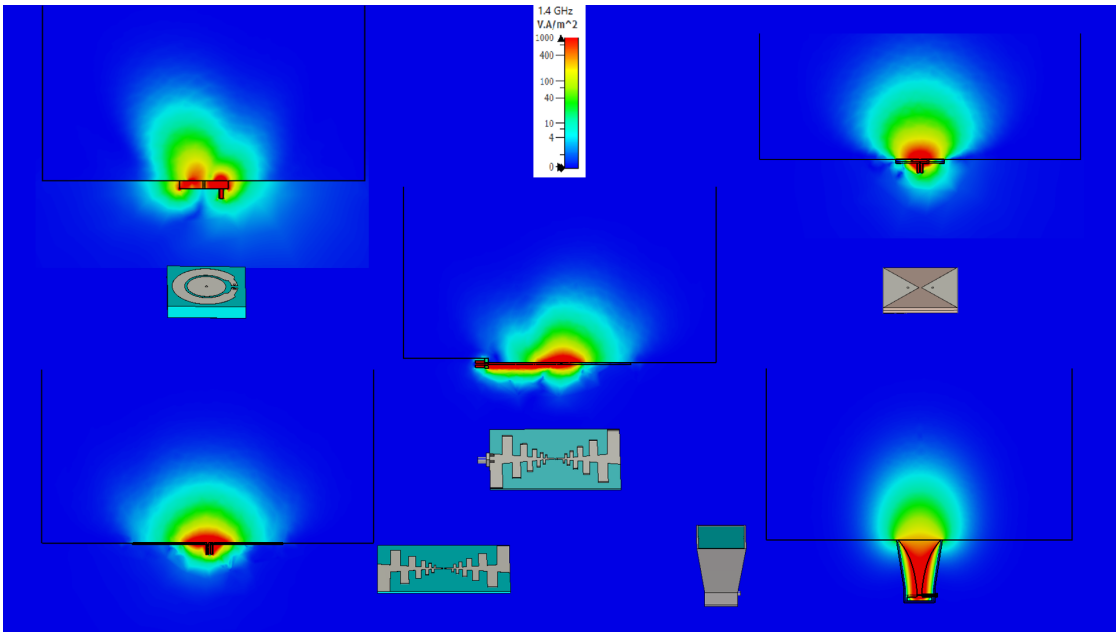

Figure 14: Power density field of the antennas on the frontal plane at 1.4 GHz

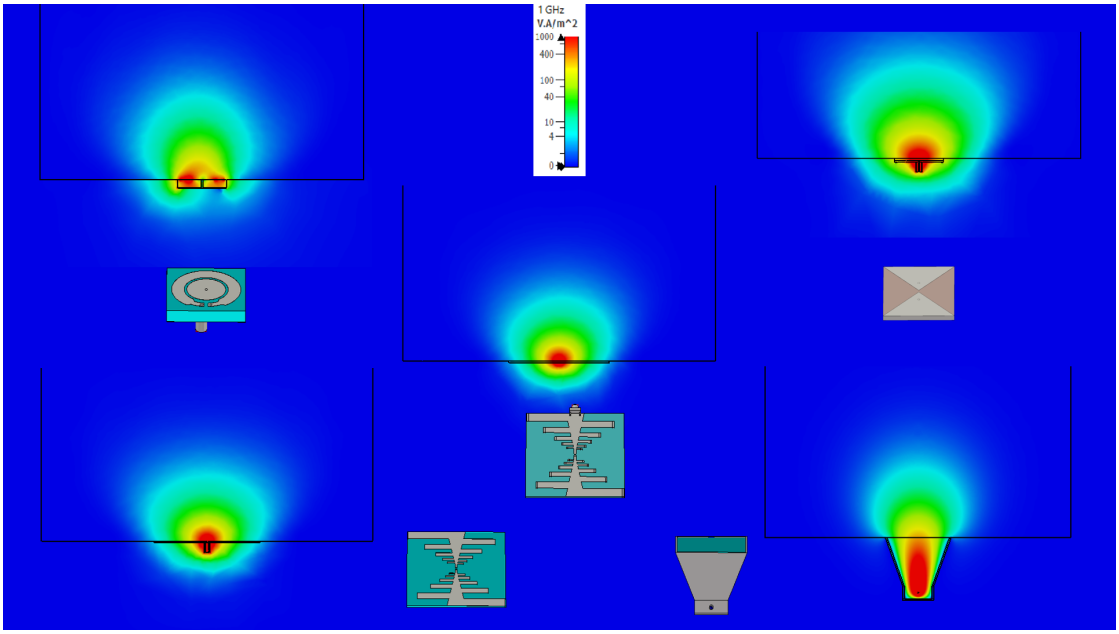

Figure 15: Power density field of the antennas on the lateral plane at 1 GHz

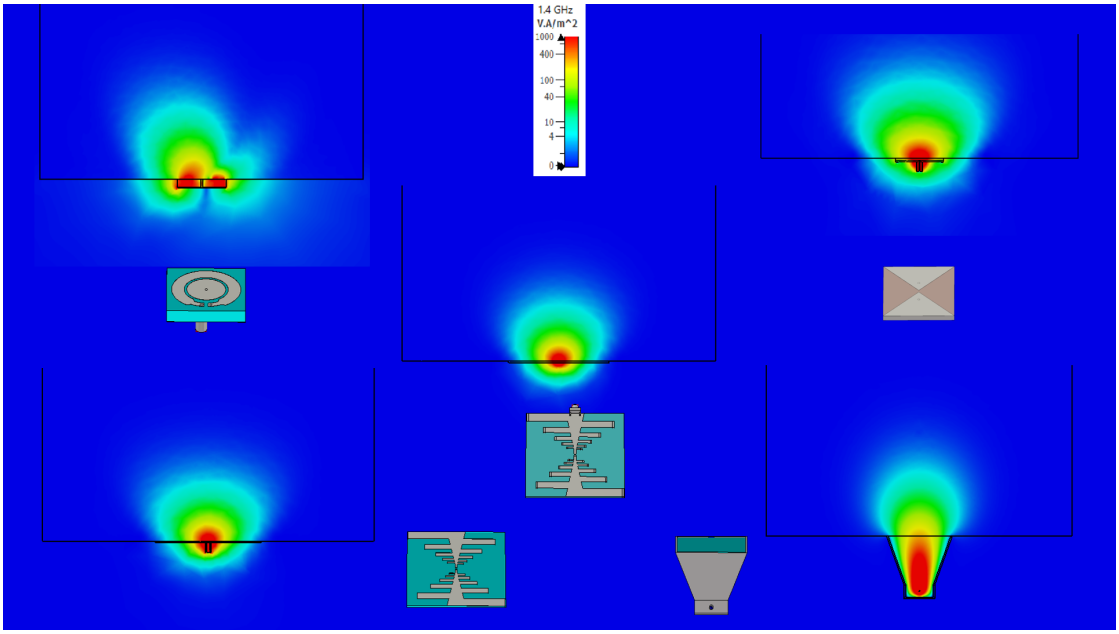

Figure 16: Power density field of the antennas on the lateral plane at 1.4 GHz

The difference between 1 GHz and 1.4 GHz in terms of field plots seems to be negligible. It is however interesting to note that the radiation pattern of the circular antenna seems to get more irregular at 1.4 GHz. Both the power density and electric fields suggest a

better performance from the horn waveguide antenna in terms of superficial waves and back radiation.

In order to gain a deeper understanding of the role of the different areas of each antenna, it was chosen to perform a simulation of the surface electrical average current densities at different frequencies. The resulting diagrams (Figures 17 to 20) highlight the most active parts of the geometries in terms of $\frac{A}{m}$, allowing a finer view of the way energy is conveyed through the structure.

To investigate a range of frequencies that could contain the most relevant band but also allow a higher degree of visible differences, the current density was calculated at 0.8, 1.4 and 2.0 GHz. This also favors an ease of visualization.

From this investigation has of course been excluded the horn antenna, as the working mechanism of this antenna is mainly based not on the superficial currents, but on the guiding effect that the three-dimensional walls have on the diffusion of the electromagnetic waves in the volume inside of the aperture.

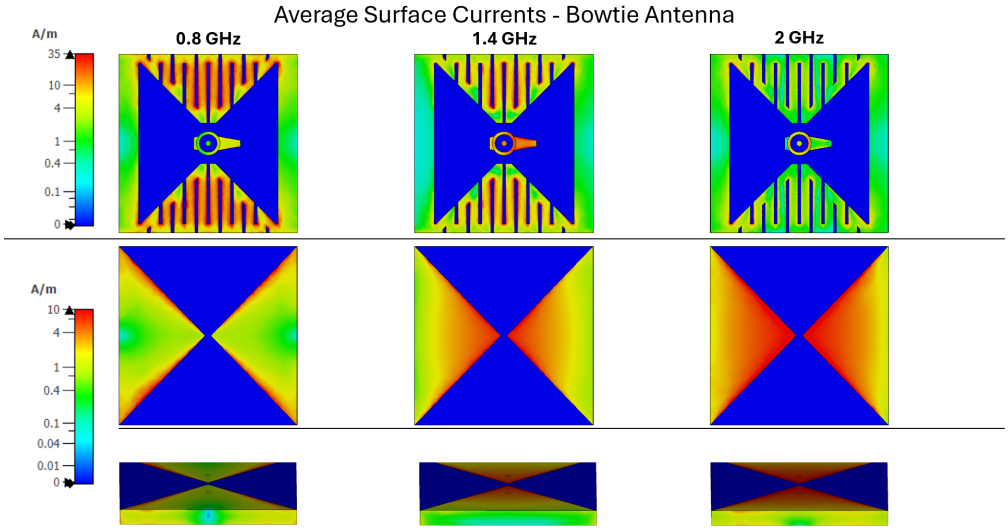

Figure 17: Surface current density on the Bowtie antenna

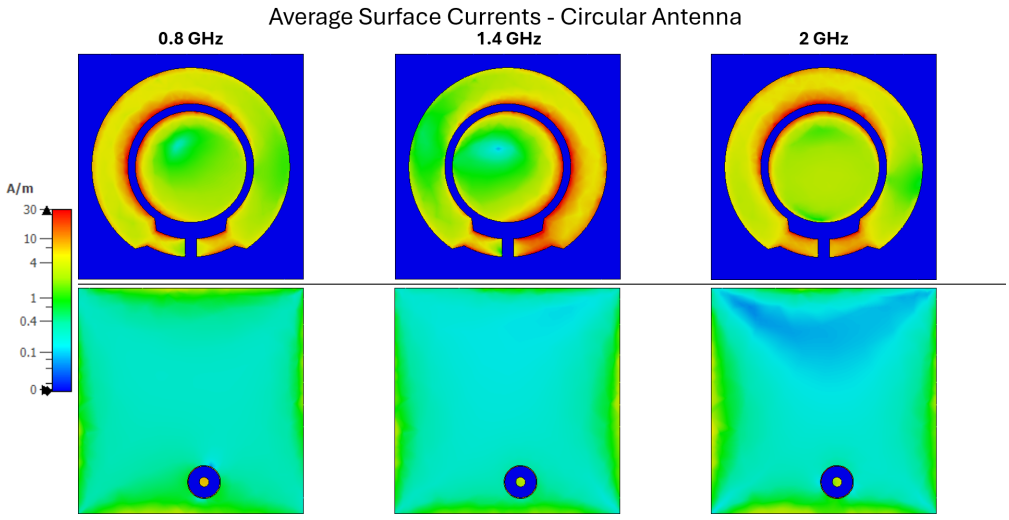

Figure 18: Surface current density on the Circular antenna

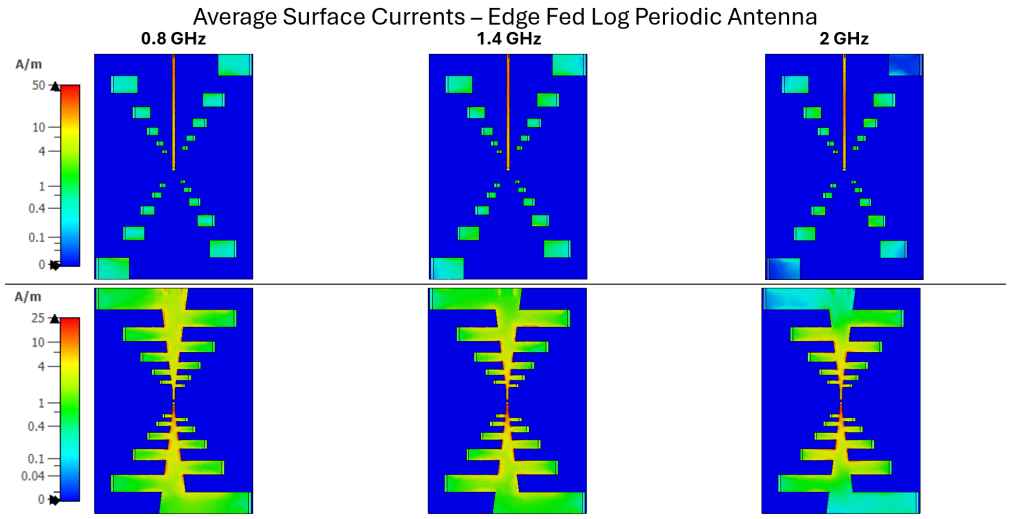

Figure 19: Surface current density on the Edge Feed Log Periodic antenna

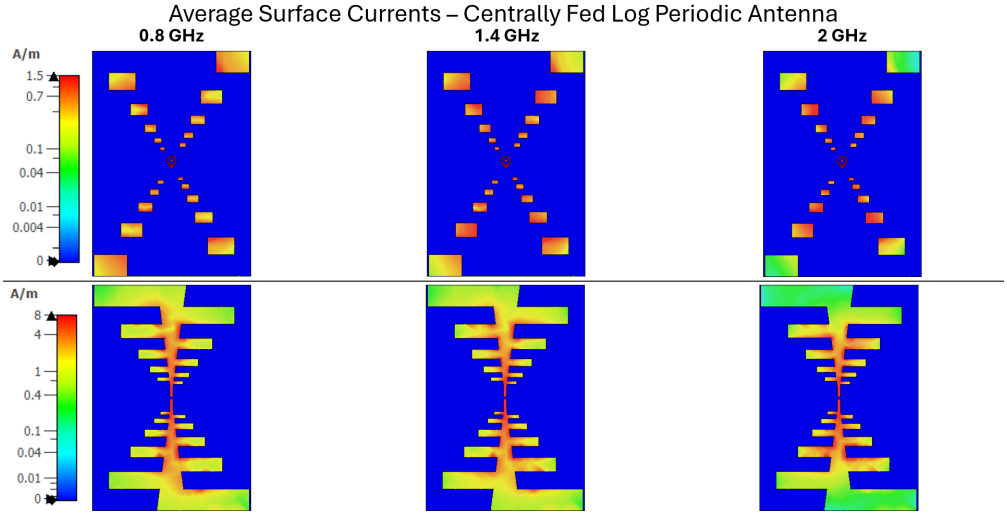

Figure 20: Surface current density on the Central Feed Log Periodic antenna

Such diagrams allow us to reach two important conclusions about the log periodic antennas. The first one is that the feeding microstrip in the edge feed antenna seems to be overly active in respect to the rest of the geometry, a feature that seems to be avoided with the use of a central feed system. The second one is that in both log periodic antennas the largest element of the antenna seems to be the least active. This prompts the interest in experimenting with the shape of the antenna, possibly trying to reduce its area, achieving a more compact sensor. Furthermore, an hypothesis had to be tested regarding the role of the curls on the backside of the antenna in redirecting the radiation in the front direction, possibly by simulating variant of the antenna with longer curls.

Six different combinations of this features were tested on the average brain block. The antenna lengths were the standard length of the antenna and the shorter length of the antenna, cut at the fourth periodic couple of elements. The three curl lengths were the standard length, 1.5 times the standard length and 2 times the standard length.

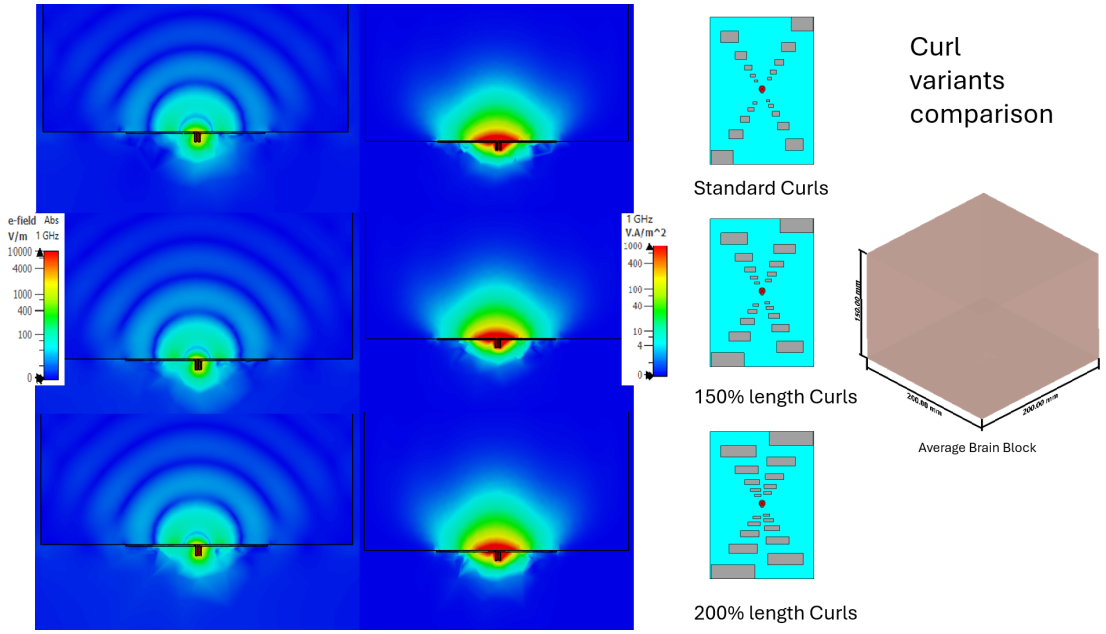

Figure 21: Electric and power density fields on the frontal plane of the log periodic antenna with different curl lengths

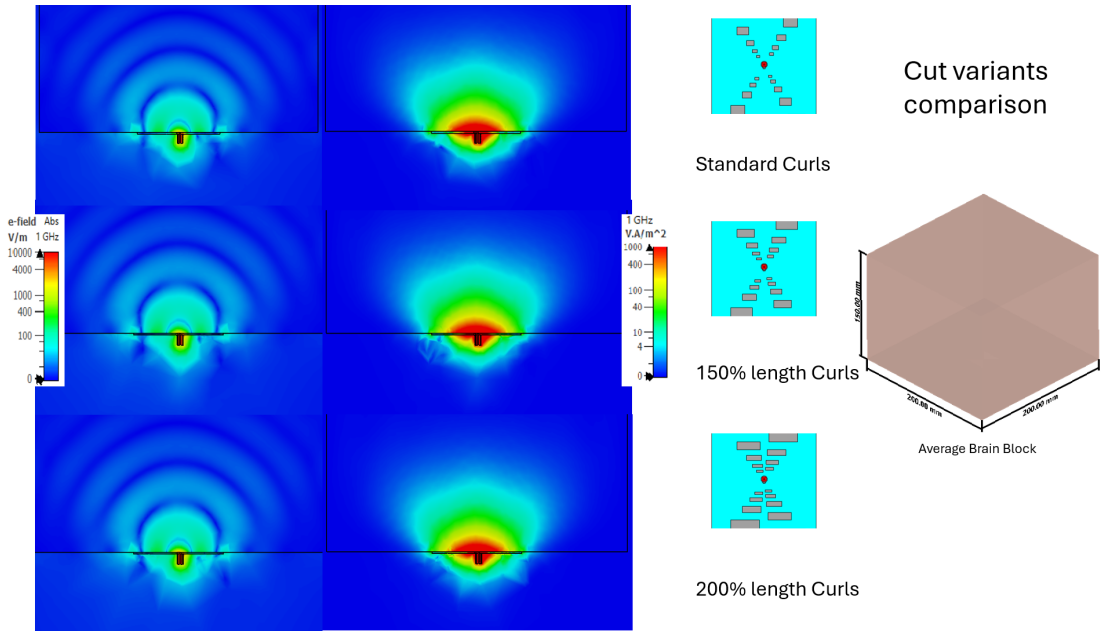

Figure 22: Electric and power density fields on the frontal plane of the shortened log periodic antenna with different curl lengths

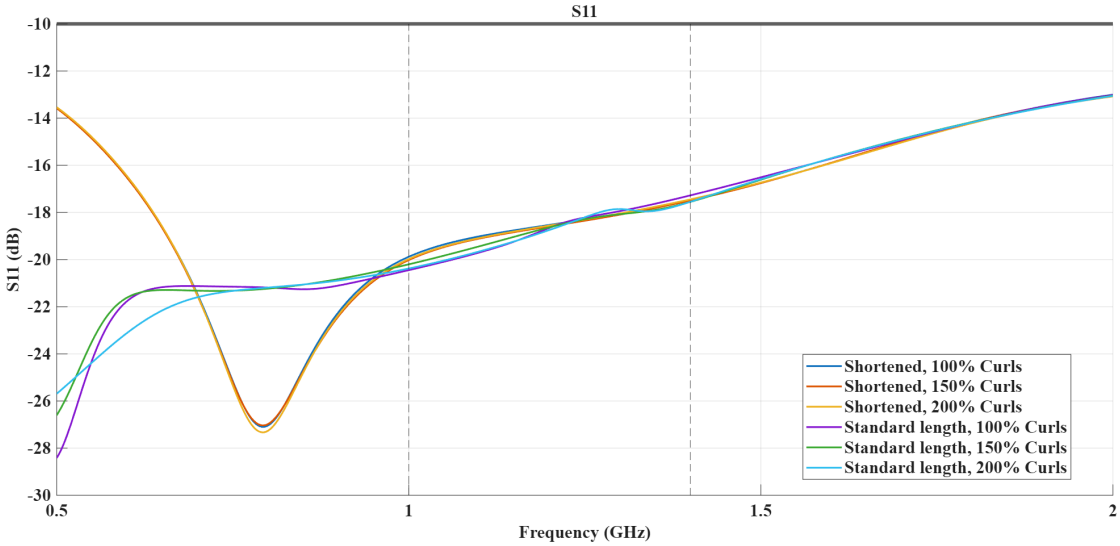

Figure 23: S11 of the different versions of the log periodic antennas

At 1.0 GHz the difference in the shape of the two plotted fields is negligible. However, the S11 curves resulting from this set of experiments led to to the conclusion that while the length of the curls does not particularly alter the band, the shortened version of the antenna presents a resonant frequency at 0.79 GHz.

After the first evaluation on a simplified shape it was clear that the central feed on the log periodic represented a substantial improvement in terms of both reflection and back radiation, due to the disturbance caused by the feeding microstrip, which appears to emit a considerable field. This led to the exclusion of the original design from further analysis, continued instead with the other four antennas.

A more complex testing setup had to be adopted in order to achieve the simulation of the transmission coefficient frequency curve, to evaluate the impact of a gap between the antennas and the brain, and to run computations on a model that has a physical twin in the real world. To this end a 1 mm Teflon shell was modelled to emulated the 3d-printed one used for the testing of antennas in the Wavison laboratory. The shell contains a $116 \times 96 \times 106$ mm core of average brain material. The outer shell is equipped with mounting features for the antennas both on opposing flat ends of the phantom and on one of the rounded side. This design leaves the possibility open for testing of non-aligned antennas. An expanded version of the phantom measuring $150 \times 96 \times 151$ mm in its core was also modelled, to make it suitable for the larger antennas (the two log periodic antennas). In this way edge effects are avoided.

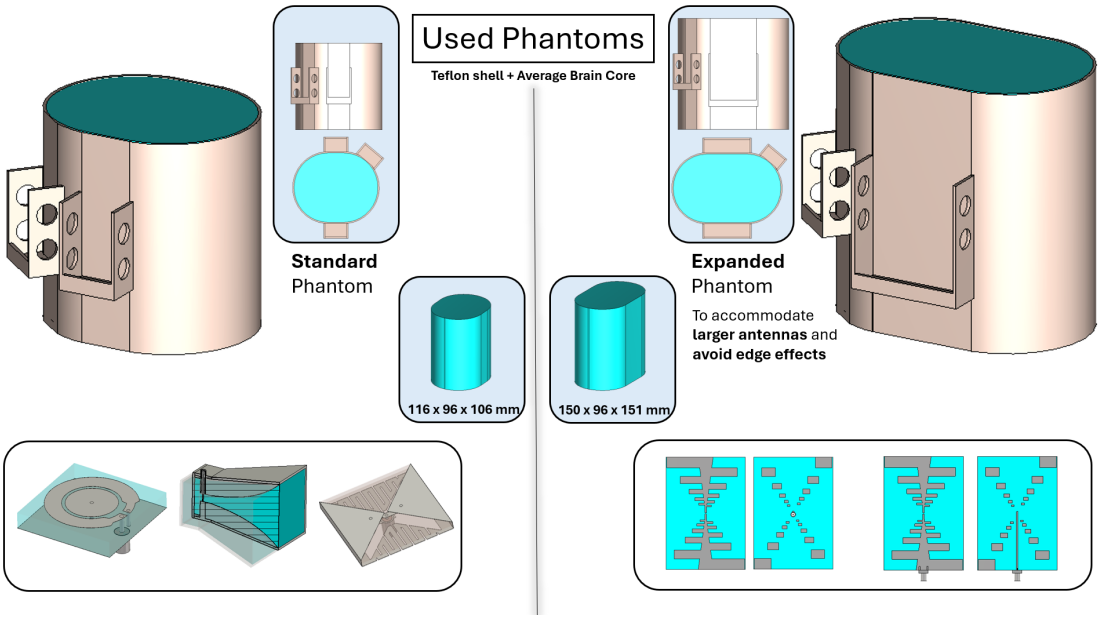

Figure 24: The two used brain phantoms

The use of this new subject has led to a new series of results, all obtained placing two antennas directly on the phantom in the place delimited by antenna holders, one in front of the other. Figure 25 and Figure 26 show us the reflection coefficient and the transmission coefficient respectively. To further investigate the possibility of a more compact Log Periodic Antenna, a variant was included in these simulations. This variant (Figure 24) displays the same longitudinal shortening tested earlier on the average brain cube paired with a lateral shortening that removes the empty part of substrate, turning its footprint from 91×64 mm^2 to 59.5×41 mm^2. The length of the back side curls in this version is the standard length, as it doesn't seems to be a particularly relevant parameter.

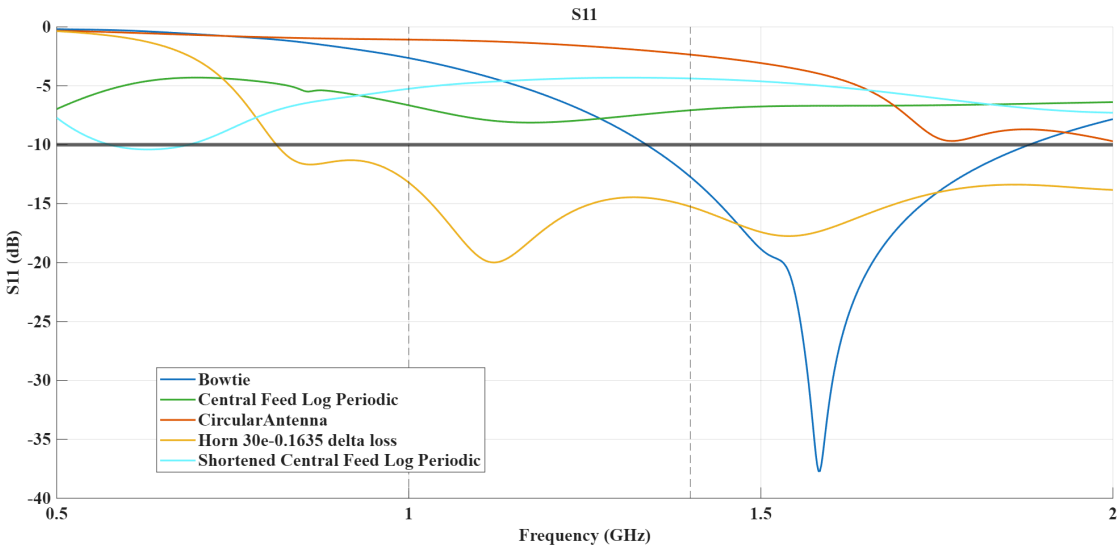

Figure 25: S11 of the antenna pair placed directly on the phantom

The reflection coefficient curves show that the plastic gap significantly increases the values, taking almost all of the antennas in the 0.8 to 1 GHz range out of the acceptable performance zone, except for the horn antenna. This antenna appears to be the least affected by the introduction of a gap. On the contrary, the reflection curves of the circular antenna and of the the log periodic antenna saw an extensive alteration in both their morphology and their modulus. The disruptive influence of a gap between the antenna and the head tissues has already been reported by Cuccaro et al. [41].

Antenna	**S11 (dB)**
Circular	-1
Bowtie	-3
Shortened Central Feed Log Periodic	-5
Central Feed Log Periodic	-7
Horn 30e-0.1635 delta loss	-13

Table 2: S11 values for each antenna at 1GHz

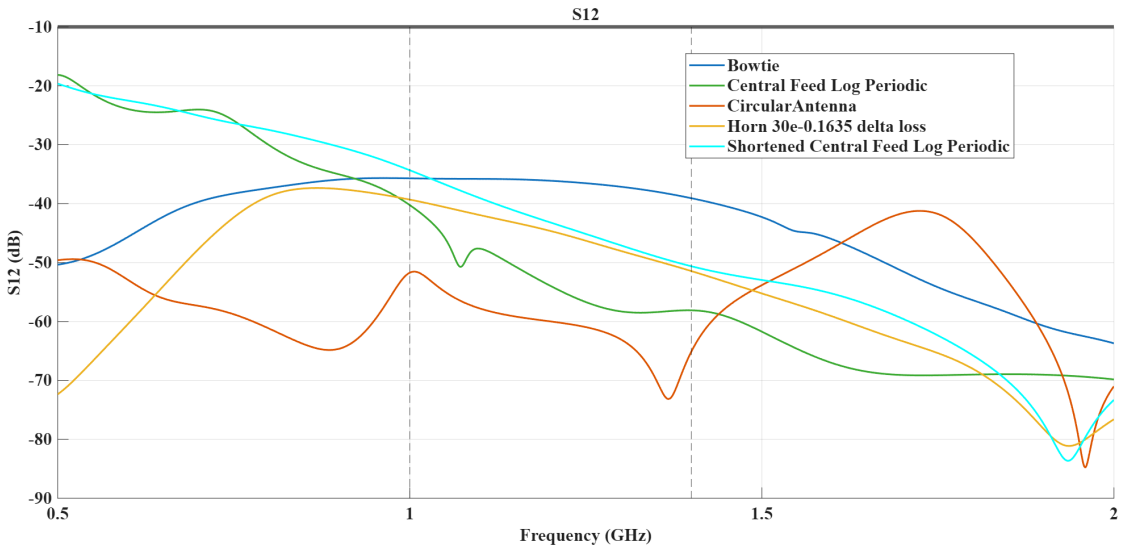

Figure 26: S12 of the antenna pair placed directly on the phantom

The value of the transmission coefficient of the antennas in the range of interest is comparable to the simulated value found in the brick antenna [42] of the Wavison stroke monitoring helmet.

Antenna	**S11 (dB)**
Bowtie	-36
Horn 30e-0.1635 delta loss	-40
Shortened Central Feed Log Periodic	-34
Central Feed Log Periodic	-39
Circular	-52
Brick	-45

Table 3: S11 values for each antenna at 1GHz

The electric and power density fields were calculated at 1 GHz, as the general tendency of a resonant frequency around 1.4 GHz can no longer be seen after the adoption of the new digital phantom. With a single frequency to focus on, fields are here reported antenna by antenna from Figure 27 to 31.

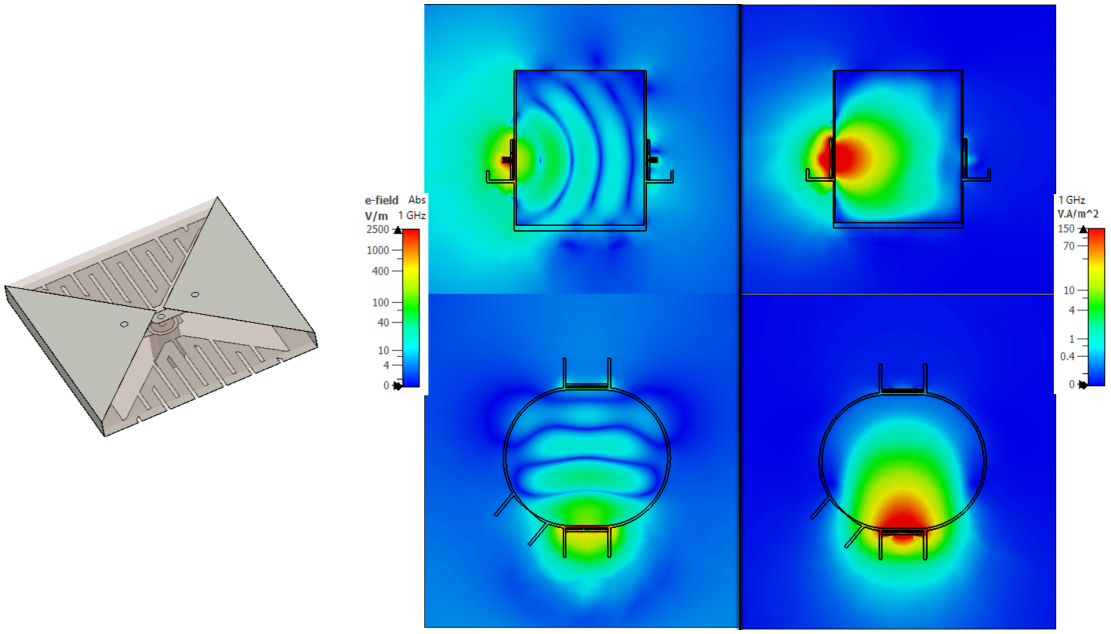

Figure 27: Electric and power density fields of the bowtie antenna at 1 GHz on the phantom

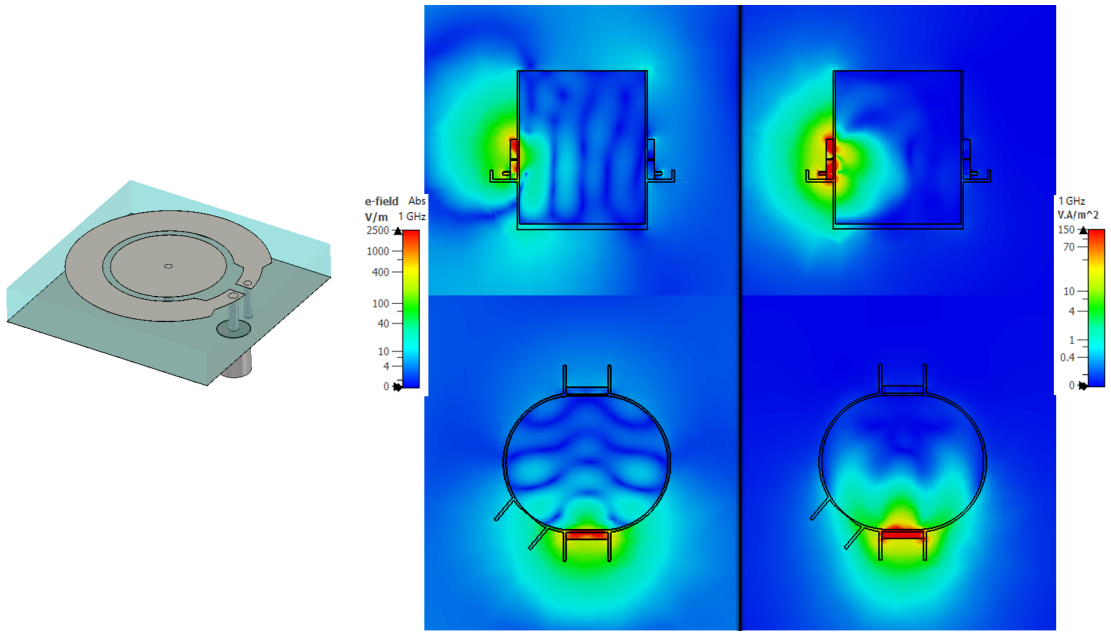

Figure 28: Electric and power density fields of the circular antenna at 1 GHz on the phantom

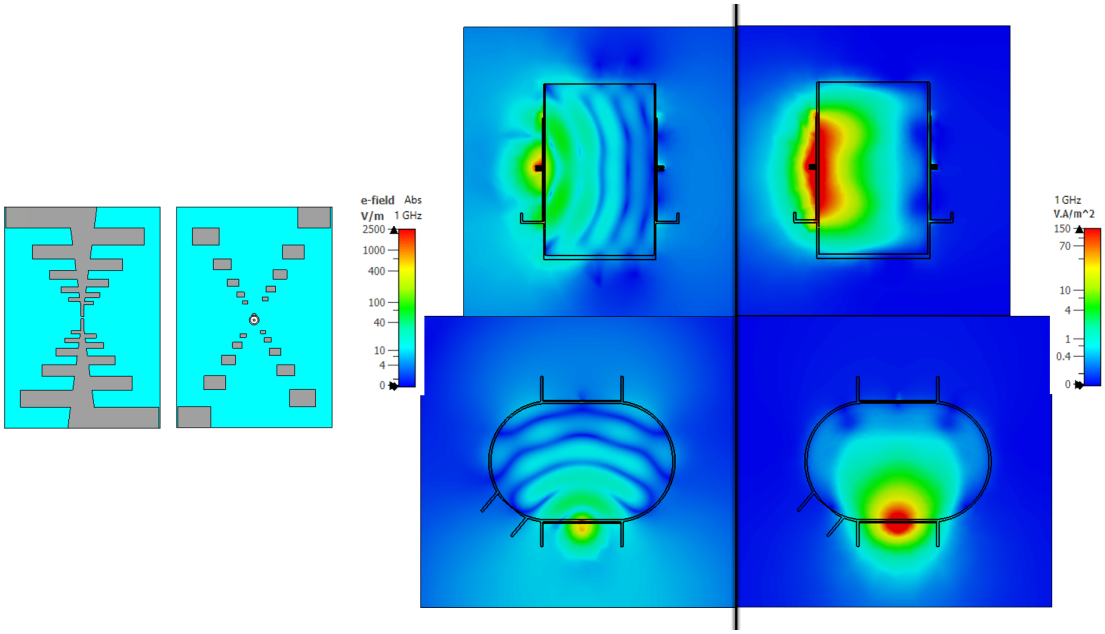

Figure 29: Electric and power density fields of the log periodic antenna at 1 GHz on the phantom

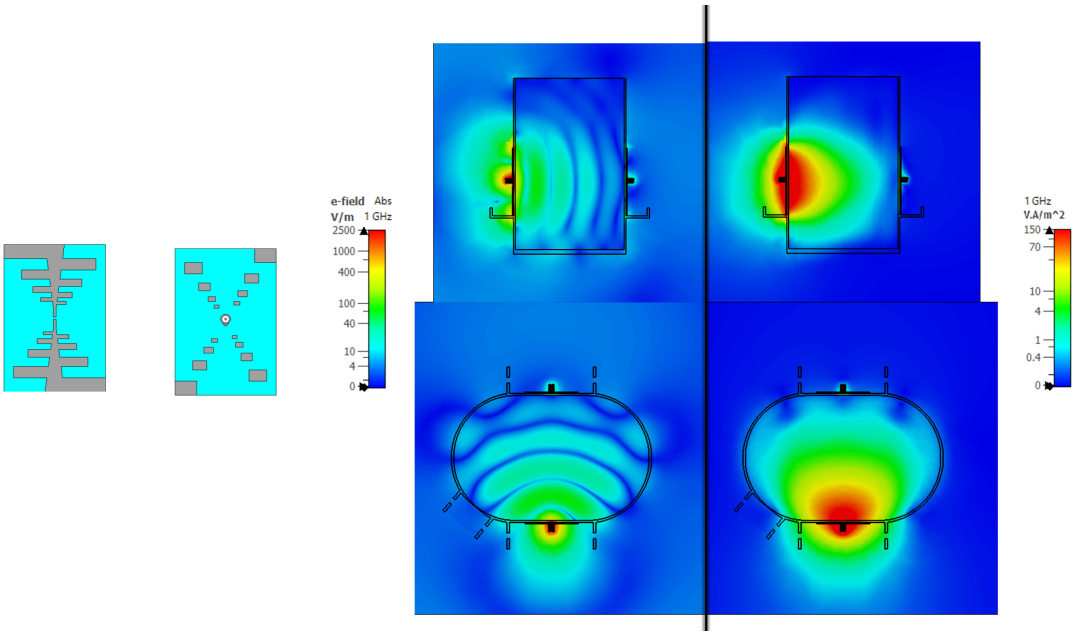

Figure 30: Electric and power density fields of the shortened log periodic antenna at 1 GHz on the phantom

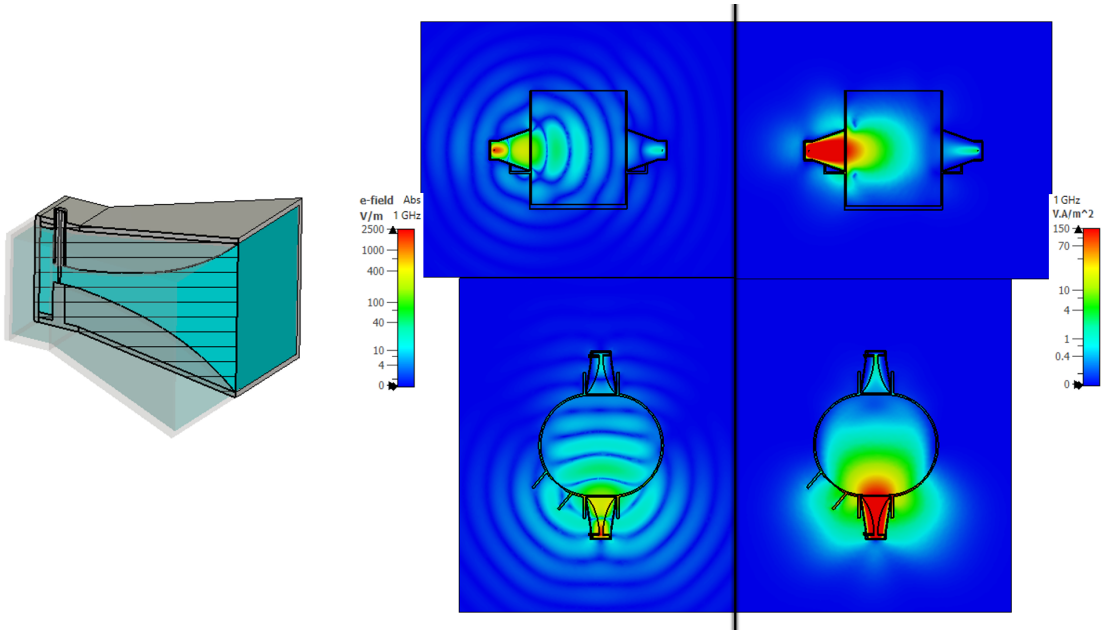

Figure 31: Electric and power density fields of the horn antenna at 1 GHz on the phantom

Once again the horn waveguide antenna shows a better coupling with the subject in respect to the other simulated antennas. It is however evident that with this phantom the surface electromagnetic waves seem to be more intense. This is probably the effect of the gap created by the plastic shell, that, due to its electromagnetic properties similar to air, constitutes an additional source of reflection.

Given the low front-to-back ratio of radiation displayed by the circular and log periodic antennas, it was deemed a valuable test to simulate the operation of these sensors in a situation where they are completely surrounded by the average brain material. Such a modality of analysis could verify if the radiation of these antennas achieves a significative focusing in a situation where the only focusing aid is the geometry of the antenna, and not the absence of matching material on the side and back directions. Figure 32 and Figure 33 show the electrical and power density fields in the described scenarios for the circular and log periodic antenna respectively. Figure 34 displays the field of the horn waveguide antenna in the same scenario: this serves as a useful comparison.

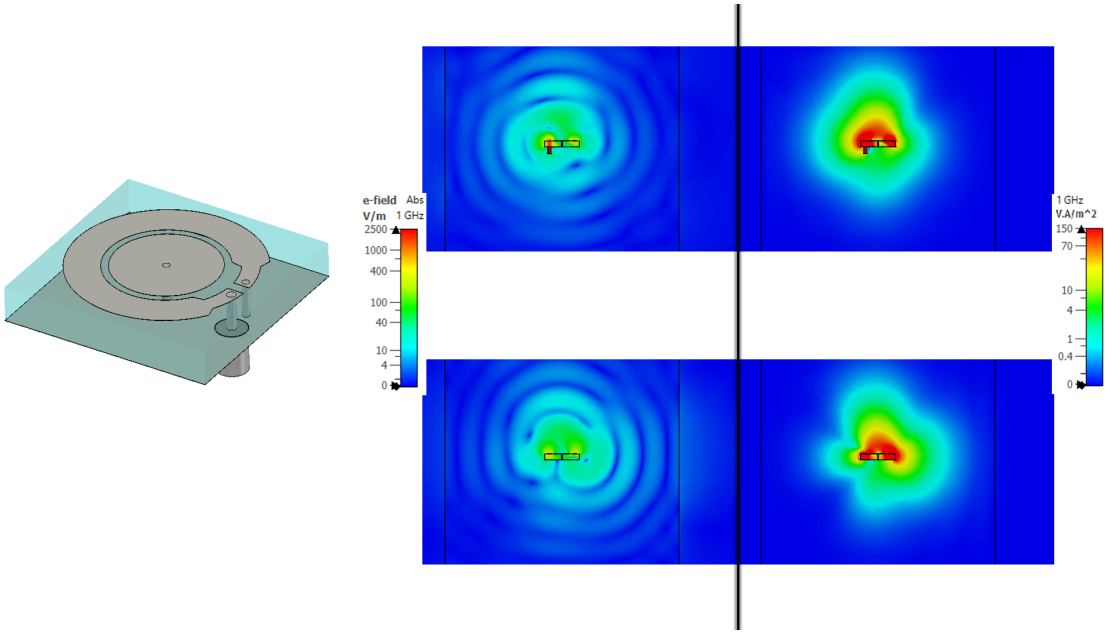

Figure 32: Electric and power density fields of the circular antenna at 1 GHz immersed in the average brain material

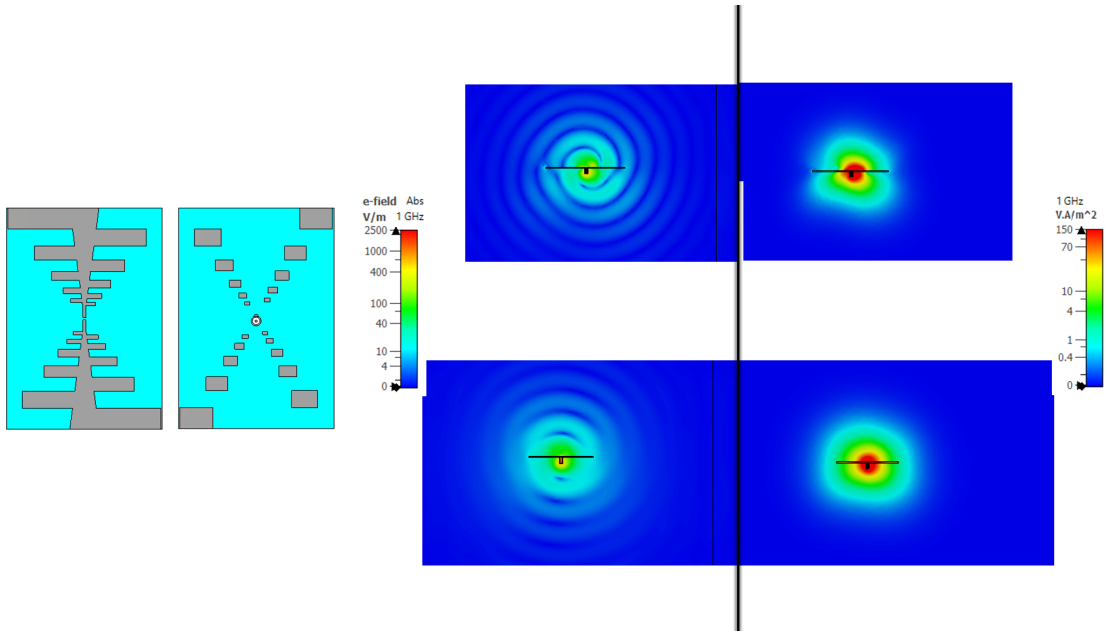

Figure 33: Electric and power density fields of the log periodic antenna at 1 GHz immersed in the average brain material

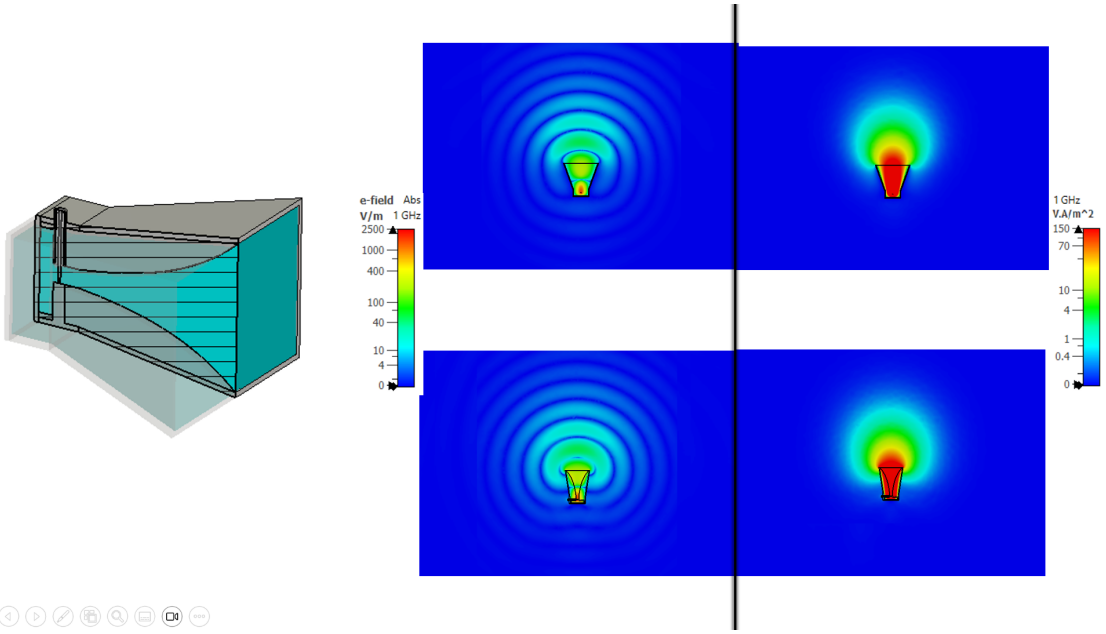

Figure 34: Electric and power density fields of the horn antenna at 1 GHz immersed in the average brain material

These tests make immediately evident the superior focusing mechanism of the horn waveguide antenna. In contrast, the circular antenna and the log periodic antenna fail to contain their radiation by means of sheer geometry, resulting in an omnidirectional pattern when challenged by full immersion in the matching medium.

To test whether the differences in the S11 graphs are truly caused by the gap created by the plastic shell, a simulation was carried out to recreate this effect on the circular antenna, the sensor whose reflection coefficient was worsened the most by the second phantom. This was achieved by using the previous average brain cube as subject, but instead of placing the antenna directly on the cube's surface a distance was introduced. The distance of such gap was varied parametrically, ultimately finding an optimal distance of 0.65 mm that yields an S11 curve morphologically matching the S11 curve that we get from the plastic shell. Only a slight frequency shift is observed between the two plots. It is interesting to note that with a gap of 1 mm, the thickness of the plastic shell, the result is not as similar.

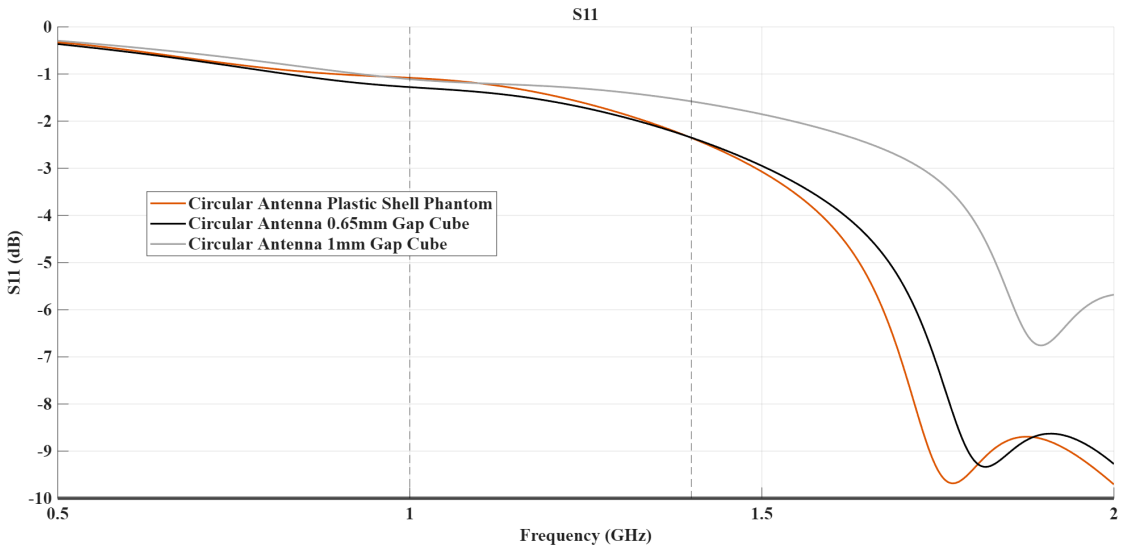

Figure 35: S11 curves of the circular antenna on the phantom and on the block with the introduction of a gap

As previously mentioned, the horn antenna is the one that was affected the least by the introduction of the plastic shell phantom. Comparing the two S11 curves of the cube and the plastic shell phantom it is possible to notice that they are already similar enough: the overall effect of the gap seems to be mainly a phase shift. Moreover, performing the same experimentation used on the circular antenna seems to not be useful to the aim of recreating the S11 curve obtained with the plastic shell phantom. The closest matches are reached with 0.15 mm and 6 mm distance gaps. To better validate the effect of the plastic shell on the performance of the antennas three new phantom variants were modelled. The circular antenna was then simulated again on these four different phantoms. Two had plastic shells: the standard phantom and a version identical to it except that the antenna support structures were removed. The remaining two phantoms were identical to those configurations, respectively, but with the plastic material replaced by the same average brain-equivalent material as the core.

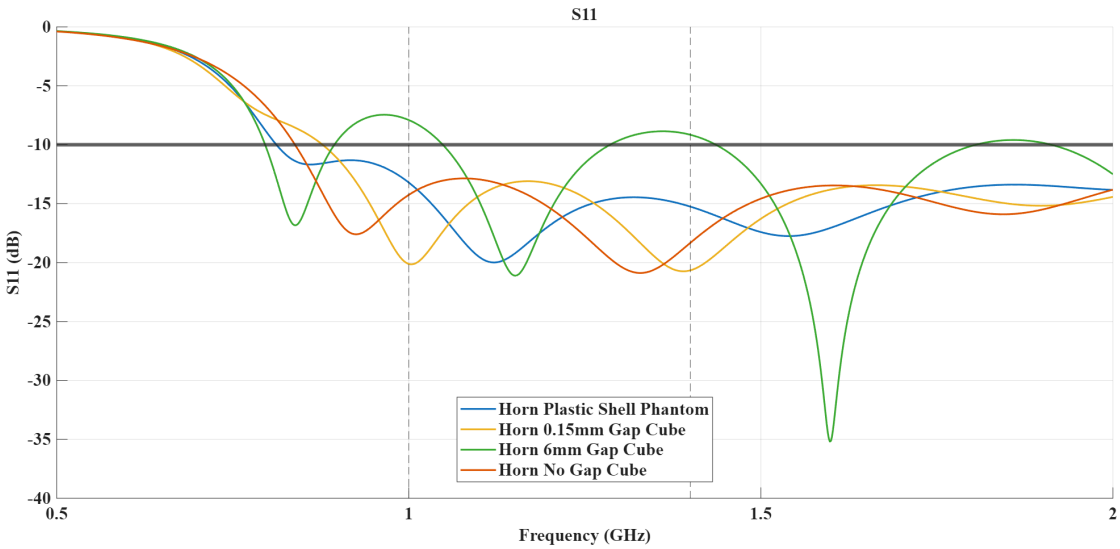

Figure 36: S11 curves of the horn antenna on the phantom and on the block with the introduction of a gap

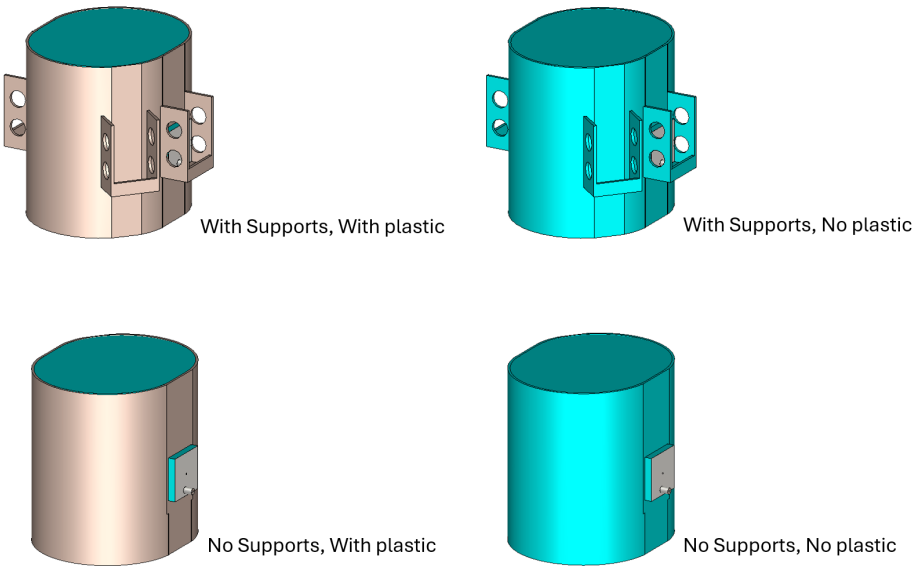

Figure 37: The four phantom variants

This quadruple setup allows us to independently check the effect of the plastic shell and of the supporting structures. The results are shown in Figure 38.

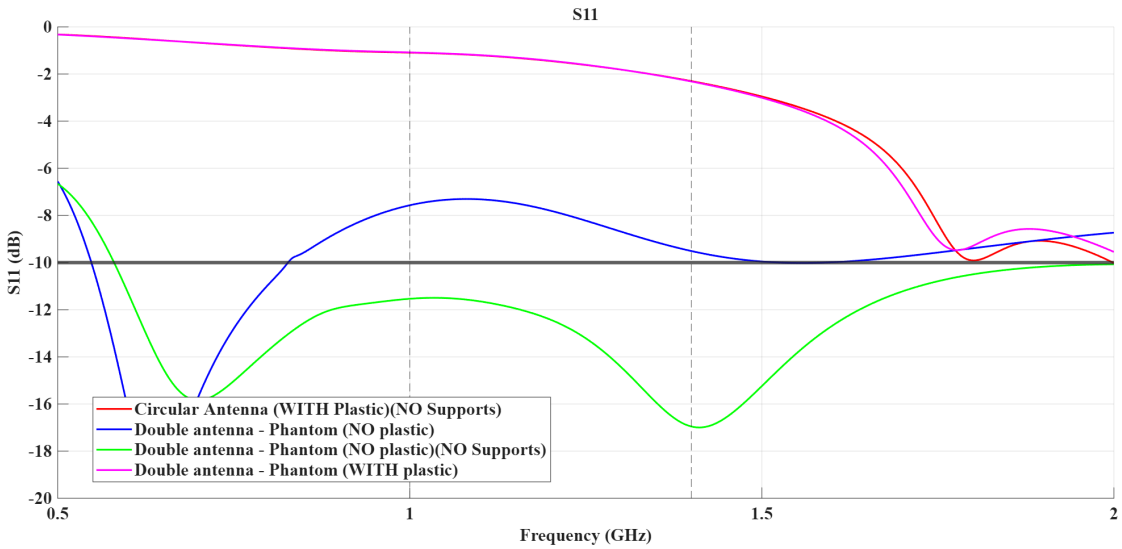

Figure 38: The S11 curves of the circular antenna on the four phantom variants

As expected, we can see that eliminating the supporting structures and switching the plastic material with the same material of the core yields a curve very similar to the one we obtain with the cube phantom. Notably, the circular antenna seems to be also influenced by the structures around the shell, as a significant difference can be noted seen between the two variants without plastic. This effect is however negligible when the latter material is reintroduced, signifying that the main element of performance disruption is the gap between the sensor and the tissues. To verify the correctness of the simulations in terms of consistency with the rules of physics, it was decided to repeat them after setting the solver to work in the time domain. The purpose is essentially to solve the same computational problem through a different mathematical procedure and to see if the two results are similar. This is useful for example to spot possible problems with the meshing employed. The following image reports eight different curves: the four previously displayed continuous lines paired with the curves calculated in the time domain. The latter are shown as dotted but coloured with the matching colour of the corresponding curve in the frequency domain.

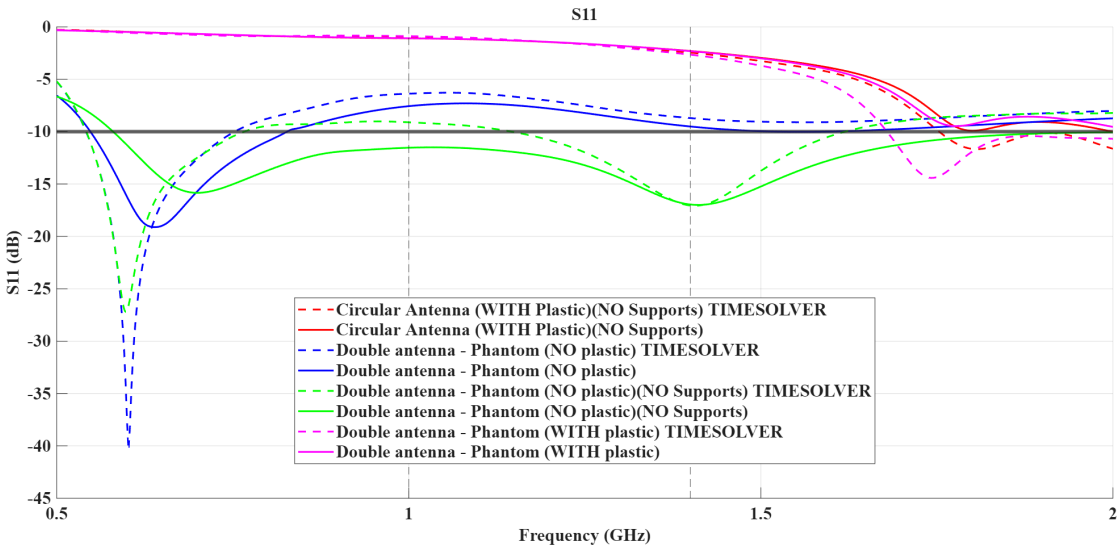

Figure 39: The S11 curves of the circular antenna on the four phantom variants with dotted lines showing the curves calculated in the time domain

The fact that the two groups of simulations are comparable validates the testing setup. The same approach can be adopted to further investigate the correctness of the setup involving the horn waveguide antenna and the plastic shell phantom. Such comparison is shown in Figure 40

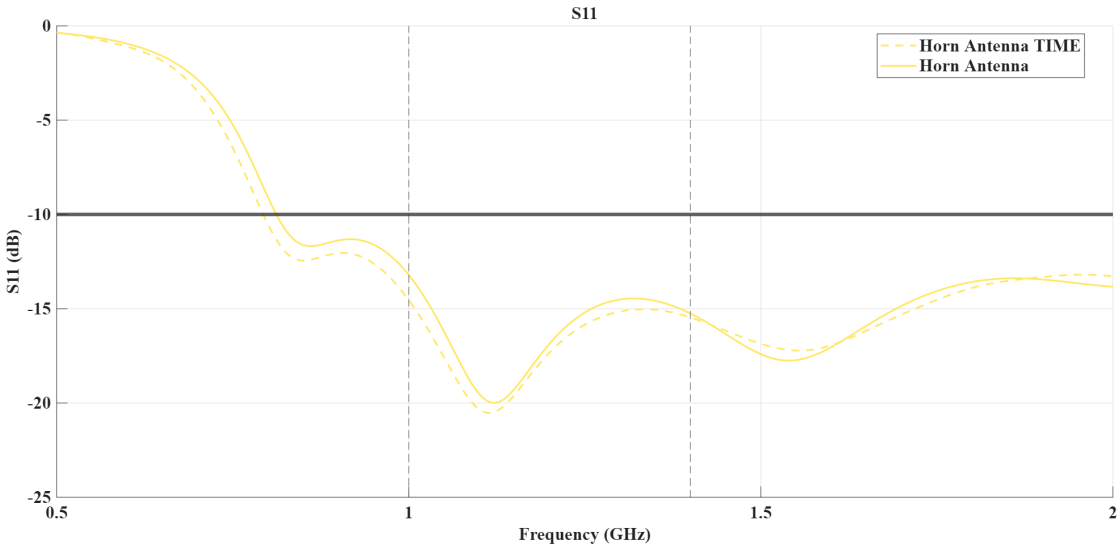

Figure 40: The S11 curves of the horn antenna with the dotted line showing the curve calculated in the time domain

Once again, we find confirmation of the alignment of the solutions found by the two

solvers.

After the careful analysis presented in this chapter, it was ultimately decided to select the double ridge filled horn waveguide antenna as the definitive subject of optimization for the specific purpose of brain microwave screening. Both the reflection curves and the field plots confirm the superior performance of this type of sensor. It also shows a much greater robustness to the presence of gaps between its aperture and the tissues. This is a critical quality, as a realistic scenario cannot be completely devoid of any gap: manufacturing imperfections, and the patient's hair could easily prevent a truly perfect contact.

Chapter 3

Antenna Optimization

3.1 The horn antenna

Horn antennas are substantially a gradual transition between a guided waveguide mode and a free-space mode. Their simple fabrication paired with their wide bandwidth makes them strong favourites for operation in the microwave band. Furthermore, their VSWR tends to be very low when they are fed with a waveguide. The main determinant of their radiation characteristics is the phase variation across the aperture that results from different path lengths from the feed to different points on the aperture. This is called phase error. If we exclude the conical horns, we can find three different kinds of rectangular horns: the H-plane sectoral horn, the E-plane sectoral horn and the pyramidal horn. They are distinguished by the orientation of the aperture, which, in the last kind, is flared in both E and H planes. The main advantage of horn antennas is their great directivity, which stems from the fact that the radiation pattern is physically contained by the metal walls of the horn itself.

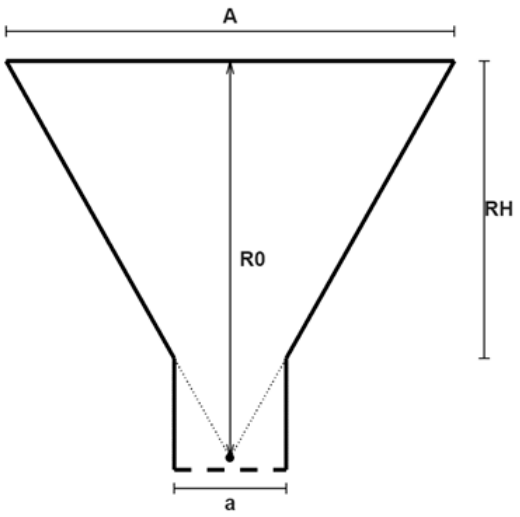

Figure 41: Simplified section of a horn antenna

The H-plane sectoral horn is a horn flared only in the H-plane. We can define its geometry with an aperture width A, a waveguide width a, and the radius of curvature R_0 of the arc defined by the angle of aperture of the horn. At the waveguide–horn junction, the tangential electric field is $E_y(x) = E_0 \cos\left(\frac{\pi x}{a}\right) e^{-j\beta_g z}$, where β_g is the phase constant of the waveguide. This depends on the transverse components of the waveguide dominant mode TE_{10} [43].

As we shift our focus from the horn input to the horn output, we can note that the impedance seen from the wave gets closer to the impedance of the free space. This means that, if we account for the phase error previously discussed, we can approximate the field at the aperture as an expanded version of the one present at the horn junction. To the end of account the error, the distance from the convergence point of the horn walls to a point x on the aperture is approximated as $R \approx R_0 + \frac{x^2}{2R_0}$. Substituting this into the horn's phase term yields the approximate aperture field $E_a(x) \approx E_0 \cos\left(\frac{\pi x}{a}\right) e^{-j\beta \frac{x^2}{2R_0}}$.

With similar steps we can analyze the case of an E-plane sectoral horn, where our approximation is instead $R_y - R_0 \approx \frac{y^2}{2R_0}$.Its substitution in the electrical field equation brings us to $E_y(x) \approx E_0 \cos\left(\frac{\pi x}{a}\right) e^{-j\beta R_0}$, where we find a in place of A because of the known linear width of the waveguide, which expands on the other plane.

The pyramidal horn (flared in both E- and H-planes) is the most common horn. Its aperture field is a combination of the two sectoral horns aperture fields. It can be approximated with $E_a(x, y) \approx E_0 \cos\left(\frac{\pi x}{a}\right) e^{-j\beta\left(\frac{x^2}{2R_H} + \frac{y^2}{2R_E}\right)}$.

The introduction of ridges inside horn antennas is a frequently used technique to increase the maximum usable bandwidth (MUB). This effect is similar to the one that ridges have inside waveguides, which is to lower the cutoff frequency of the fundamental mode. Such an effect is beneficial for both waveguides and horn antennas, as it allows to achieve a wider single-mode operating range before higher order modes begin to propagate. The

unchecked propagation of higher order modes leads to undesired effects in the antenna's radiation characteristics [44]. Beside the finer control on the range of propagation modes, an important role of the ridges is impedance matching. This is the reason why ridges have an exponential shape. The ridge dimensions (height and width) are tuned to ensure that the associated impedance creates a smooth transition from the low impedance of the waveguide to the high impedance of free space. Sometimes the exponential equation of the ridge profile is modified to include a linear component, enabling a smoother transition [45].

3.2 Optimization Strategy

Before starting to optimize the antenna's geometry, a few choices have to be taken. The first of these is the nature of the antenna feed that we want to use in our simulations. This critical decision stems from the need to find a compromise between simulation accuracy and computation time, as the optimization process involves a great number of tests to find the best combination of parameters. In this case, after carefull consideration, the three possible feeds to pick from were chosen to be a coaxial feed (the one used until now), a point-to-point discrete port, and an edge-to-edge discrete port. The first of these three is expected to be the most accurate, as its the one that most closely reproduces the real-world scenario. However, this comes at the cost of the longest computation time. The other two feeds are essentially a direct imposition of a differential input between the two internal faces at the innermost ends of the ridges. This eliminates the need for a waveguide port placed on the top face of the coaxial cable, which requires more resources in terms of calculations. Figure 42 shows the three different feeds applied on the horn antenna.

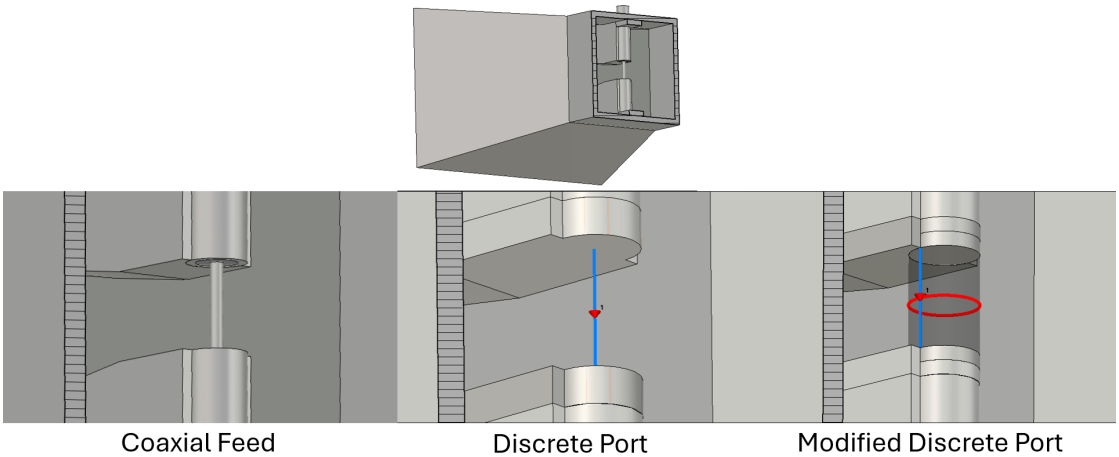

Figure 42: The three considered feeds

The tests were conducted with a more realistic filling material, alcohol, and were validated with the time domain solver after the initial frequency domain simulations. The

reflection curve of the coaxial feed can be taken as a reference to evaluate the accuracy of the other two. As it can be seen, the edge-to-edge feed gives us a curve that is close to the one of the coaxial feed, and is also much faster to simulate. Furthermore, the curves in the frequency domain and in the time domain are substantially identical. The point-to-point feed on the contrary appears far from the reference, and the two domains appear to divergence very early. This led to the selection of the edge-to-edge feed as the most fit for the optimization process.

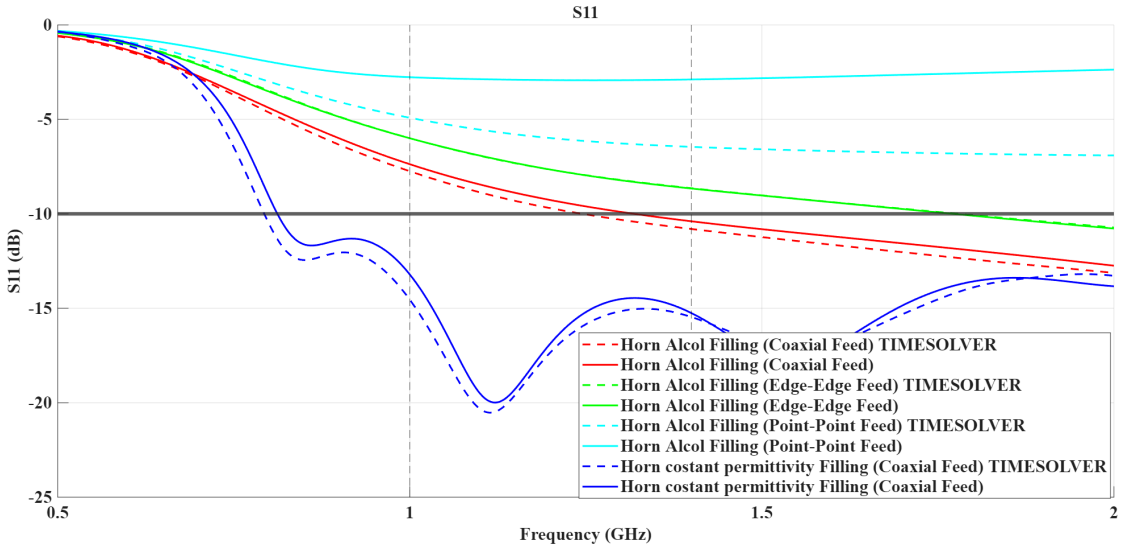

Figure 43: The S11 obtained using the three different feeds. Both frequency and time domain solvers were used

After the choice of the feeding type the next necessary step is the fixing of the mesh. This allows to both avoid a completely automatic meshing by CST Studio, which is subject to variability, and to optimize the computational load on the computer. In this process, the mesh of the antenna is first simplified to a low tetrahedron version, where the meshing is sparse. Then a specific portion of the model is set to receive a denser meshing. The S11 curve obtained from this new meshing is compared to the one obtained by a simulation where mesh refinement was operated by CST Studio, which is considered the most accurate rendition of the model. By repeating these steps a number of times, the reflection curves gradually approach convergence to the reference curve. In this case the baseline curve was obtained on a model of the antenna filled and immersed in the average brain material, with mesh refinement enabled. The areas that received finer meshing were the feed core, the bottom of the antenna cavity, the top surface of the ridges and a ring-like portion of the walls around the feed. Since every result was shown to be close to the reflection parameters of the baseline, the best compromise between accuracy and number of tetrahedrons was chosen.

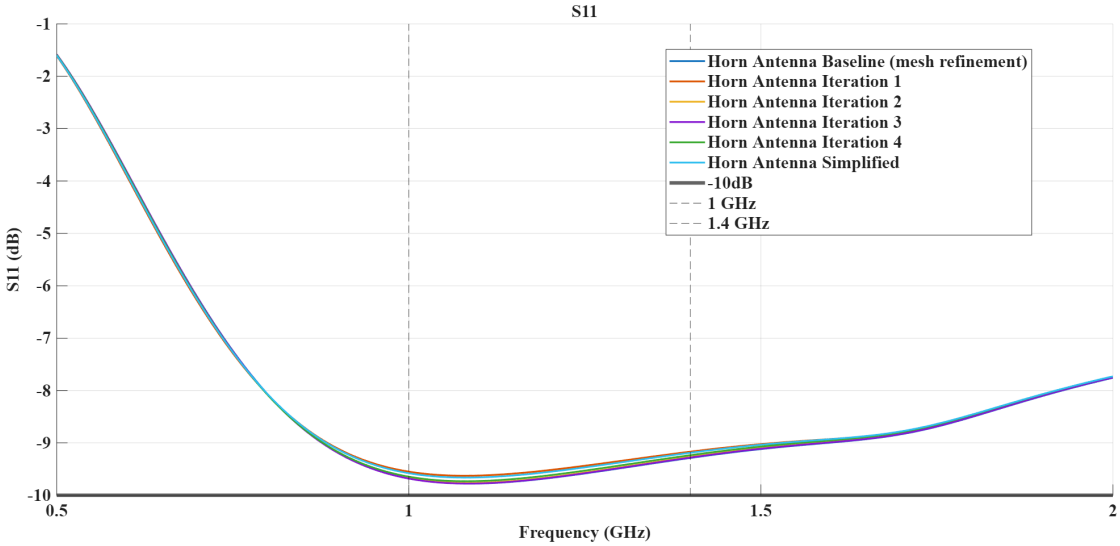

Figure 44: The S11 obtained in the mesh fixing process

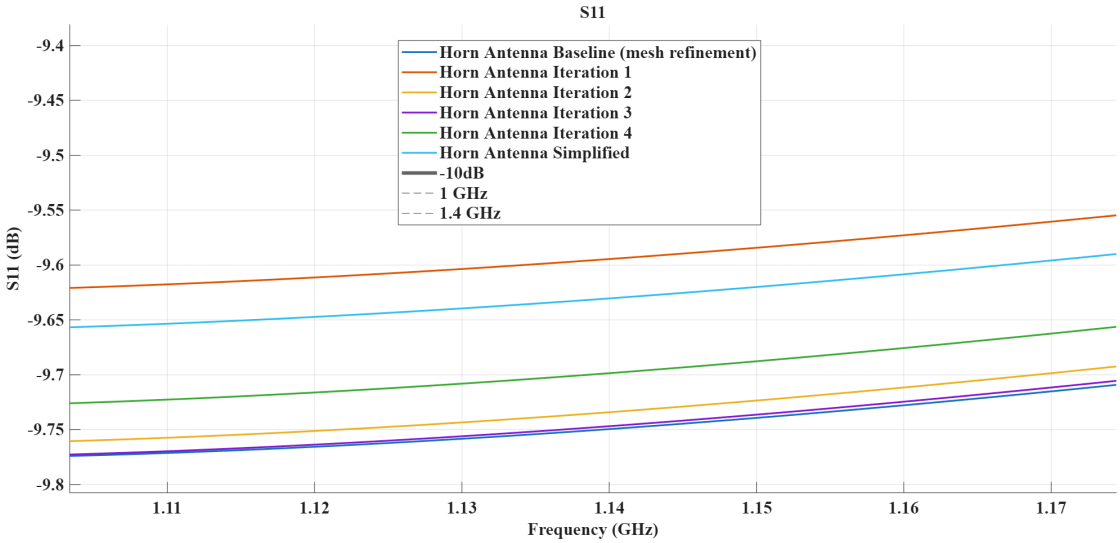

Figure 45: Zoom on the previous figure

Once the mesh was fixed, the filling material had to be selected for optimal guiding of the EM waves inside the phantom. An important requirement of the simulated materials was the fact that they had to be within the manufacturing capabilities of the Wavison team. Moreover, the filling material had to be easily loaded and contained within the horn waveguide. Lastly, the material should be as easy to preserve or substitute as possible. The simulations were run with five different materials: alcohol, water, ECO40 rubber, ECO45 rubber and a specific mixture of water, gelatine and flour used by Rashid et all. [26].

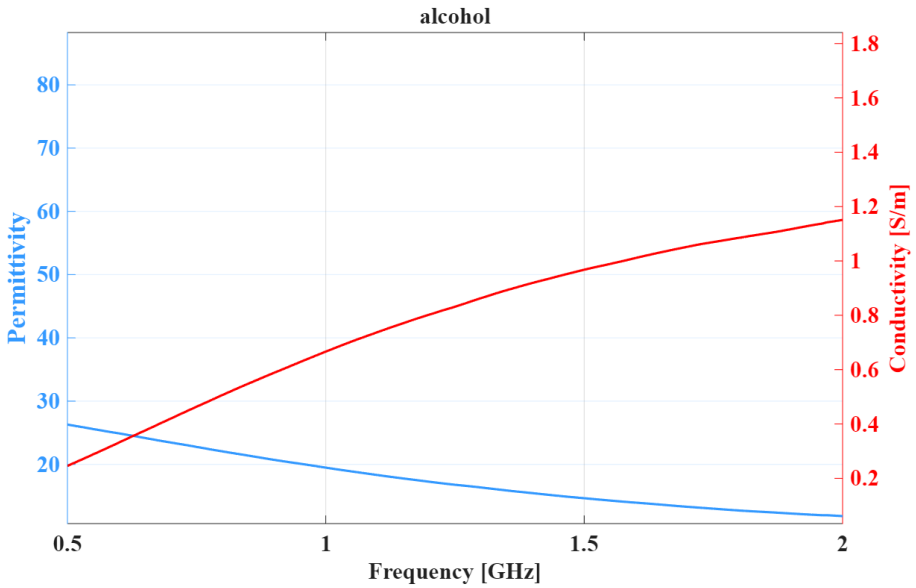

Figure 46: Relative permittivity and conductivity of alcohol

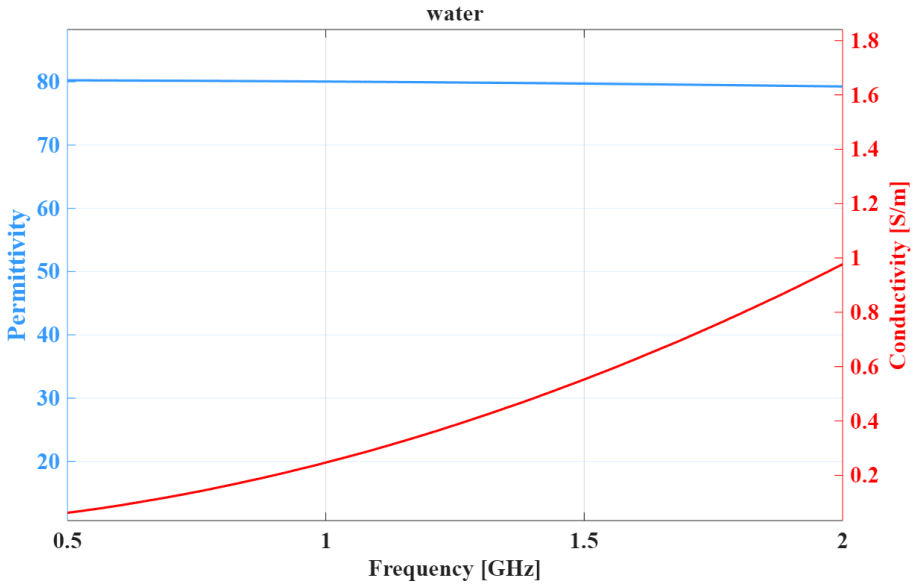

Figure 47: Relative permittivity and conductivity of water

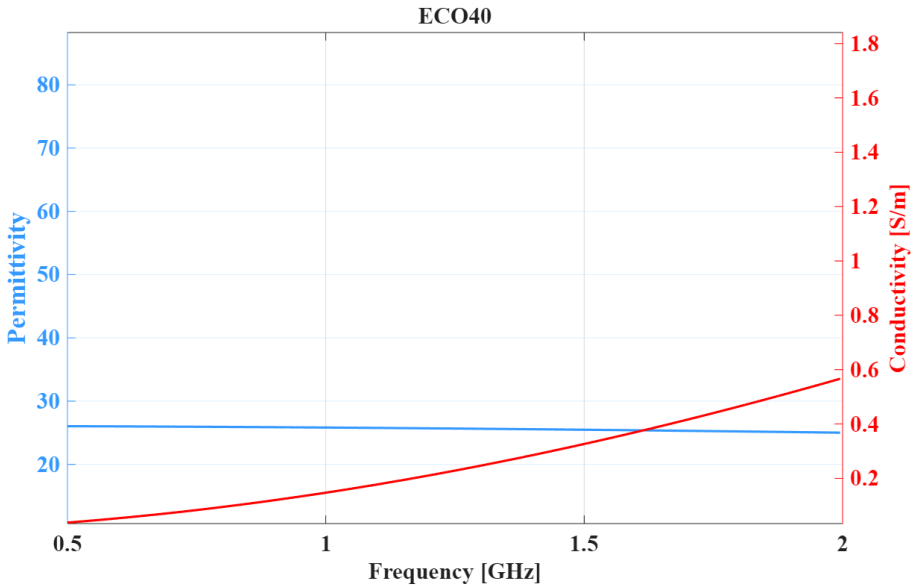

Figure 48: Relative permittivity and conductivity of ECO40 rubber

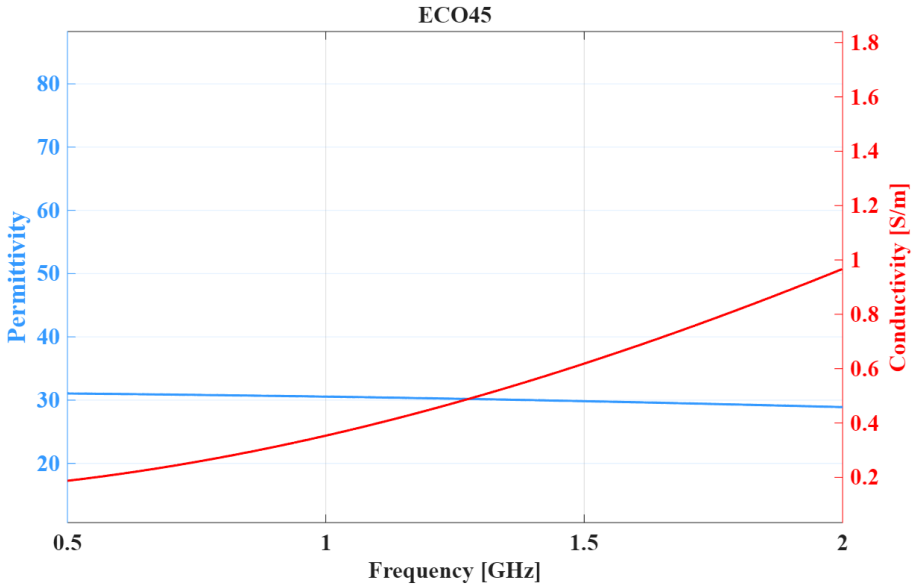

Figure 49: Relative permittivity and conductivity of ECO45 rubber

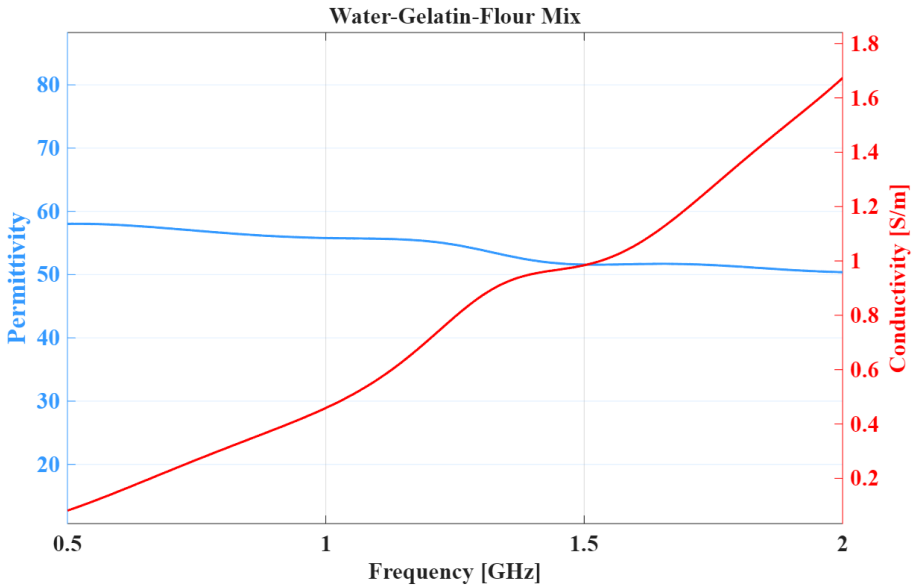

Figure 50: Relative permittivity and conductivity of the water, gelatin, flour mixture

The materials were used in the filling portion of the antenna on a double horn simulation on the plastic shell phantom over the consolidated range of frequencies. This allowed to assess the impact of the filling material not only on the reflection coefficient, but also on the transmission coefficient. Figure 51 and Figure 52 show the results of these trials.

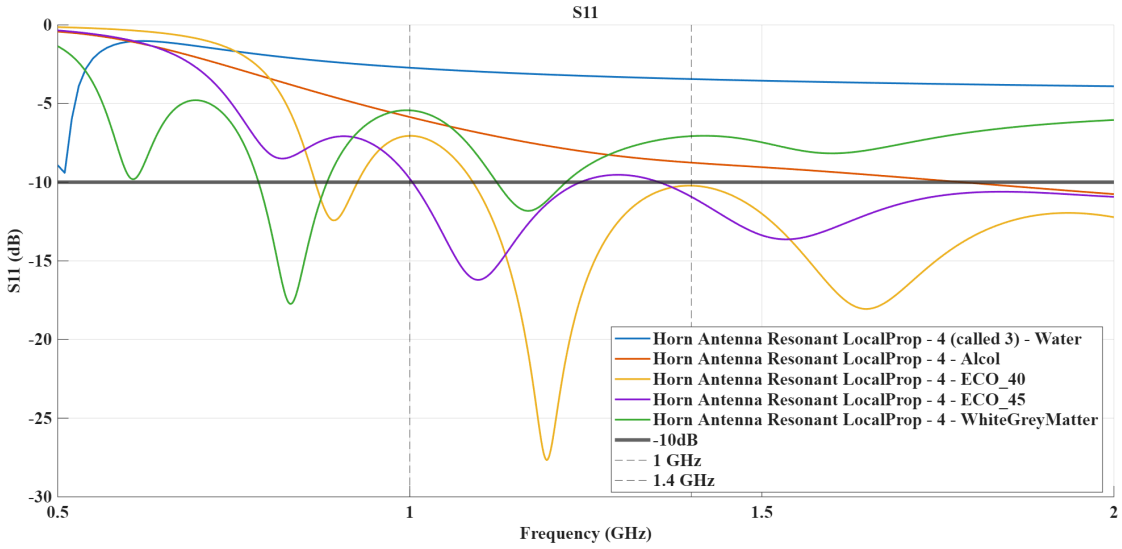

Figure 51: Reflection coefficients obtained in the material trials

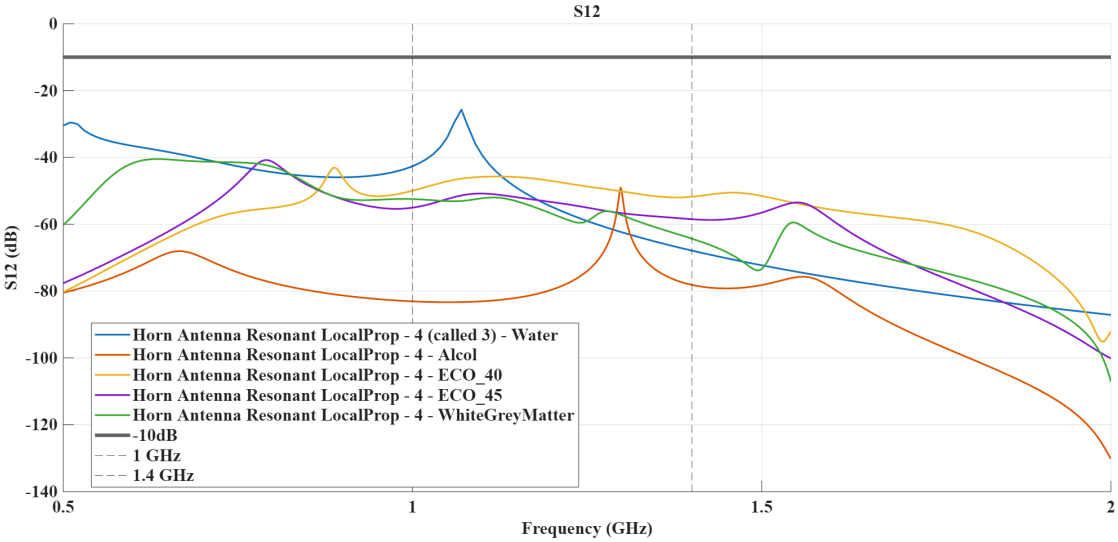

Figure 52: Transmission coefficients obtained in the material trials

ECO45 was found to have a wide resonance peak at a frequency close to 1 GHz, while having an S12 transmission curve within the expected values. Its relative permittivity is also almost identical to the value of the original costant-permittivity material used in the first simulations. These characteristics, together with compliance with the aforementioned requirements, led to the selection of this material as the definitive filling for the optimization process.

The final phase of optimization focused on geometry optimization. The base for this activity was the use of parametric sweeps. Parametric sweeps allow to test the same simulation scenario with a number of different combinations of geometric values that define the shape of the antenna. Thanks to this approach we obtain a great quantity of different reflection coefficient curves that reflect the performance of the sensor in our specific setup, hence reaching a device optimized for our purpose.

Four parameters were the chosen values of the procedure: vertical aperture (in our case it is perpendicular to E-field direction, since the feed is horizontally placed), horizontal aperture (parallel to the E-field direction), back chamber depth and back chamber side. In the next figure (Figure 53) they are respectively indicated by the letters ah, bh, lw and L. The starting values of these parameters were 43, 30, 20 and 9 mm. The aperture values include the 1 mm thick walls of the antenna. The optimization followed a procedure of twofold supervision: each parametric combination was tested on both the average brain cube and on the plastic shell phantom, a choice mindful of the difference between gap and gapless scenarios. The efforts were therefore oriented towards the individuation of a sensor as tolerant as possible to the presence of gaps. First, a very sparse parametric sweep on all four values was launched to identify the general trends deriving from big variations of the dimensions, such that an indication of values to avoid could be obtained, together with the most promising ranges. Then a second denser parametric sweep was used to select the best combination of values, proceeding in order of the most influent parameter between the four analysed. This second sweep led to the identification for both phantoms of three

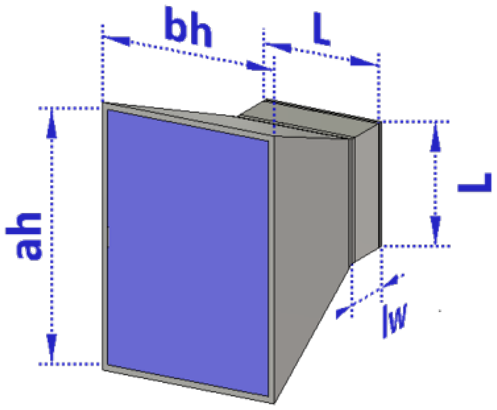

Figure 53: A visual representation of the investigated parameters

main clusters of results in terms of S11 curves, each one with its general tendencies of resonance frequencies and bandwidth. The main parameter separating these clusters was L, which was therefore the most influent parameter between the four.

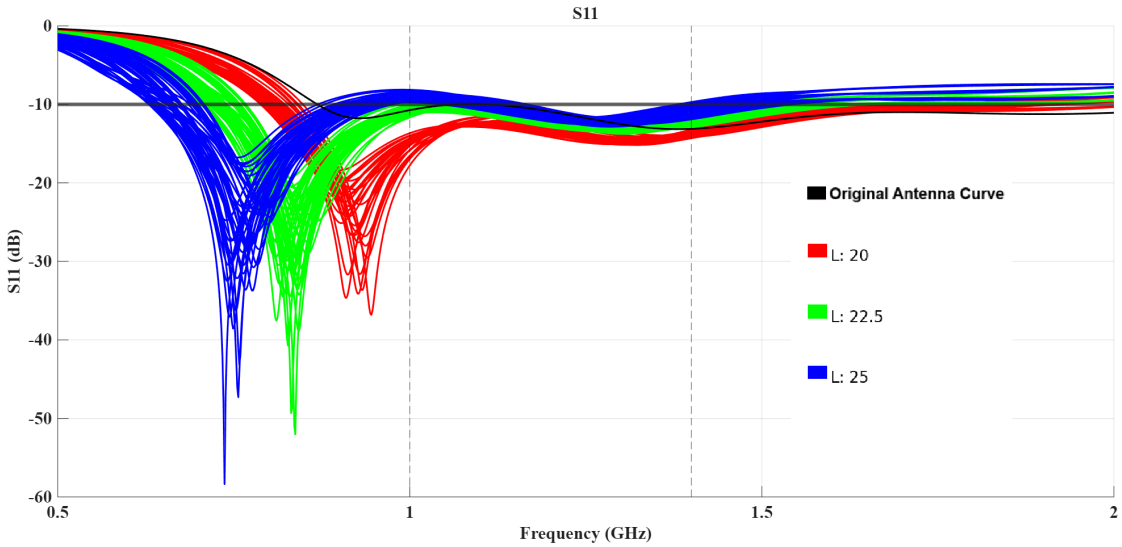

Figure 54: The three main clusters of S11 curves obtained on the cube of average brain material

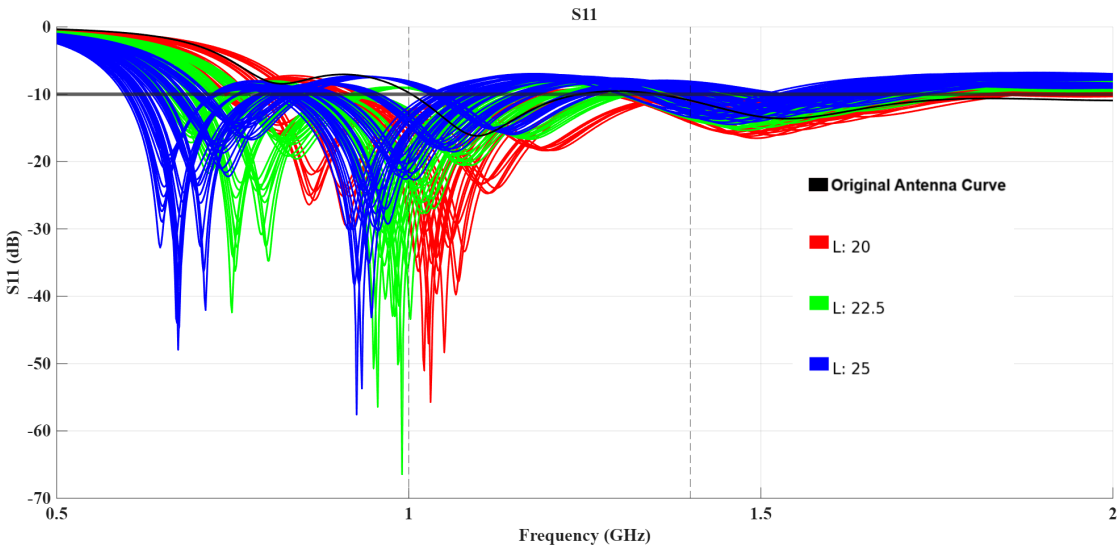

Figure 55: The three main clusters of S11 curves obtained on the plastic shell phantom

In both simulation setups the cluster with a back chamber side of 20 mm contains curves that tend to show a resonance in the 0.8 to 1 GHz. For this reason the investigation continued inside of this parametric region, and the other clusters were discarded from the collection of results. The next leading parameter in terms of impact on the simulation results is shown to be ah, the aperture in the direction perpendicular to E. Figure 56 and Figure 57 highlight the five clusters divided by the ah value of the antennas that originated them.

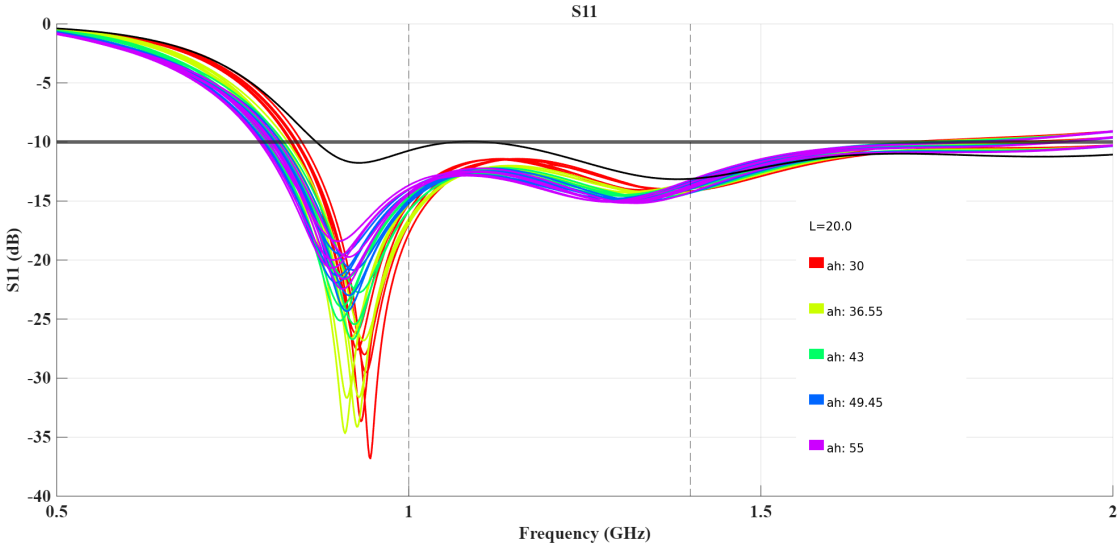

Figure 56: The five clusters of curves for the cube of average brain material

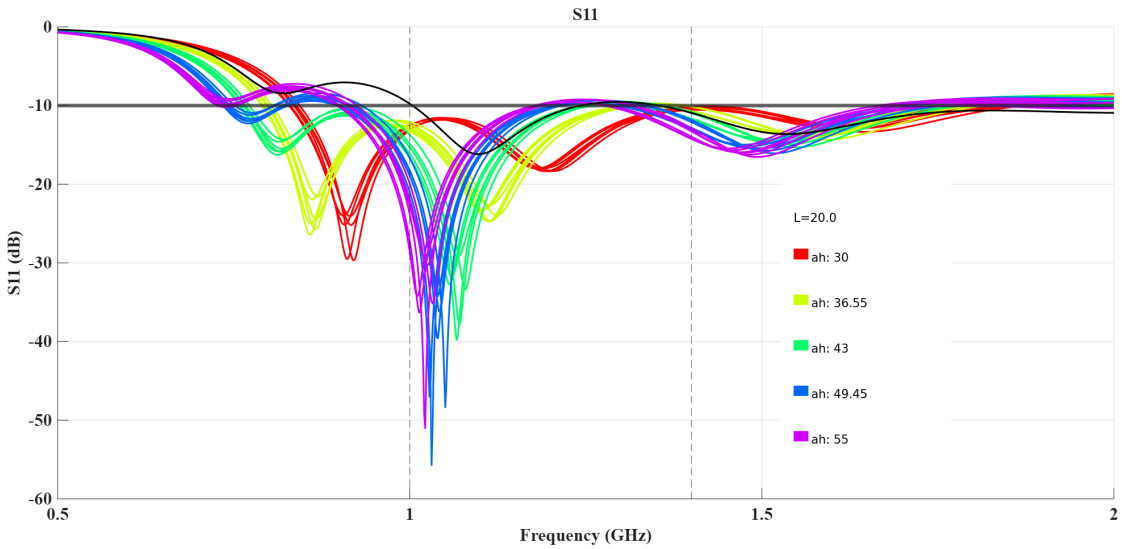

Figure 57: The five clusters of curves for the plastic shell phantom

It is immediately clear that the value of 30 mm yields the strongest resonance between the considered values. It was then chosen this value to proceed with the search for the best combination of parameters, eliminating the other curves.

At this point, plotting the six remaining curves allows not only to choose the best value of bh, but also the best value of lw.

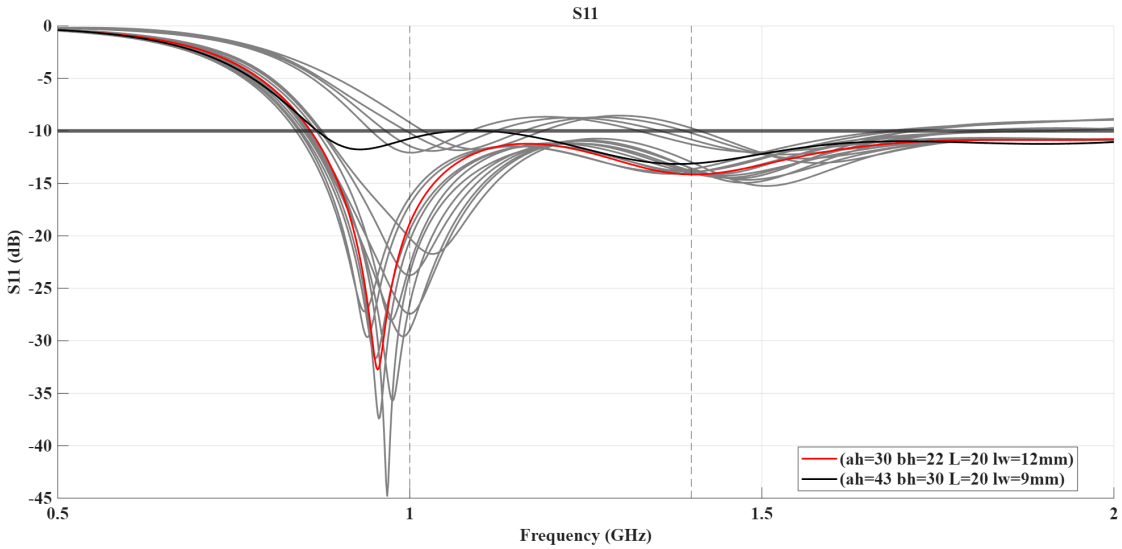

Figure 58: The six remaining curves for the cube of average brain material

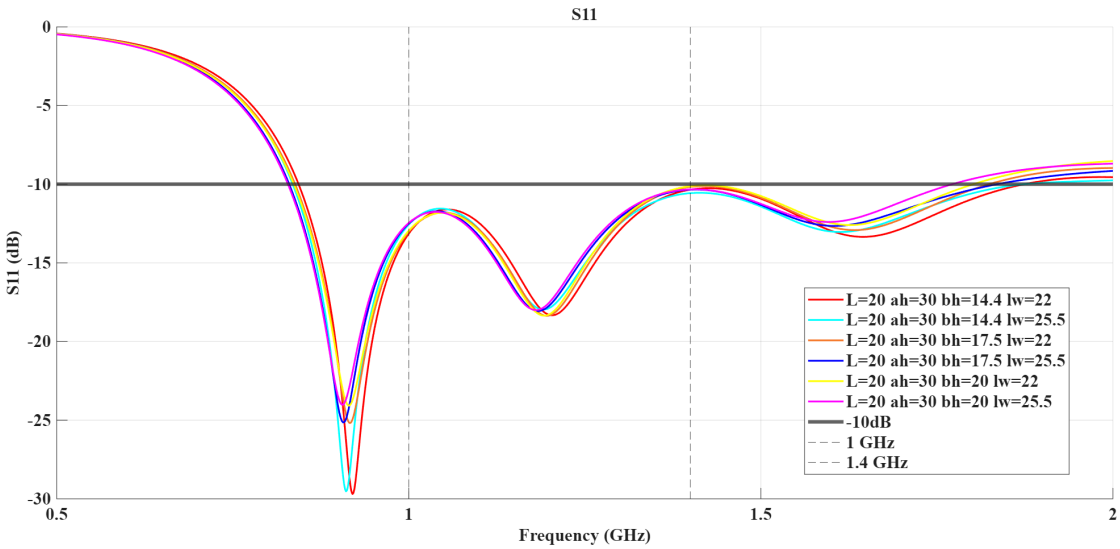

Figure 59: The six remaining curves for the plastic shell phantom

This could be the end of our optimization process. However, noticing the interplay between the effect of lw, which seems to shift the resonance frequency, and the effect of bh, which seems to affect the resonance intensity, it was decided to launch a third and final sweep. This final step focused on the individuation of the best combination of lw and bh. The calculation of 16 different sets of value yielded the final empirical proof that 12 mm for lw and 22 mm for bh was the couple that allowed for the strongest resonance in the plastic shell phantom. These values were only the second best choice for the average brain cube but it was nonetheless selected as it represents a less accurate scenario in respect to the other target

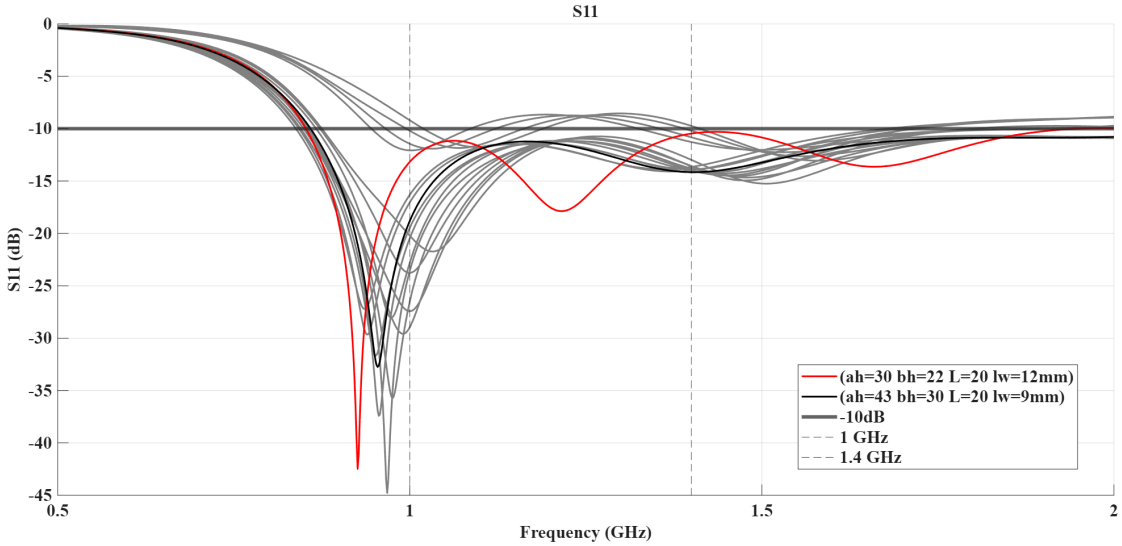

Figure 60: The final sweep for the average brain cube

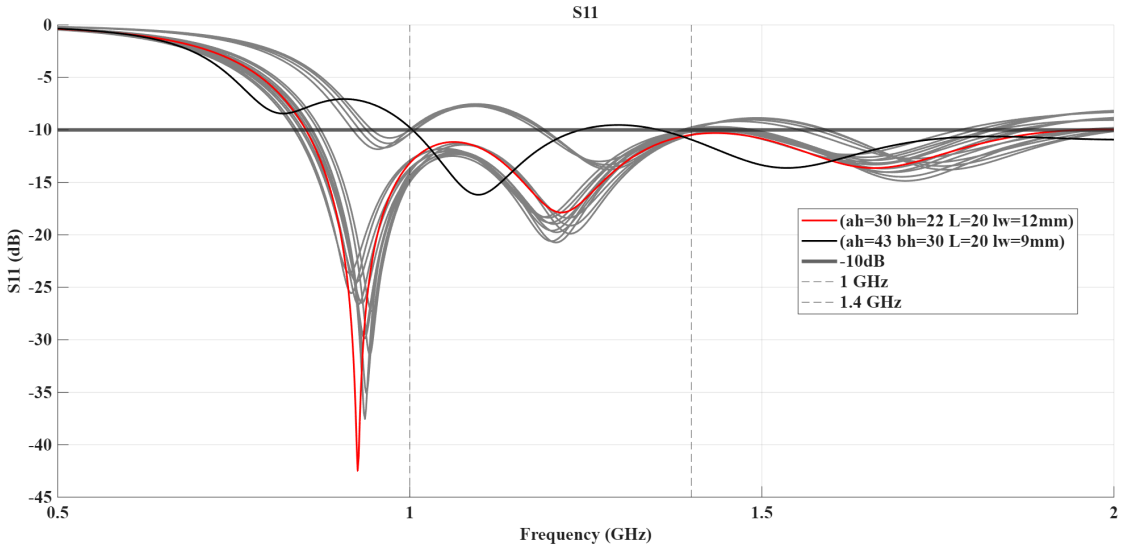

Figure 61: The final sweep for the plastic shell phantom

The last validation for the final design involved the simulation of the new combination of parameters with a coaxial feed and with the enabling of automatic mesh refinement in order to test it more accurately with a much longer computation time. In the next figures we see the reflection and transmission curves of the final design compared to the starting version of the sensor. The target was the plastic shell phantom.

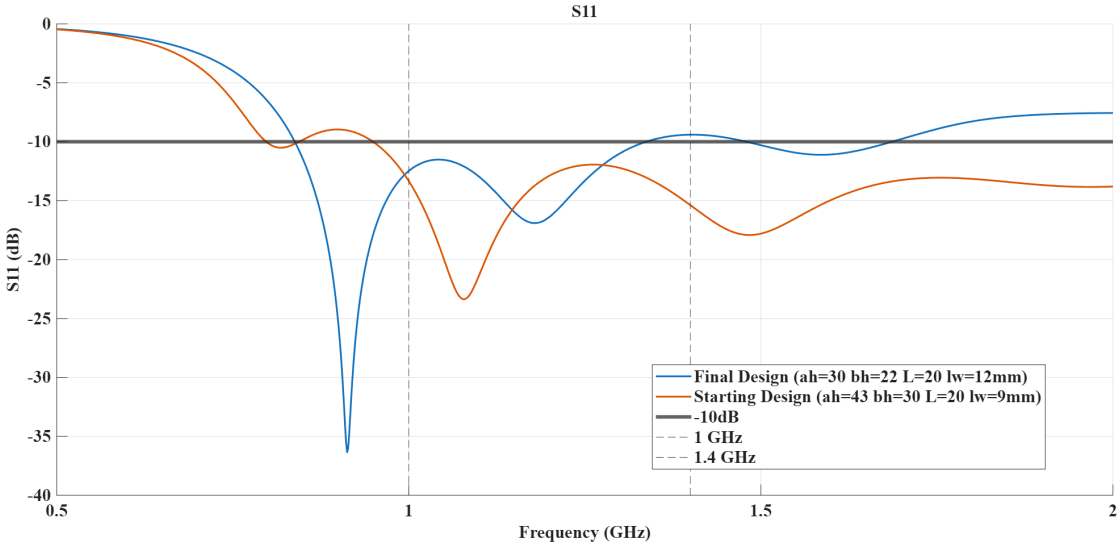

Figure 62: The reflection coefficient of the final antenna compared to the starting one

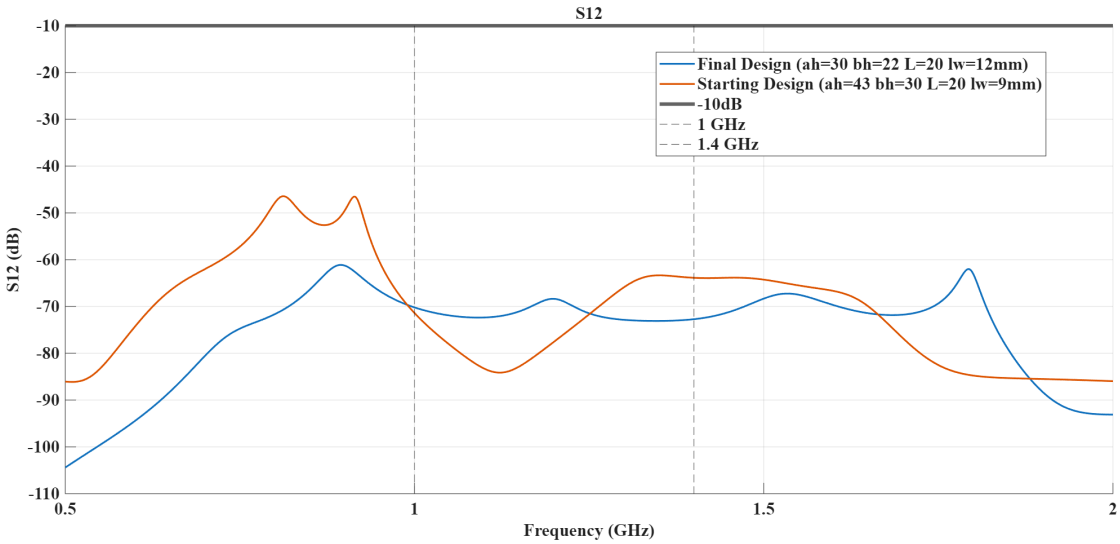

Figure 63: The transmission coefficient of the final antenna compared to the starting one

The final optimized antenna operates in the -10 dB band from 0.84 to 1.34 GHz while maintaining a compact footprint of 31×23 mm^2. Its height is equal to 44.5 mm. The optimization process was therefore succesfull in making the antenna not only perform better, but also more compact. Figure 64 shows a visual comparison of the starting design and the final design.

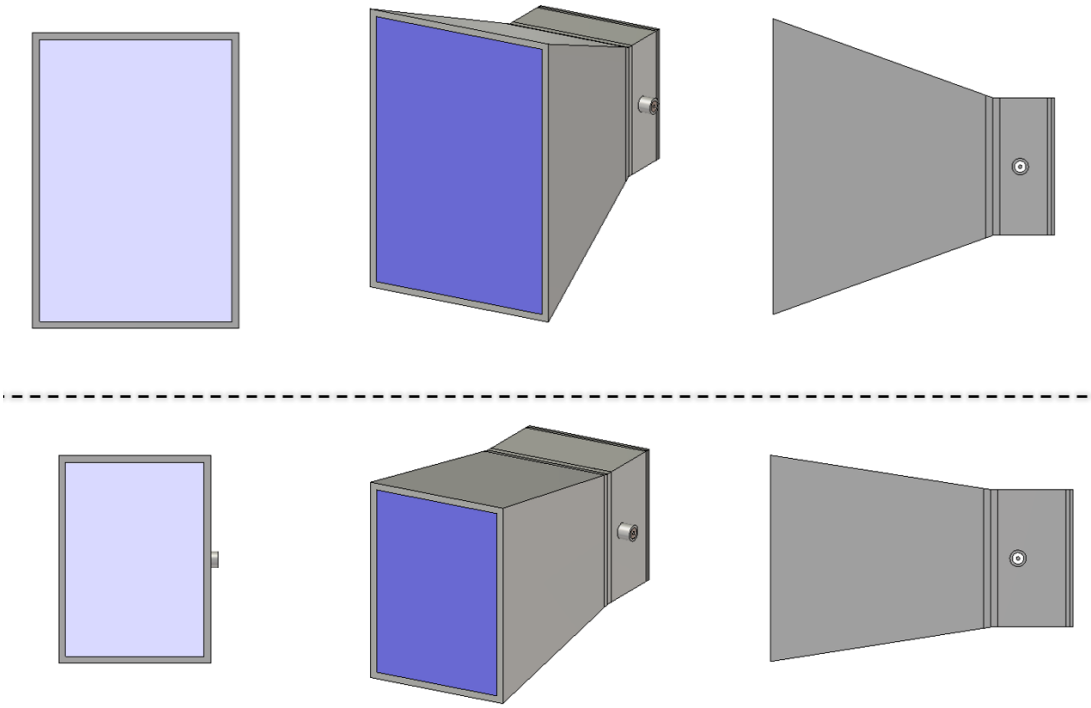

Figure 64: Starting antenna above (ah=43 bh=30 L=20 lw=9mm), optimized antenna below (ah=30 bh=22 L=20 lw=12mm)

Figure 65 shows the directivity plot of the antenna in the near field for both planes of radiation on the average brain cube. They were computed by calculating the power flow density on each point of two semicircles of 10 cm of radius on the XY and XZ planes, then normalizing it by the average power flow density that enters the cube at the interface between the antenna and the cube, similarly to the way it was done by Pishnamaz et all. [46].

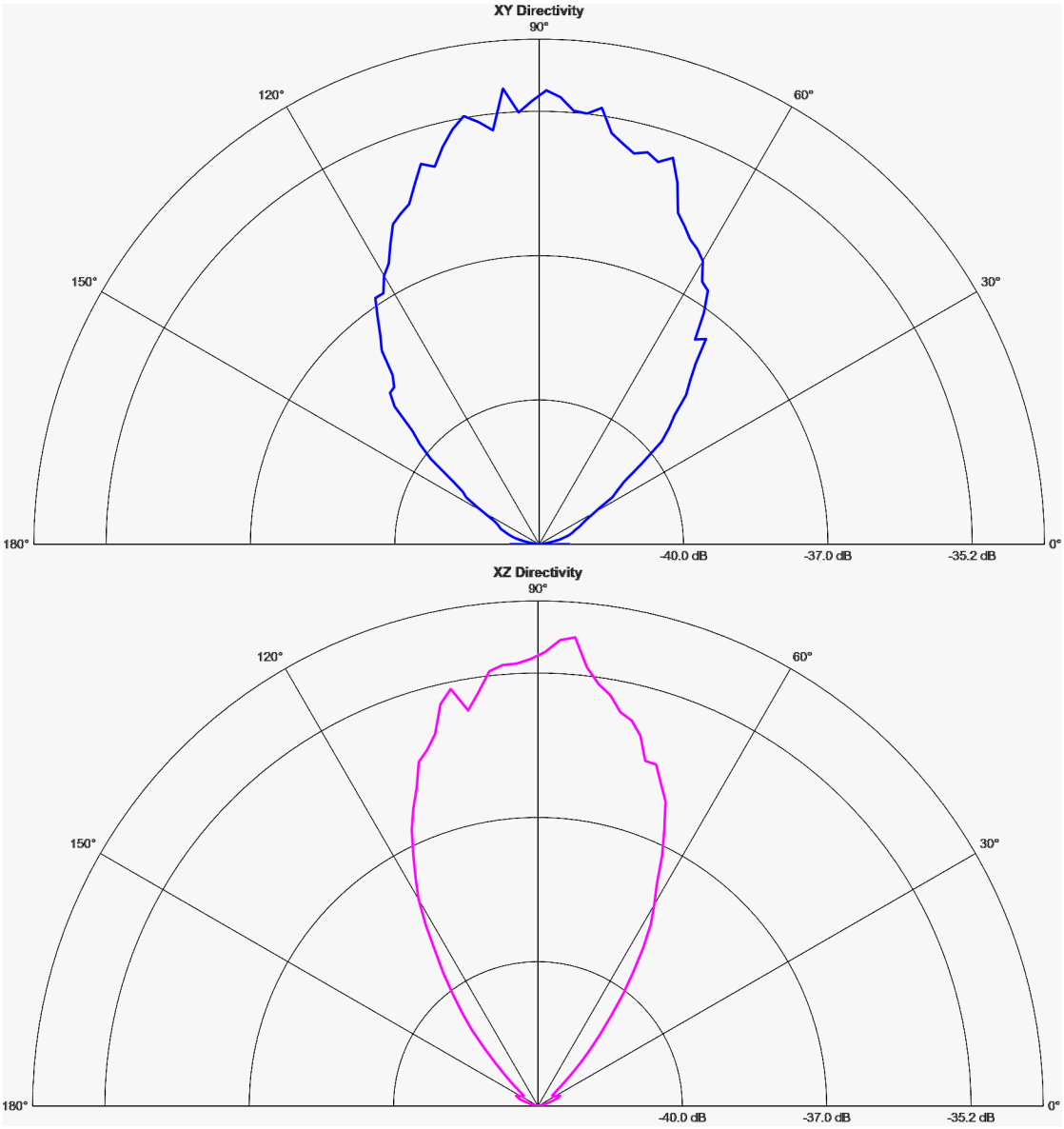

Figure 65: Directivity plots of the antenna in the near field.

3.3 Lab Testing

The last phase of this thesis was the lab testing. In order to manufacture the prototypes of the antenna, a 3d model had to be finalized with the necessary precautions for the testing. In order to guarantee mechanical stability, the walls of the antenna were thickened by 1 mm. This was done by expanding outwards the external surface. This did not affect the performance of the antenna, as confirmed by the computational simulation of this new version of the sensor. Furthermore, three circular hole were created to accommodate a

straight 2 hole flange SMA jack, which needs a central hole to be inserted and two side holes to get screwed in place. The model was now ready to used for manufacturing.

Several aluminium and copper prototypes of the antenna were then produced and brought to the lab of the Department of Electronics and Telecommunications of the Politecnico di Torino. The prototypes are displayed in Figure 66.

Figure 66: Fabricated antenna prototypes in aluminum and copper for microwave testing

To connect the input with the bottom of the antenna, a segment of RG402 semi-rigid coax cable was cut and stripped of its outer conductor on both sides, leaving the inner conductor and dielectric exposed. At one end, an SMA pin was soldered to the exposed conductor, and the segment was then soldered to the SMA connector. Screwing then the connector to the antenna allowed to place the anima of the cable against the bottom of the horn, providing differential input. Hot glue was then poured around the borders of the connector's flange, to the end of making the seal waterproof.

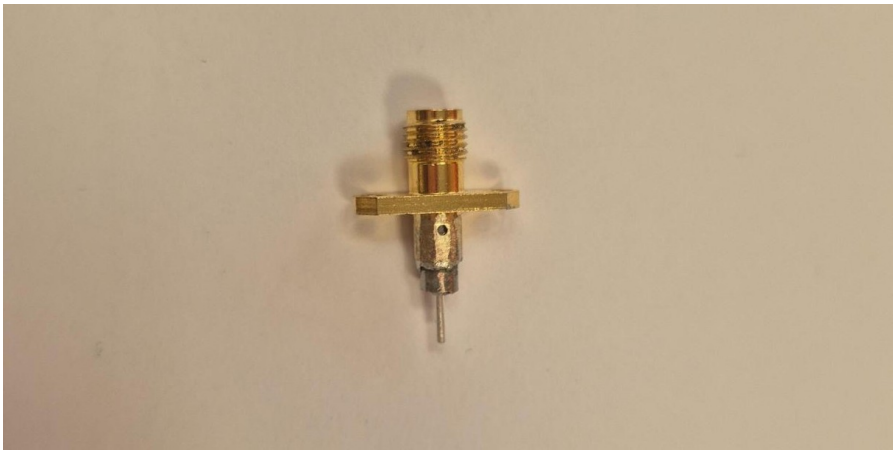

Figure 67: The prepared SMA connector with the soldered coaxial segment exposing its inner conductor

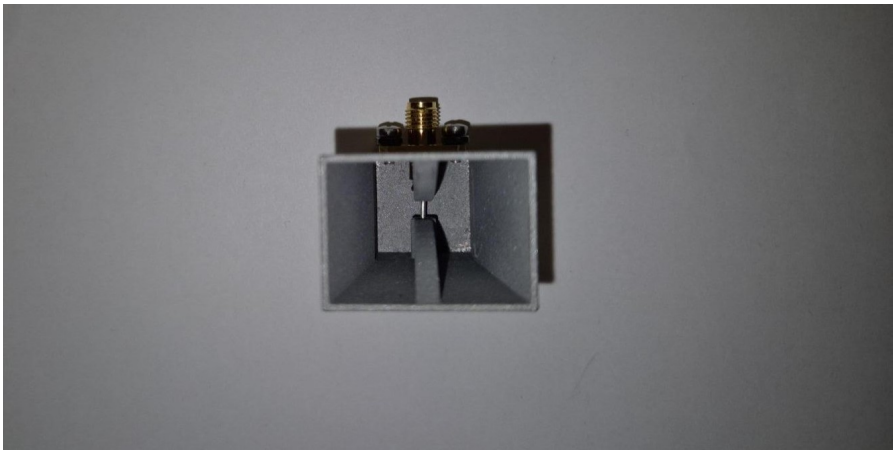

Figure 68: The inner conductor inside the core of the horn

Once the sensor were ready, a dielectric probe was prepared to measure the permittivity and conductivity of the mixtures for the filling of the antennas. These mixtures were in fact prepared just before the measurement to avoid the alteration of its properties. Moreover, the software for the probe had to be calibrated at the start of the process to ensure the highest precision. The calibration involved three measurements, specifically the measurement of an open circuit, a short circuit and a liquid with known dielectric properties, which in our case was water. The code used for this process of calibration was a courtesy of Marta Cavagnaro and Giuseppe Ruvio [47].

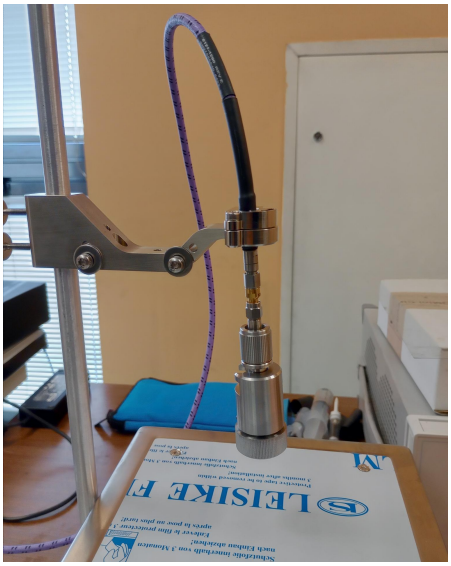

Figure 69: Dielectric probe setup for measuring relative permittivity and conductivity of filling materials

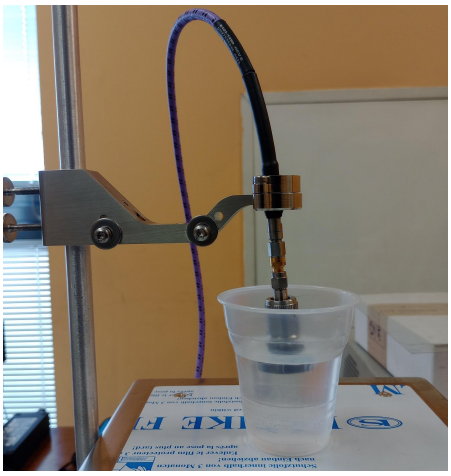

Figure 70: Distilled water sample probed for calibration of dielectric measurements

In order to avoid the long drying process of ECO45 rubber, another kind of filling was chosen. This alternative filling was a mixture of Triton and distilled water, at mass percentages of 34.4% and 65.6% respectively. This allowed for properties similar to the rubber filling, as shown in Figure 71. These substances produced a viscous material that could undergo shape changes. The antennas were then filled with the mixture and their opening were sealed with thin plastic sheets fixed with adhesive tape.

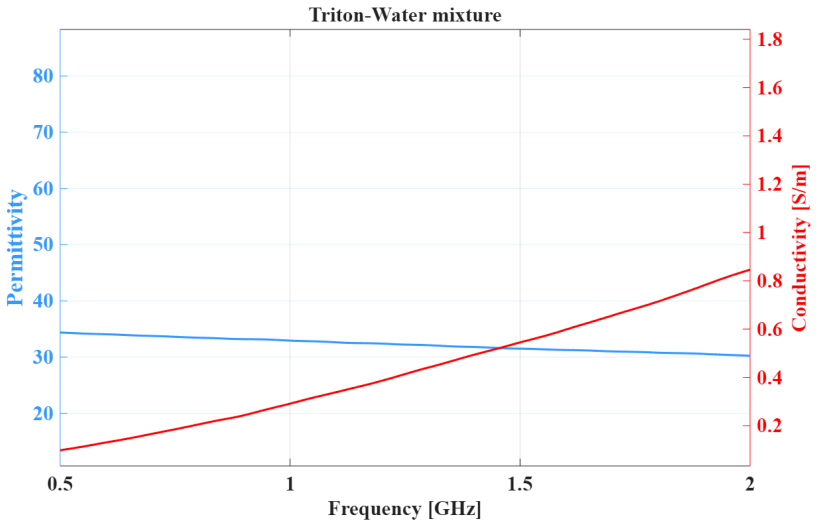

Figure 71: Relative permittivity and conductivity of the Triton-water mixtures

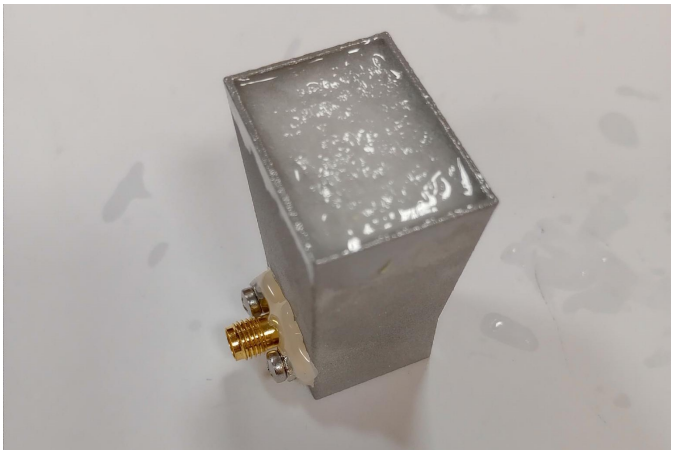

Figure 72: Antenna filled with a Triton–water mixture to tune dielectric properties

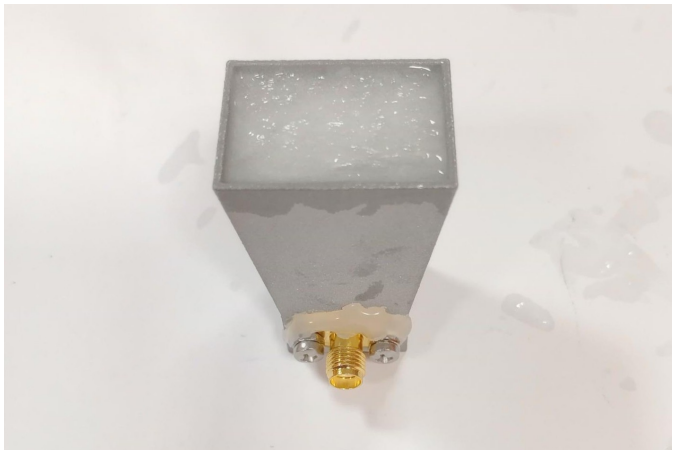

Figure 73: Filled antenna sealed with a thin plastic sheet and adhesive tape

The liquid representing the average brain material was then prepared with a combination of alcohol, distilled water and salt [10], which was then poured inside of the physical twin of the plastic shell phantom used in simulations until now. The antennas were then connected to the Keysight Virtual Network Analyzer (VNA), and then mounted on the supports of the phantom.

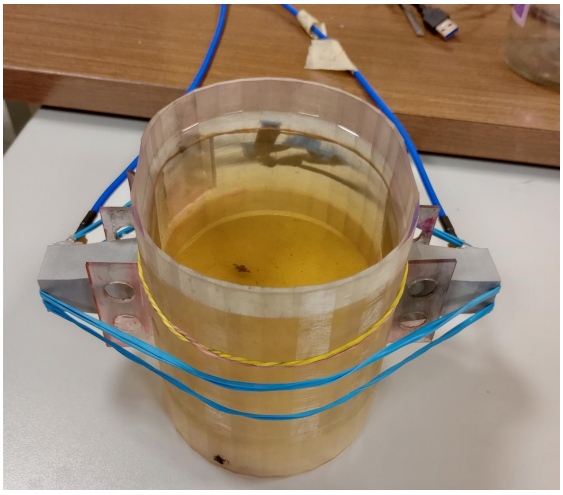

Figure 74: Placement of antennas on the phantom shell for microwave exposure

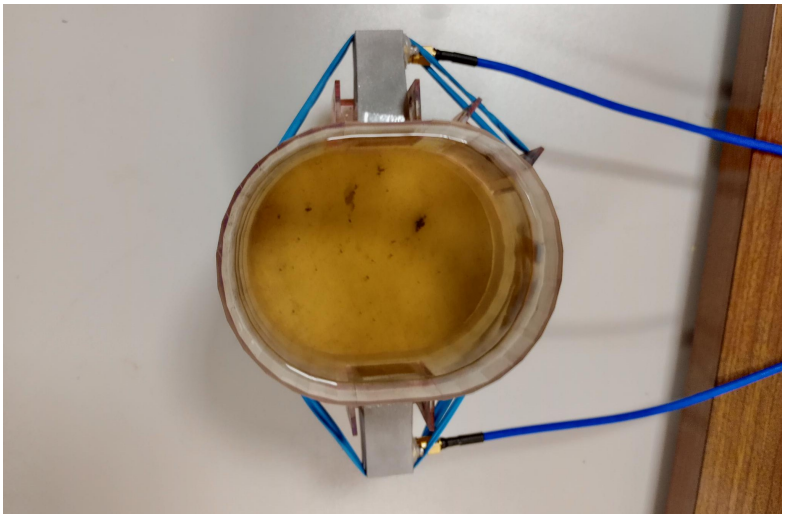

Figure 75: Top view of the antenna configuration on the phantom shell

Figure 76: Complete testing setup including PC, VNA, phantom shell, and antennas

After everything was set up, the VNA test was launched and the two antennas took turns in emitting an impulse of 0dB (1 mV) and receiving the transmitted power. This allowed for the calculation of the reflection and transmission parameters. Figure 71 and Figure 71 show us on the same plot the measured parameters and the simulated parameters of the antenna.

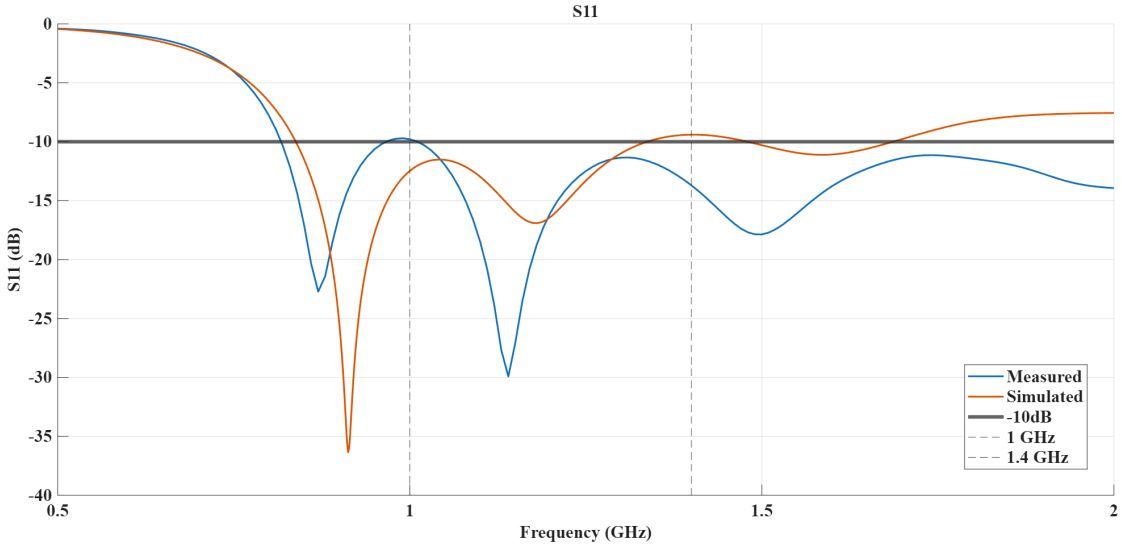

Figure 77: Comparison of measured and simulated S11 curve

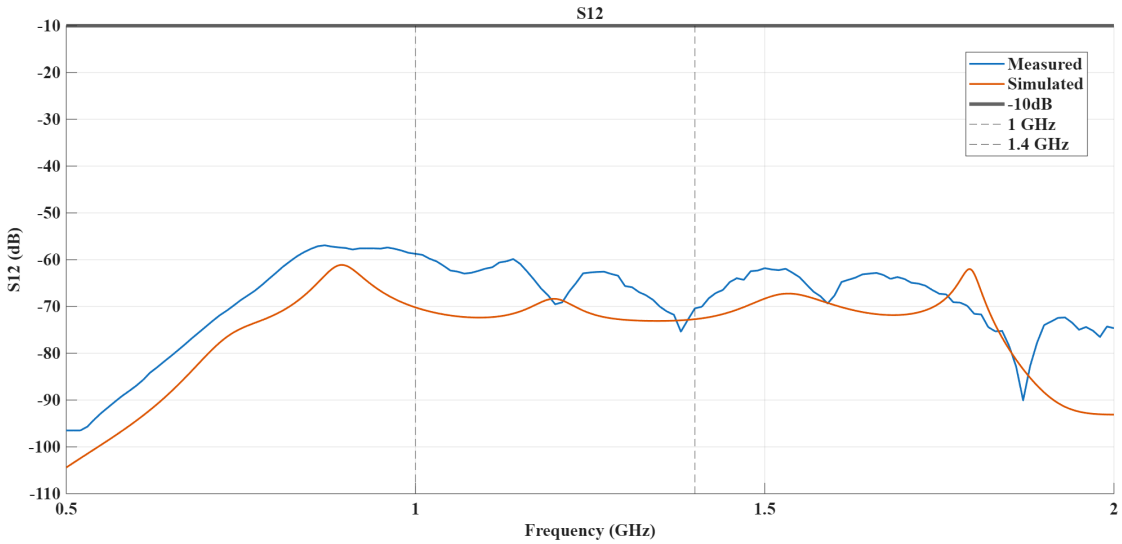

Figure 78: Comparison of measured and simulated S12 curve

The two sets of values are comparable and show differences compatible with manufacturing defects and tolerances in fabrication, assembly, and measurement setup. Resonance frequencies appear slightly lower, and their intensity is weaker, as expected from a real world scenario where noise and imperfections are present.

Chapter 4

Conclusions and Future Work

In this Thesis, the selection, optimization, realization, and testing of a compact on-body microwave antenna for brain screening has been successfully performed. The antenna, which is designed to be integrated with the stroke monitoring system developed by the Wavision Research group, is specifically optimized for microwave sensing and imaging tasks in medical context. The strength of microwave systems in the diagnostic field resides several factors, including their absence of ionizing radiation, paired with the ability to sense dielectric contrasts in the human body. This kind of contrasts is the one generated by the presence of abnormal tissues like blood cloths or ruptured arteries, which present different dielectric properties that can be sensed by sensor like the proposed one. Their operational frequencies are roughly found between 0.5 and 2 GHz, while the interval between 0.8 and 1 GHz offering the best compromise between depth and resolution.

The first part of this work involved a scoping review of state-of-the-art microwave bio-imaging antennas to define requirements for the system. Key requirements included the need to minimize mutual coupling between antennas, reduce back radiation that could reflect off the environment and create artifacts, and ensure deep electromagnetic (EM) wave penetration. Using both simplified and anatomically realistic head phantoms, five candidate antennas with various geometries were chosen and examined using electromagnetic simulations. The filled-horn double-ridged waveguide antenna demonstrated better performance than the other candidates: a circular patch antenna with a parasitic element, a double-substrate bowtie antenna, a double-ridge filled-horn waveguide antenna, an edge-feed planar log-periodic antenna and a central-feed planar log-periodic antenna. The horn antenna was then selected for optimization. The main reasons for this choice were the fact that this sensor offers a deeper penetration of the EM field by lowering surface waves and back radiation. Additionally, it demonstrated increased resistance to air gaps at the tissue material-antenna interface.

The optimization strategy had its focus on the calibration of the geometry of the horn antenna, as well as the selection of dielectric filling that could best convey microwaves inside the target, while still being easily manufacturable. Horn antennas tend to offer high directivity as the metal walls physically contain the radiation pattern and the introduction of the exponential ridges increases the maximum usable bandwidth. This is achieved thanks to the lowering of the cutoff frequency of the fundamental mode. The optimization

process utilized parametric sweeps, testing combinations of four geometric parameters: E-plane aperture, H-plane aperture, back chamber depth and back chamber side length. The selection of the parameters proceeded in order of the proved importance of the values: the back chamber side length had the largest impact on resonance frequency, while the E-plane aperture was the second most influent. The other two parameters were then selected through a new parametric sweep. As a filling material, tests indicated that a material with a permittivity of 30 was the best candidate to maximize impedance matching with the brain. For the final laboratory validation a substance was used in the form of a mixture of Triton and distilled water (34.4% Triton, 65.6% distilled water). This filling was successfully used to mimic the required dielectric properties.

The successful optimization led to a final antenna that operates in the -10 dB band from 0.84 to 1.34 GHz. Moreover, it also achieved a more compact size featuring a final footprint of 31×23 mm^2. Such contained dimensions are indeed fit for the integration into a medical helmet with a tightly packed array of antennas. The practical significance of the investigation was confirmed through lab testing, where manufactured prototypes were measured using a Virtual Network Analyzer (VNA) on a physical twin of the plastic shell phantom: thanks to this step the measured reflection and transmission parameters validated the final design, as they showed minor differences with the simulated values.

The optimized horn antenna is a major improvement as it solves a number of basic issues with the practical use of microwave imaging as a brain anomaly diagnostic tool. The current project is a step toward the implementation of a portable stroke monitoring system for clinical use. The complete integration of the designed antenna into the helmet system being developed by the Wavison Research Group is one of the potential future developments. An analysis of the array's overall performance and the measurement of cross-coupling between neighboring radiating elements are necessary for this design.

Bibliography

[1] Amanda G. Thrift et al. «Global stroke statistics». In: *International Journal of Stroke* 12.1 (2017), pp. 13–32. DOI: 10.1177/1747493016676285. URL: https://doi.org/10.1177/1747493016676285.

[2] Michael Brainin et al. «Acute neurological stroke care in Europe: results of the European Stroke Care Inventory». In: *European Journal of Neurology* (2000). DOI: 10.1046/j.1468-1331.2000.007001005.x. URL: https://doi.org/10.1046/j.1468-1331.2000.007001005.x.

[3] Mauro Furlan et al. «Spontaneous neurological recovery after stroke and the fate of the ischemic penumbra». In: *Annals of Neurology* (1996). DOI: 10.1002/ana.410400213. URL: https://doi.org/10.1002/ana.410400213.

[4] François Chollet et al. «The functional anatomy of motor recovery after stroke in humans: a study with positron emission tomography». In: *Annals of Neurology* (1991). DOI: 10.1002/ana.410290112. URL: https://doi.org/10.1002/ana.410290112.

[5] W. Nowinski. «Taxonomy of Acute Stroke: Imaging, Processing, and Treatment». In: *Diagnostics* (2024).

[6] Gillian Mead et al. «A systematic review and synthesis of global stroke guidelines on behalf of the World Stroke Organization». In: (2023). DOI: 10.1177/17474930231156753. URL: https://doi.org/10.1177/17474930231156753.

[7] Zhao Wang et al. «Medical Applications of Microwave Imaging». In: *The Scientific World Journal* 2014.1 (2014), p. 147016. DOI: https://doi.org/10.1155/2014/147016. eprint: https://onlinelibrary.wiley.com/doi/pdf/10.1155/2014/147016. URL: https://onlinelibrary.wiley.com/doi/abs/10.1155/2014/147016.

[8] C. Origlia et al. «Review of Microwave Near-Field Sensing and Imaging Devices in Medical Applications». In: *Italian National Conference on Sensors* (2024). DOI: 10.3390/s24144515. URL: https://doi.org/10.3390/s24144515.

[9] Valeria Mariano et al. «Field-Based Discretization of the 3-D Contrast Source Inversion Method Applied to Brain Stroke Microwave Imaging». In: *IEEE Journal of Electromagnetics RF and Microwaves in Medicine and Biology* (2024).

[10] David Rodriguez-Duarte et al. «Experimental Assessment of Real-time Brain Stroke Monitoring Via a Microwave Imaging Scanner». In: *IEEE Open Journal of Antennas and Propagation* (2022). DOI: 10.1109/ojap.2022.3192884. URL: https://doi.org/10.1109/ojap.2022.3192884.

[11] Vishnupriya Leena and Nikhil Kumar. «Quasi Crystal based Circular Patch Antenna with Artificial Magnetic Conductor for Breast Cancer Detection». In: (2025).

[12] D. Awan et al. «UWB Antenna with Enhanced Directivity for Applications in Microwave Medical Imaging». In: *Italian National Conference on Sensors* (2024). DOI: 10.3390/s24041315.

[13] Musa N. Hamza, Sławomir Kozieł, and A. Pietrenko-Dabrowska. «Design and experimental validation of a metamaterial-based sensor for microwave imaging in breast, lung, and brain cancer detection». In: *Scientific Reports* (2024). DOI: 10.1038/s41598-024-67103-9.

[14] S. Mousavi et al. «Dual-Sense Circularly Polarized Substrate Integrated Waveguide Antenna for Deep Torso Imaging». In: *IEEE Transactions on Antennas and Propagation* (2025). DOI: 10.1109/tap.2024.3509212.

[15] Hui Chen and Kwai Man Luk. «Detection Capability Enhanced Biosensor Antenna for Portable Electromagnetic Stroke Diagnostic Systems». In: (2023). DOI: 10.1109/tbcas.2023.3313732.

[16] Hui Chen and Kwai-Man Luk. «An Antenna Array Based on Radar Operation with High Detection Capability and Implementability for Three-Dimensional Head Imaging». In: (2024). DOI: 10.1109/tap.2024.3388214.

[17] Shubhadip Paul, Nilesh Kumar Tiwari, and M. Jaleel Akhtar. «Design of Highly Directive GRIN MS Lens Integrated DFHA for Deep Tissue Biomedical Imaging». In: (2023). DOI: 10.1109/tap.2022.3222808.

[18] Xiang Gao et al. «Design of Low-Profile Ultrawideband Conformal Array Antennas for Microwave Brain Imagers». In: (2023). DOI: 10.1109/apcap59480.2023.10469948.

[19] Hui Chen et al. «An On-Body Matched Differentially Fed Magnetoelectric Dipole Antenna for Head Imaging Systems». In: *IEEE Transactions on Antennas and Propagation* (2022). DOI: 10.1109/tap.2022.3184512.

[20] N. A. Koma'rudin et al. «Directional Wideband Wearable Antenna with Circular Parasitic Element for Microwave Imaging Applications». In: *Computers, Materials & Continua* (2022). DOI: 10.32604/cmc.2022.024782.

[21] Kamel Sultan and Amin M Abbosh. «Wearable Dual Polarized Electromagnetic Knee Imaging System.» In: *IEEE Transactions on Biomedical Circuits and Systems* (2022). DOI: 10.1109/tbcas.2022.3164871.

[22] Abdulrahman S. M. Alqadami et al. «Compact Unidirectional Conformal Antenna Based on Flexible High-Permittivity Custom-Made Substrate for Wearable Wideband Electromagnetic Head Imaging System». In: *IEEE Transactions on Antennas and Propagation* (2020). DOI: 10.1109/tap.2019.2938849.

[23] Abdulrahman S. M. Alqadami et al. «Compact Flexible Wideband Antenna for On-Body Electromagnetic Medical Diagnostic Systems». In: *IEEE Transactions on Antennas and Propagation* (2020). DOI: 10.1109/tap.2020.2996815.

[24] Abdulrahman S. M. Alqadami et al. «Flexible Electromagnetic Cap for Head Imaging». In: *IEEE Transactions on Biomedical Circuits and Systems* (2020). DOI: 10.1109/tbcas.2020.3025341.

[25] Md. Rokunuzzaman et al. «Compact 3-D Antenna for Medical Diagnosis of the Human Head». In: *IEEE Transactions on Antennas and Propagation* (2019). DOI: 10.1109/tap.2019.2908066.

[26] Saba Rashid et al. «3-D Printed UWB Microwave Bodyscope for Biomedical Measurements». In: *IEEE Antennas and Wireless Propagation Letters* (2019). DOI: 10.1109/lawp.2019.2899591.

[27] Abdulrahman S. M. Alqadami et al. «Wearable Electromagnetic Head Imaging System Using Flexible Wideband Antenna Array Based on Polymer Technology for Brain Stroke Diagnosis». In: *IEEE Transactions on Biomedical Circuits and Systems* (2019). DOI: 10.1109/tbcas.2018.2878057.

[28] Zuria Mahmud et al. «Microwave Imaging for Breast Tumor Detection Using Uniplanar AMC Based CPW-Fed Microstrip Antenna». In: *IEEE Access* (2018). DOI: 10.1109/access.2018.2859434.

[29] Ali Recai Çelik et al. «Development of an ultra-wideband, stable and high-directive monopole disc antenna for radar-based microwave imaging of breast cancer». In: *Journal of Microwave Power and Electromagnetic Energy* (2018). DOI: 10.1080/08327823.2018.1458692.

[30] Xuyang Li et al. «A Compact Double-Layer On-Body Matched Bowtie Antenna for Medical Diagnosis». In: *IEEE Transactions on Antennas and Propagation* (2014). DOI: 10.1109/tap.2013.2297158.

[31] Francesco Clemente et al. «Ultra-wideband miniaturised high permittivity-matched antennas for biomedical diagnostic». In: *European Conference on Antennas and Propagation* (2013).

[32] Reza K. Amineh et al. «Near-Field Microwave Imaging Based on Aperture Raster Scanning With TEM Horn Antennas». In: *IEEE Transactions on Antennas and Propagation* (2011). DOI: 10.1109/tap.2010.2103009.

[33] A. Eesuola et al. «Novel ultra-wideband directional antennas for microwave breast cancer detection». In: *2011 IEEE International Symposium on Antennas and Propagation (APSURSI)* (2011). DOI: 10.1109/aps.2011.5996646.

[34] Young K. Kwag et al. «A high-directive bowtie radar antenna with a pyramidal reflector for ultra wideband radar imaging applications». In: *Microwave and Optical Technology Letters* (2009). DOI: 10.1002/mop.24043.

[35] Kwai-Man Luk et al. «A New Wideband Unidirectional Antenna Element». In: (2006).

[36] Ondřej Fišer et al. «UWB Bowtie Antenna for Medical Microwave Imaging Applications». In: *IEEE Transactions on Antennas and Propagation* (2022). DOI: 10.1109/tap.2022.3161355.

[37] Nooshin Valizade Shahmirzadi et al. «Electronically Scanned Active Sensor Array for the Imaging of Compressed Breast». In: *European Conference on Antennas and Propagation* (2023). DOI: 10.23919/eucap57121.2023.10133793.

[38] Mohammad Shahidul Islam et al. «A Portable Electromagnetic Head Imaging System Using Metamaterial Loaded Compact Directional 3D Antenna». In: *IEEE Access* (2021). DOI: 10.1109/access.2021.3069712.

[39] Mahdi Ghorbani et al. «Double ridged horn antenna designs for wideband applications». In: *Iranian Conference on Electrical Engineering* (2011).

[40] IT'IS Foundation. *Dielectric Properties Database*. https://itis.swiss/virtual-population/tissue-properties/database/dielectric-properties. 2025.

[41] A. Cuccaro et al. «Subcranial Encephalic Temnograph-Shaped Helmet for Brain Stroke Monitoring». In: *Italian National Conference on Sensors* (2024).

[42] D. O. Rodriguez-Duarte et al. «Brick-Shaped Antenna Module for Microwave Brain Imaging Systems». In: *IEEE Antennas and Wireless Propagation Letters* (2020). DOI: 10.1109/lawp.2020.3022161.

[43] Natalia Nikolova. *Lecture 18: Horn Antennas*. https://www.ece.mcmaster.ca/faculty/nikolova/antenna_dload/current_lectures/L18_Horns.pdf. Lecture notes, McMaster University. 2022.

[44] C. Bruns, P. Leuchtmann, and R. Vahldieck. «Comprehensive analysis and simulation of a 1-18 GHz broadband parabolic reflector horn antenna system». In: *IEEE Transactions on Antennas and Propagation* 51.6 (2003), pp. 1418–1422. DOI: 10.1109/TAP.2003.812236.

[45] Ramin Dehdasht-Heydari, H.R. Hassani, and Alireza Mallahzadeh. «Quad ridged horn antenna for UWB applications». In: *Progress in Electromagnetics Research-pier - PROG ELECTROMAGN RES* 79 (Jan. 2008), pp. 23–38. DOI: 10.2528/PIER07091602.

[46] Seyed Moein Pishnamaz et al. «Reducing Waves on the Body Surface in Near-Field Medical Diagnostics by a Dielectric Rod Antenna». In: *IEEE Transactions on Antennas and Propagation* 71.10 (2023), pp. 7958–7969. DOI: 10.1109/TAP.2023.3305097.

[47] Marta Cavagnaro and Giuseppe Ruvio. «Numerical Sensitivity Analysis for Dielectric Characterization of Biological Samples by Open-Ended Probe Technique». In: *Sensors* 20.13 (2020). ISSN: 1424-8220. DOI: 10.3390/s20133756. URL: https://www.mdpi.com/1424-8220/20/13/3756.